Faculteit Wetenschappen
Vakgroep Vaste-Stofwetenschappen

A fundamental study of advanced metal/semiconductor contacts

door

Wouter Leroy

Promotor: prof. dr. ir. R.L. Van Meirhaeghe
Co-promotor: prof. dr. C. Detavernier

Proefschrift ingediend tot het behalen van de graad van
Doctor in de Wetenschappen

Academiejaar 2006–2007

Ph. D. Jury:

R.L. Van Meirhaeghe (UGent) (promotor)

C. Detavernier (UGent) (co-promotor)

J. Jordan-Sweet (IBM)

P. Van Daele (UGent)

R. Ryckebusch (UGent) (chairman)

P. Clauws (UGent)

P. Vereecken (IMEC)

All science is either physics,
or stamp collecting.

ERNEST RUTHERFORD
(1871-1937)

Dankwoord

Een doctoraat is hoofdzakelijk een zelfstandig zwoegwerkje, edoch is de raad, hulp en steun van vele mensen onontbeerlijk. Volgende mensen verdienen dan ook een plaatsje in dit werk, en hopelijk kunnen ze dit proefschrift ervaren als een bedanking en erkenning voor de voorbije jaren. Bedankt aan:

Prof. Roland Van Meirhaeghe om me de kans te geven aan dit doctoraatswerk te beginnen, voor de wetenschappelijke begeleiding met zijn verrijkende en verreikende Schottky-ervaringen, en natuurlijk ook voor de gezellige omgang o.a. bij de koffie.

Prof. Christophe Detavernier voor de uitstekende wetenschappelijke begeleiding en dito stimuli op de juiste momenten, voor zijn contacten met IBM, en voor de aangename bureau-gesprekken.

The IBM-people, beginning with Christian Lavoie for the opportunity to perform *in situ* XRD measurements at Brookhaven National Laboratory, and for the critical, but fun conversations regarding the publications and beer. Also, Jean Jordan-Sweet for technical assistance at the synchrotron, and for enthusiastically accepting the invitation to be on my Ph.D. commission.

Verder ook meerdere mensen uit de vakgroep. Davy Deduytsche voor de vele hulp met en tijdens metingen, de hulp in het doden van de zenuwen, stress en tijd, maar zeker ook voor het helpen verorberen van de veel te grote mega-amerikaanse pizza na een week nachtwerk. Lucien Van Meirhaeghe voor de onschatbare technische hulp, niet op zijn minst bij het C-AFM werk. Verder ook Stijn Mahieu voor de steun vanop een verdiepje hoger, waar ik ook Jo'tje moet bedanken voor het 3-inch geknutsel; Olivier Janssen, Gilbert Notebaert en Ulric Demeter voor de technische hulp; en tenslotte Karl, Stefaan, de 'jonkies'(Charlotte, Koen en Werner) en de chinezen voor de leuke samenwerking.

Hoewel een doctoraat 'beetje een leven op zichzelf is', heb ik heel veel steun gekregen van familie en vrienden. Ik wil op de eerste plaats mijn ouders bedanken voor alle kansen, steun en hulp. Zeker ook mijn drie lieve zusjes die altijd (uit eigen wil!) informeerden naar mijn werk, en de schattige kindjes (ook hij/zij die zich nog niet heeft laten zien) om de wereld af en toe terug op haar juiste waarde te laten schatten. Verder nog een hele hoop vrienden, die elk op hun manier (al dansend, drinkend, etend, zingend, babbelend,...) me gesteund hebben doorheen de laatste vier jaren. Ik wil als laatste ook Barbara bedanken, voor haar immer enthousiaste aanwezigheid en lieve woorden.

Nederlandstalige Samenvatting

MINIATURISATIE is voor de micro-elektronica reeds vele jaren het middel bij uitstek om aan **Moore's Law** te voldoen. Deze zegt (in een verkorte versie): "*Het aantal transistoren op een computerchip verdubbelt elke 18 maanden*", en is voor de fabrikanten eerder een drijvende kracht geworden dan een observatie. Verdere miniaturisatie brengt echter meerdere problemen aan het licht, zoals o.a. de invloed van stress op de silicide-vorming, de lekstroom van de dunner wordende SiO_2-poort ('*gate*'), en de toename van elektrisch verbruik en van de warmte-productie.

We geven een paar mogelijke paden die geopperd worden om de huidige tred in ontwikkeling van micro-elektronica aan te houden. Het vervangen van de huidige polykristallijne Si gate door een metaal gate (of een volledige silicide-gate), zou een deel van de problemen kunnen oplossen. Ook het gebruik van Schottky juncties in plaats van de huidige p-n juncties, wordt weer ter sprake gebracht. Een heel ander pad ligt in het gebruiken van andere materialen dan Si. Mogelijke kandidaten hiervoor zijn: de Si-verwante materialen ($SiGe$, Ge, SiC, $Si_{1-x-y}Ge_xC_y$), C-houdende materialen zoals diamant en koolstof nanobuizen, en III-V halfgeleiders ($GaAs$, GaN, InP). Op veel vlakken hebben de vernoemde materialen betere kwaliteiten dan het huidig gebruikte Si, edoch bevinden toepassingen ervan zich ofwel in een experimentele fase, ofwel hebben ze slechts een niche van de markt kunnen veroveren (vb. $GaAs$ in de mobiele technologie). Ge en $GaAs$ worden naar voor gebracht als materialen met hoge mobiliteit, voor het gebruik als geleidend kanaal ('channel') in de transistor. Andere materialen als diamant en SiC vinden eerder toepassing in de niche-markt van hoog-vermogentoepassingen.

Het eerste deel van dit werk situeert zich binnen deze ontwikkelingen als fundamenteel onderzoek naar de inhomogene aard van Schottky barrières. Het tweede deel spitst zich toe op de vorming van carbides, die veelbelovende kandidaten zijn om koolstofhoudende halfgeleiders te contacteren. Het laatste deel illustreert de toepasbaarheid van de carbide contacten op koolstof nanobuizen en diamant.

Elektrische karakterisering van Au/n-GaAs Schottky contacten met behulp van een geleidende-tip AFM

METAAL/HALFGELEIDER contacten maken deel uit van zowat alle elektronische toepassingen. De belangrijkste eigenschap van een metaal/halfgeleider contact is de Schottky barrièrehoogte (SBH). Eerst wordt bondig de theoretische achtergrond geschetst, met de klemtoon op de recente theorieën rond inhomogeniteiten (Pinch Off Theorie (PO) en Bond Polarization Theorie (BPT)).

Vervolgens wordt de atomaire krachtmicroscoop met geleidende tip (C-AFM) besproken, als veelbelovende, nieuwe techniek voor het bestuderen van (sub)micron structuren. AFM wordt sinds eind jaren '80 courant gebruikt voor het topografisch bestuderen van oppervlakken. Midden de jaren '90, werd de AFM uitgerust met een geleidende tip, om deze nanometer-nauwkeurige topografische techniek te combineren met gekende, macroscopische elektrische karakteriseringstechnieken. We hebben een bestaande AFM omgebouwd tot C-AFM om I/V-karakteristieken te meten op kleine $Au/n-GaAs$ Schottky contacten. Er werd geen verschil gevonden tussen de verschillende materialen van de tips die werden gebruikt, $25nm\,Pt$-coating of $20nm\,Cr/20nm\,Au$-coating, noch tussen de verschillende veerconstantes van de cantilevers. De Pt-gecoate tips met kleine krachtsconstante, worden geprefereerd omwille van de langere levensduur en het stabieler blijven van het elektrische contact, respectievelijk.

Via elektronenbundel lithografie werden kleine $Au/n-GaAs$ contacten vervaardigd op micron- en submicron schaal. Er kon echter geen stabiel elektrisch contact gehouden worden tussen de C-AFM en de **submicron** contacten. De reden hiervoor is wellicht een te grote thermische drift van de piezo-elementen, welke de positionering van het sample verzorgen. Wel werden er 368 vierkante $Au/n-GaAs$ Schottky contacten elektrisch gekarakteriseerd met behulp van de C-AFM, waarvan de groottes varieerden tussen $6\mu m \times 6\mu m$ en $150\mu m \times 150\mu m$. Alle diodes ondergingen een gelijkaardig productieproces tot vlak voor de Au-depositie. Groep B (260 diodes) onderging een bijkomende chemische dip in een $HCl : H_2O$ (1:1) oplossing, met reiniging in H_2O. Via het thermionische emissie-model werd voor elke diode de *effectieve barrièrehoogte* en de *idealiteitsfactor* berekend, uit de opgemeten I/V-karakteristiek. De diodes vertonen een niet-ideaal gedrag, en daarom werden de I/V-karakteristieken gefit a.d.h.v. het PO-model. Uiteindelijk werd per groep een gemiddelde *homogene barrièrehoogte* bekomen (zie pagina 29). Via een andere methode, nl. uit de lineaire relatie tussen de effectieve barrièrehoogte en de idealiteitsfactor, werd per groep een *laterale homogene barrièrehoogte* bepaald (zie pagina 32). We concluderen dat **beide gevolgde methodes betrouwbaar zijn voor het bepalen van de homogene barrièrehoogte**. De homogenene barrièrehoogte voor de Au/n-GaAs Schottky contacten van groep A is $1.021\ eV$, en voor de groep B diodes is deze $0.848\ eV$.

De homogene barrièrehoogte van de groep A -diodes hoger dan deze voor de groep B -diodes. Uit voorgaand onderzoek in onze groep, wordt besloten dat dit tengevolge is van aanwezige $Au^{\delta+} - O^{\delta-}$ dipolen in het metaal-halfgeleider grensvlak van de group A -diodes. De experimentele bevestiging van dit **dipool-model** is een belangrijke stap in de **aanvaarding van de (recente) Bond Polarization Theorie**.

Carbides gevormd door vaste-stofreacties tussen dunne lagen

CARBIDES zijn metaal-koolstof verbindingen, voornamelijk gekend omwille van hun heel hoge smelttemperatuur en hoge hardheid (ook bij hoge temperaturen). Door deze eigenschappen worden ze vaak gebruikt als anti-slijtage coatings en in snij-en boortoepassingen. Carbides zijn echter ook metallische geleiders, wat hen aantrekkelijk maakt voor toepassingen in de micro-elektronica, zeker met de huidige interesse in geavanceerde materialen die koolstof bevatten (diamant, koolstof nano-buizen, SiC).

We hebben de vaste-stofreactie tussen transitie-metalen en koolstof bekeken met *in situ* **X-stralen diffractie (XRD)**. Vaste-stofreacties worden in de productie van Si-transistoren gebruikt voor de vorming van de silicide contacten op source, drain en gate (SALICIDE proces). De vaste-stofreacties van carbides kunnen een gelijkaardige rol spelen bij het ontwikkelen van een elektronica op basis van koolstof-houdende halfgeleiders.

Dunne metaallagen ($30nm$) werden bestudeerd op een koolstof-basislaag ($200nm$ C op SiO_2) met behulp van *in situ* XRD, aangevuld met *ex situ* XRD metingen en via X-stralen foto-elektronen spectroscopie (XPS) en rutherford backscattering spectroscopie (RBS).

De verschillende fases van de vaste-stofreactie werden geïdentificeerd voor een opwarming tot max. $1150°C$. W, Mo, Fe, Cr en V vormen carbides, maar Nb, Ti, Ta en Hf hebben een extra capping-laag bovenop de metaallaag nodig om oxidatie te voorkomen. Er werd geopteerd voor een koolstof capping-laag, om eventuele andere dan carbide-reacties uit te sluiten. Mn en Zr vormen, ondanks de voorzorgsmaatregelen (capping-laag, geen vacuüm-onderbreking bij depositie van de verschillende lagen), oxides in plaats van carbides. De resultaten van de fasevorming worden weergegeven in tabel 7.19 op pagina 108, en de vormingstemperaturen (bij een opwarmtempo van $3°C/s$) staan samengevat op pagina 109 in tabel 7.20.

Verder werd ook de kinetiek van de vaste-stofreactie bestudeerd d.m.v. *in situ* XRD metingen met verschillende opwarmtempo's. Via een zogenaamde **Kissinger-analyse**, werd voor de carbide-vormingen een activatie-energie bepaald (zie tabel 8.1, pagina 124). Deze helpen bij het begrijpen van de onderliggende mechanismen bij de fase-vorming van carbides.

Carbides als contacten voor geavanceerde C-houdende halfgeleiders

KOOLSTOF-houdende halfgeleiders zijn veelbelovende materialen voor de toekomst van de micro-elektronica. Carbides kunnen worden beschouwd als goede kandidaten om deze materialen elektrisch te contacteren. Koolstof nanobuizen (CNTs) en diamant zijn twee geavanceerde halfgeleiders, elk met heel bijzondere eigenschappen.

CNTs zijn heel sterk en toch enorm flexibel, ze hebben speciale chemische eigenschappen zoals bijvoorbeeld de mogelijkheid om CNTs te vullen met andere stoffen, en bovenal kunnen ze zowel metallisch als halfgeleidend zijn, afhankelijk van hun atomaire structuur. Er is reeds uitgebreid geëxperimenteerd met het gebruik van CNTs, en de eerste CNT-transistoren zijn ondertussen reeds een feit (zij het wel enkel in laboratorium-omstandigheden). Een transistor heeft nood aan elektrische connecties, en daar kunnen carbides voor gebruikt worden. Op pagina 138 geven we een mooi voorbeeld van de mogelijkheid om carbides te vormen met CNTs, via een vaste-stofreactie.

Diamant wint de laatste jaren aan belang binnen de halfgeleider-industrie, ten gevolge van de vooruitgang van de productie van synthetische diamant. 'Chemical Vapour Deposition' (CVD) diamant heeft het grote voordeel t.o.v. natuurlijke diamant en 'high pressure high temperature' synthetische diamant, dat het op elk substraat en over grote oppervlakten kan worden afgezet, en dat de eigenschappen van de diamant gemanipuleerd kunnen worden. Diamant zal in de eerste plaats gebruikt worden in elektronica die blootgesteld wordt aan extreme omgevingen (hoge temperaturen, corrosieve omgeving,...), maar kan haar weg naar algemene bekendheid via niche-markten waar maken.

Het contacteren van diamant blijft ook nog steeds veel vragen oproepen, en om de excellente elektrische en thermische eigenschappen van het diamant (zie tabel 9.1, pagina 141) te benutten, moeten ook de contacten voldoen aan een reeks van eigenschappen. Ze moeten sterk adherent aan het diamant zijn, stabiel bij hoge temperaturen, resistent aan chemische corrosie, een goede elektrische geleiding vertonen, en compatibel zijn met het farbicage-proces. Carbides bezitten veel van deze eigenschappen en zijn daardoor de geschikte kandidaat om diamant te contacteren.

We tonen aan dat carbide contacten gevormd kunnen worden op diamant m.b.v. een vaste-stofreactie, en dat dezelfde fases optreden als geïdentificeerd in het vorige deel van dit werk op amorf-koolstof. Verder werd ook een eerste onderzoek verricht naar het elektrische gedrag van deze contacten. Hieruit kunnen we concluderen dat de kristalstructuur van het metaal-diamant grensvlak de elektrische eigenschappen sterk beïnvloedt. De verklaring via de Bond Polarization Theorie is hierbij relevant, en een beter begrip van het diamant-oppervlak en de invloed van factoren als depositietechniek en reiniging, zijn noodzakelijk.

Table of Contents

Dankwoord i

Nederlandstalige Samenvatting iii

Table of Contents ix

Preface xiii

Scope of this work xviii

I ELECTRICAL CHARACTERISATION OF AU/N-GAAS SCHOTTKY CONTACTS USING C-AFM 1

1 Introduction 3
- 1.1 Theoretical models describing the Schottky Barrier 3
- 1.2 Electrical behaviour of the Schottky Barrier 6
- 1.3 The inhomogeneous Schottky barrier 8

2 Conducting probe Atomic Force Microscopy (C-AFM) 13
- 2.1 Atomic Force Microscopy 13
- 2.2 The conducting probe AFM 15
- 2.3 Our C-AFM system 16

3 Experimental Details 23

4 The SBH inhomogeneities in identically prepared Au/n-GaAs Schottky contacts 25
- 4.1 The submicron Schottky contacts 26
- 4.2 The micron Schottky contacts 28

II THIN FILM SOLID-STATE REACTIONS FORMING CARBIDES 37

5 General properties of carbides 39
5.1 Introduction 39
5.2 General properties of carbide materials 42

6 Experimental Details 49

7 Thin film solid-state reactions forming carbides 55
7.1 The Titanium - Carbon system 55
7.2 The Vanadium - Carbon system 64
7.3 The Chromium - Carbon system 70
7.4 The Manganese - Carbon system 75
7.5 The Iron - Carbon system 77
7.6 The Zirconium - Carbon system 82
7.7 The Niobium - Carbon system 86
7.8 The Molybdenum - Carbon system 90
7.9 The Hafnium - Carbon system 94
7.10 The Tantalum - Carbon system 99
7.11 The Tungsten - Carbon system 104
7.12 Summary 108

8 Kinetics for the solid-state formation of carbides 113
8.1 The growth models 113
8.2 Kissinger analysis 115
8.3 Determining the activation energies for the W-C system 116
8.4 The activation energies for the other M-C systems 119
8.4.1 Ti-C: 119
8.4.2 V-C: 120
8.4.3 Fe-C: 120
8.4.4 Nb-C: 121
8.4.5 Mo-C: 122
8.4.6 Hf-C: 123
8.5 Summary 124

III Carbides as contacts to C-containing advanced semiconductors **131**

9 Carbides as contacts to C-containing advanced semiconductors **133**
9.1 Carbon Nanotubes (CNTs) 134
9.2 CVD-Diamond 140

CONCLUSIONS **155**

APPENDICES **157**

B Visualization of the EBL process **161**

C Error calculation for the activation energies determined by *in situ* XRD **163**

List of Publications **169**

Preface

1947 is marked in the mind of most 'semiconductor'-scientists as the start of the technology-era, with the successful fabrication of the first practical **point-contact transistor** by 1956-nobel prize winners John Bardeen, Walter Brattain and William Shockley at Bell Laboratories. But long before, in 1833, Michael Faraday discovered that the electrical resistivity of silver sulfide has a negative temperature coefficient, which is an intrinsic property of a semiconductor. In the late 1950's, another break-

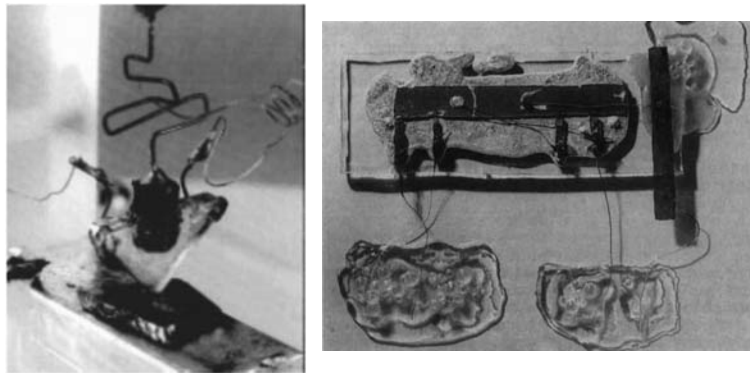

Figure 1: *Picture of the first point-contact transistor, made by Bardeen, Brattain and Schockley (left) and a picture of the first IC made by Kilby (right).*

through occurred with the discovery that semiconductor materials could be combined and treated so that they functioned as an entire circuit or subassembly rather than as a circuit component; 2000-nobel prize winner Jack Kilby invented the integrated circuit (IC) in 1958 at Texas Instruments. The use of personal computers stimulated a boom in the electronic materials industry, during the 1980's and nowadays, semiconductor devices are all around us. They can be found in just about every commercial product we touch, from the family car to the pocket calculator. Semiconductor devices are contained in television sets, portable radios, stereo equipment, and much more.

Although silicon and germanium were used in radar detectors in the early 1940s, silicon is the most common semiconductor material used today. It was the unexpected discovery in 1959 that silicon dioxide can passivate (protect) the surface of silicon, which led to the invention of metal-oxide-silicon (MOS) transistors. This property, along with some others (*e.g.* the band gap of 1.1 eV which permits the operation of silicon semiconductors devices at higher temperatures than germanium), brought about the current dominance of silicon in the electronics industry.

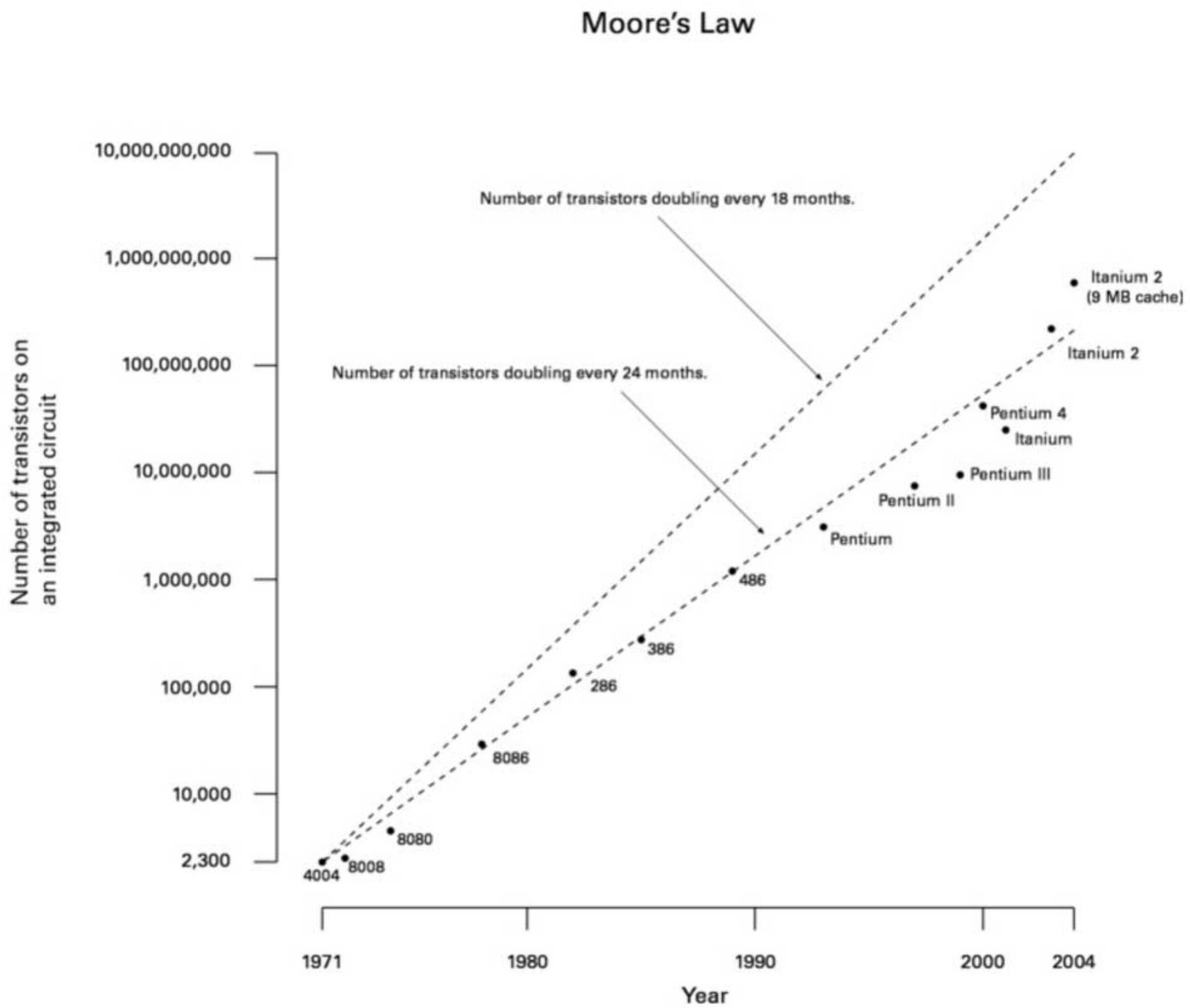

Figure 2: *Moore's Law illustrated with the growth of the transistor counts for Intel processors.*

In 1965, Gordon Moore made an observation and forecast:

> *The complexity for minimum component costs has increased at a rate of roughly a factor of two per year ... Certainly over the short term this rate can be expected to continue, if not to increase. Over the longer term, the rate of increase is a bit more uncertain, although there is no reason to believe it will not remain nearly constant for at least 10 years. That means by 1975, the number of components per integrated circuit for minimum cost will be 65,000. I believe that such a large circuit can be built on a single wafer.*

It is common to cite **Moore's Law** to refer to the rapidly continuing advance in computing power per unit cost, and its most popular formulation is of the doubling of the number of transistors on integrated circuits (a rough measure of computer processing power) every 18 months, see figure 2. Moore's Law nowadays is more than only an observation, it serves as a goal for the industry, driving semiconductor manufacturers to focus enormous energy aiming for the specified increase in processing power. In this regard, it can be viewed as a *self-fulfilling prophecy*.

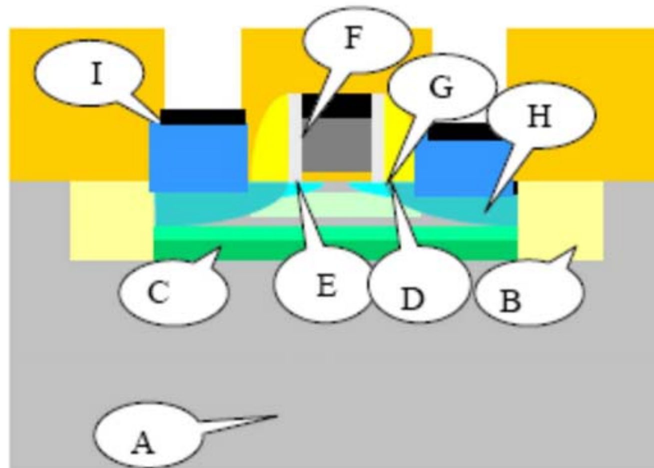

A: Starting Material
B: Isolation
C: Well Doping
D: Channel Surface
E: Channel Doping and Channel Strain
F: Gate Stack
G: Extension Junction and Halo
H: Contacting Source/Drain Junction
I: Elevated Junction and Contacts

Figure 3: *Illustration of a MOSFET, pointing out the major problems concerning the down-scaling, as explained in the International Technology Roadmap for Semiconductors (ITRS).*

Down-scaling of Si-devices:

Down-scaling of the device dimensions is the current trend in manufacturing, to attain the required processing speed. The smaller the distance an electric signal has to travel, the faster the binary information is processed. Diminishing the dimensions of the transistors has made several problems popping up, *e.g.* the stress influence in silicide formation, the electric leakage of the thinning SiO_2 gate dielectric, the increase in power consumption and heat production. Figure 3 shows some of the problems related to the down-scaling of the MOSFET. The full explanation of the problems and thoughts on the solutions can be found in the ITRS Roadmap 2005. We will only be highlighting a few of them. Firstly, the gate-problem (F) is discussed, while for the problems with the starting material (A) and the channel doping and strain (E), the usage of other materials (than Si) might bring a solution.

The gate of the currently-used transistors (MOSFETs) consists of poly-crystalline silicon (poly-Si) layer on a thin insulating layer (SiO_2), above the channel. However, with very thin gate dielectrics, a problem arises that if the poly-Si region immediately above the gate dielectric is not sufficiently doped, it becomes depleted under the influence of a gate potential for normal transistor operation. The depletion region then acts like a parasitic dielectric, being added to the gate dielectric. This results in a thickening of the overall gate dielectric and consequently, it weakens the control of the gate over the channel. Replacing the poly-Si gate by a **metal gate** can lead to elimination of the gate-depletion effect (provided that other challenges related to the use of metal gates are overcome). Furthermore, although the materials now used (SiO_2 and $SiON$) are fabrication-friendly, much better performance in terms of improved transistor speed and reduced current leakage can be obtained by switching to a metal gate and a high-k gate dielectric.

According to Zhang and Ostling [1], the "old" idea [2] of using **Schottky junctions** instead of p-n junctions in the source/drain regions, has revisited the engineering tables. This example illustrates the quest for down-scaling pushes researchers to combine traditional methods with new methods, materials and approaches.

Other materials:

If silicon cannot continue to double processing speed every 18 months, another technology might be able to take over. Scientists and technology enthusiasts have been pointing in numerous directions: the Si-related materials ($SiGe$, Ge, SiC, $Si_{1-x-y}Ge_xC_y$), the C-materials ***diamond*** and ***carbon nanotubes***, the III-V materials ($\mathbf{GaAs}$, GaN, InP) or more futuristic approaches as quantum computing and DNA computing. Some of these approaches are still highly experimental but have known early successes, such as creating elementary transistors and memory cells. Still, bringing engineering procedures used in experiments to a mass-production en-

vironment may pose greater challenges for these technologies than silicon faced in its 30 years of improving performance. Because of their close Si-relation and thus processing, the Si-related materials are the first choice as improvements to the currently used devices (*e.g.* strained-Si or $Si_{1-x}C_x$ in the channel of the MOSFET). However, most methods suffer from not being as general purpose as silicon computing. But in some of these areas, however, the new technologies outpower silicon-based methods by far. Most of them will start out in a niche, like any disruptive technology, before reaching general acceptance in the technology-industry. The III-V materials are a good example for this, as they are currently reaching unseen heights in their use for mobile/wireless technologies ($GaAs$) and for light-emitting diodes (GaN).

Scope of this work:

The first part of this work deals with *the electrical characterisation of Au/n-GaAs Schottky contacts using Conducting probe Atomic Force Microscopy (C-AFM)*.

Chapter 1 gives a brief overview of the theoretical background concerning Schottky barriers.

In Chapter 2, we discuss the relatively new C-AFM technique, which is extremely useful for characterising **small-sized features**. It can combine nanometer-resolved topography measurements with standard electrical characterisation techniques. For example, Bietsch *et al.* [3] used this technique to test nanoscale wire arrays electrically.

As mentioned before, **GaAs** is currently undergoing a revival due to the wireless industry. The Au/n-GaAs Schottky contact has already been extensively studied and can be regarded as one of 'the standards' for Schottky barrier research [4]. Furthermore, in the near future, the use of metal gates or Schottky junctions are not unthinkable, so a better fundamental understanding of the main property, the Schottky Barrier Height (SBH), is necessary. Chapter 4 contains more **experimental evidence for the recently published Bond-Polarization theory** of Tung [5, 6].

In the second part of this work, we present our results on *the thin film solid-state reactions forming carbides*.

In chapters 5 and 6 we give an overview of the properties of carbides and our experimental details for this part of the research, respectively.

Carbon-containing semiconductors (diamond, CNTs, SiC,...) are relatively new materials to be used in the electronics technology. Semiconductor applications need electrical contacts and carbides are considered as potential candidates. In Chapter 7 we therefore studied the solid-state formation of the different carbide phases formed starting from thin metal films in contact with carbon. Solid-state formation is a **technological important technique**, currently used in the SALICIDE process [1] for making silicide contacts to silicon devices. The ***in situ*** study shows which of **the different carbide phases** can be formed using a solid-state reaction (in an industrial-relevant environment). This is as a good step towards their application in carbon-containing devices.

In Chapter 8 research on a more fundamental property of the solid-state formation is presented. *In situ* **x-ray diffraction (XRD)** measurements were used to determine **the activation energy** for the different carbide phases. This data can help in the understanding of the underlying mechanisms of the phase formation.

Finally, in the last part, we focus on the advanced carbon-containing semiconductors: carbon nanotubes (CNTs) and diamond. Chapter 9 illustrates the importance of these two materials by summarizing some of the relevant published work. We also present some experimental results, indicating the possibility of using **carbides as contacts for these carbon-containing semiconductors**.

Bibliography

[1] S. L. Zhang and M. Ostling. *Crit. Rev. Solid State Mat. Sci.*, 28(1):1, 2003.

[2] S.M. Sze. *Physics of Semiconductor Devices.* John Wiley and Sons, Inc., New York, 2nd. edition, 1981.

[3] A. Bietsch, M. A. Schneider, M. E. Welland, and B. Michel. *J. Vac. Sci. Technol. B*, 18(3):1160, 2000.

[4] S. Forment, R. L. Van Meirhaeghe, A. De Vrieze, K. Strubbe, and W. P. Gomes. *Semicond. Sci. Technol.*, 16(12):975, 2001.

[5] R. T. Tung. *Phys. Rev. Lett.*, 84(26):6078, 2000.

[6] R. T. Tung. *Mater. Sci. Eng. R-Rep.*, 35(1-3):1, 2001.

Part I

Electrical characterisation of Au/n-GaAs Schottky contacts using C-AFM

Chapter 1

Introduction

METAL-SEMICONDUCTOR (MS) contacts are an essential part of virtually all semiconductor electronic and optoelectronic devices. One of the most important properties of a MS interface is its Schottky barrier height (SBH). The SBH controls the electronic transport across the MS interface and therefore, it is of vital importance to the successful operation of any semiconductor device. Ever since the second half of the 20th century, many textbooks and articles were published with efforts to unravel the SBH mystery.

In this chapter, a little theoretical background about the SBH formation will be discussed. A more extensive overview can be found in the review article of Tung [1]. Then, the (theoretical) electrical behaviour of the SB will be discussed, focussed on the current-voltage (IV) behaviour. We will conclude this introductory chapter with some explanation about the inhomogeneities in the SB.

1.1 Theoretical models describing the Schottky Barrier

THE FIRST theory on the formation of a SB was proposed by Walter Schottky‡ [2] and Sir Neville Mott¶ [3]. They propose that the SBH $\Phi^0_{B,n}$ between a metal with work function ϕ_m and a semiconductor with an electron affinity χ_s should be

$$\Phi^0_{B,n} = \phi_m - \chi_s, \tag{1.1}$$

where the n denotes the SBH measured on an n-type semiconductor (as we will silently presume from now on). Unfortunately, the strong dependence of the SBH on the metal work function predicted by the Schottky-Mott theory, has received little support from experiments. The insensitivity of the SBH to the metal work function has been attributed to the 'Fermi level (FL) pinning'. A lot of theories, trying to

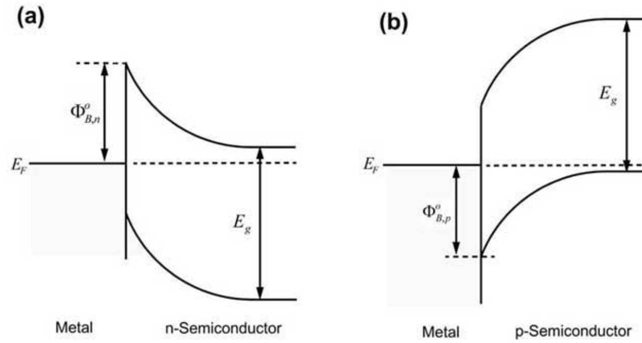

Figure 1.1: *Basic energy band diagram at a metal-semiconductor interface. The SBH is indicated to (a) n-type, (b) p-type semiconductor.*

explain this FL pinning, made assumptions which make the SBH insensitive to the interface structure. But from a standpoint of general physics and chemistry, such assumptions were hard to rationalize. One would expect the SBH to depend on the identity of the semiconductor and the metal, but also on the interface bonding and structure. The latter was shown in the mid 1980s with the dependence of the SBH on the orientation/structure at single crystalline MS interfaces (e.g. [4]). A few years later, it was pointed out that the SBHs at polycrystalline MS interfaces were often inhomogeneous [5–7], which settled some of the disagreements on the FL pinning at those interfaces. New spatially resolved techniques like the Ballistic Electron Emission Microscopy (BEEM) [8], gave direct evidence for this SBH inhomogeneity [9]. The inhomogeneity of the polycrystalline interfaces was consistent with the structure dependent view. But how does one explain the FL pinning phenomenon with this bonding picture?

In 2000, Tung published a new view on things by associating the interface dipole with the chemical bonding at the MS interface: the 'Bond Polarization' theory [10]. In his theory, he uses a method from molecular chemistry, namely the electrochemical potential equalization (ECPE) method, which allows an estimation of all the atomic charges of a large molecule. The total energy of a molecule is the sum of the energies of the individual atoms and the interactions between them:

$$\begin{aligned} E_{tot}(n_1, n_2, \ldots, n_N) &= \sum_i^N (\text{energy of indiv. molec.}) \\ &+ \sum_{i \neq j}^N (\text{interactions between two molec.}), \end{aligned}$$

or

$$E_{tot}(n_1, n_2, \ldots, n_N) = \sum_i^N \left(E_i^0 + U_i n_i + \frac{1}{2} Y_i n_i^2 \right) + \sum_{i \neq j}^N \frac{n_i n_j J_{ij}}{2}, \quad (1.2)$$

where the energy of a single atom was approximated by a second-order Taylor expansion about the neutral atom. J_{ij} is the Coulombic interaction between one electron located at atomic position i and another at the position of the jth atom, thus $J_{ij} = e^2/\epsilon_0 d_{ij}$. The coefficients U_i and Y_i are the Mulliken electronegativity and the hardness of the isolated atom, respectively, and are defined using the electron affinity χ_i and the ionization potential I_i of the atom as $U_i = \chi_i/2 + I_i/2$ and $Y_i = I_i - \chi_i$. The task is then to minimize E_{tot}, subject to the constraint that the net charge of the molecule is zero. The charge transfer can then be estimated from the requirement that, in thermal equilibrium, the electrochemical potential ($\partial E_{tot}/\partial n_i$), is constant throughout the molecule.

To apply this ECPE method in order to estimate the charge transfer and electric dipole at a MS interface, Tung regarded the entire MS region (the 'interface specific region') as a giant molecule. A few planes of atoms each from the semiconductor and metal lattices are included in this molecule. A further assumption is that the charge transfer only occurs between atoms directly involved in the interface bonds. By giving the atoms bulk characteristics, the Mulliken electronegativity and the hardness can be written as: $U_M = \phi_M$, $Y_M = 0$, $U_S = \chi_s + E_g/2$ and $Y_S = E_g$, where ϕ_M is the work function of the metal and E_g is the band gap of the semiconductor. Finally (after some calculations, see [10, 11]), the SBH is:

$$\Phi_B^0 = \gamma_b \left(\phi_M - \chi_s \right) + \left(1 - \gamma_b \right) \frac{E_g}{2}, \quad (1.3)$$

wherein the 'interface parameter' is:

$$\gamma_b = 1 - \frac{e^2 d_{MS} N_b}{\epsilon_{int}(E_g + \kappa)}. \quad (1.4)$$

d_{MS} is the distance between the metal and semiconductor atoms at the interface, N_b the uniform density of chemical bonds, ϵ_{int} the permittivity of the interface region, and κ the sum of all the hopping interactions.

Equation 1.3 predicts the same weak dependence of the SBH on the metal work function, as predicted by other 'gap state models' (e.g. MIGS [12–14]). There are

‡Walter Hermann Schottky lived from 1886 to 1976.

¶Sir Neville Francis Mott lived from 1905 to 1996, and shared the 1977 nobel prize in physics with P. Anderson and J. van Vleck.

however, quite some issues which remain unsettled about the application of the ECPE method at MS interfaces. But most important is **the validity of the overall view on the bonding-related charge transfer at the interface**.

1.2 Electrical behaviour of the Schottky Barrier

TO UNDERSTAND the electrical behaviour of a Schottky Barrier, figure 1.2 shows the influence of an external applied bias on the SB. For a positive or forward bias (i.e. negative bias applied on the n-type semiconductor, compared to the metal), there is a reduction in the barrier, as seen by the electrons coming from the semiconductor side. The barrier on the metal side remains the same, independent of the applied bias, and this barrier is called the SB Φ_B. When an electron is transported across

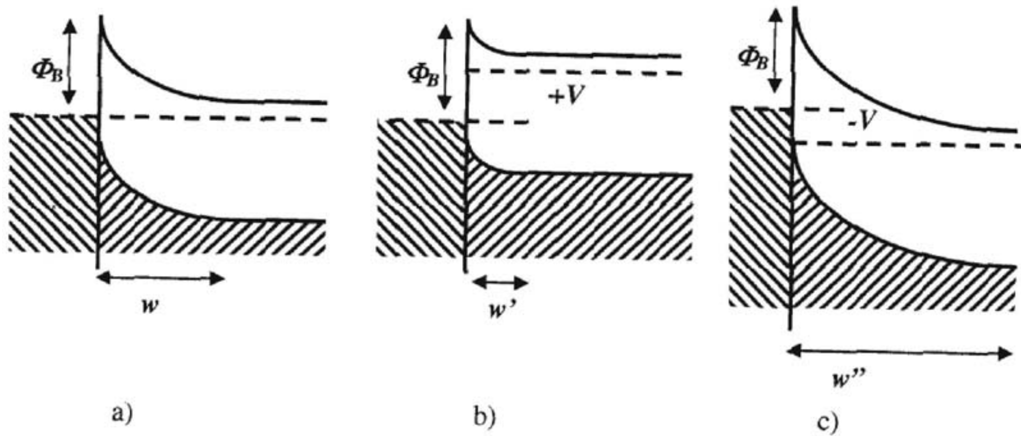

Figure 1.2: *Schottky barrier under with external applied bias, (a) no bias, (b) forward bias, (c) reverse bias.*

a SB, the electric field produced by this particular electron causes a lowering of the barrier. This is called *the image-force effect* and the effect is shown in figure 1.3(a). Special about it, is that this lowering is absent if there is no electron in the conduction band near the top of the barrier. More explanation about this and other effects that influence the electrical behaviour, can be found in e.g. the work of Rhoderick and Williams [15].

Figure 1.3(b) shows the various ways in which electrons can be transported across a MS junction (n-type semiconductor) under forward bias. The inverse processes occur under reverse bias. The mechanisms are:

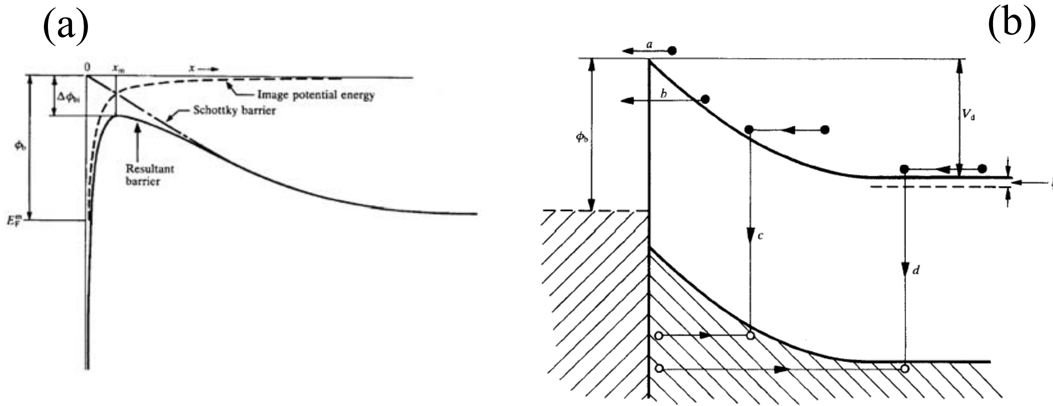

Figure 1.3: *(a) Image-force lowering of the barrier. (b) Transport processes in a forward-biased Schottky barrier.*

(a) emission of electrons from the semiconductor over the top of the barrier into the metal;

(b) quantum-mechanical tunnelling through the barrier;

(c) recombination in the space-charge region;

(d) recombination in the neutral region ('hole injection').

Process (a) is the most important in most of the Schottky diodes and the other processes are regarded as departures of this ideal behaviour. The thermionic emission theory of Bethe [16] describes the current transport as

$$J = \frac{I}{A} = A^{*}T^{2}e^{\left(-\frac{\Phi_B}{k_b T}\right)}\left[e^{\frac{qV}{k_b T}} - 1\right], \tag{1.5}$$

where a Richardson constant is defined as

$$A^{*} = \frac{4\pi m^{*} q k_b^2}{h^3}. \tag{1.6}$$

A is the surface of the diode, k_b is the Boltzmann constant, T the temperature, m^* the semiconductor effective electron mass, q the magnitude of the electronic charge, and h Planck's constant.

To account for the image-force effect on the current-voltage relationship, an ideality factor n is induced in the relationship. It is defined as the inverse of the slope of the I-V curve, normalized by that expected of the perfect thermionic emission process, or:

$$n = \left[1 - \left(\frac{\partial \Phi_B}{q \partial V}\right)\right]^{-1}. \tag{1.7}$$

In real devices, the applied bias across the interface can be diminished by voltage drops across the Ohmic contact and the bulk semiconductor. If the effect of this series resistance is taken into consideration, an Ohmic drop of IR_S should be subtracted from the applied bias to obtain the actual voltage drop across the MS interface. One finally gets as useful relation:

$$J = \frac{I}{A} = A^*T^2 e^{\left(-\frac{\Phi_B}{k_b T}\right)} \left[e^{\frac{q(V-IR_S)}{nk_bT}} - 1 \right]. \quad (1.8)$$

1.3 The inhomogeneous Schottky barrier

A SCHOTTKY BARRIER which has lateral variation in its BH, i.e. along the MS interface, is named '*inhomogeneous*'. This means that along the MS interface, '**patches**' exist, which have their own (higher or lower) SBH. This can be due to the influence of chemical bonds (see the BPT), but also due to the presence of charges, defects, interfacial layers, ... One of the first models that describes the current of an inhomogeneous SB is the 'parallel conduction model' [5], where the total current is the sum of the contributions from every individual area, meaning

$$I(V) = A^*T^2 \left[e^{\left(\frac{qV}{k_bT}\right)} - 1 \right] \sum_i A_i e^{-\frac{\Phi_i}{k_bT}}, \quad (1.9)$$

where A_i and Φ_i are the area and the SBH of the i'th patch, respectively. The main assumption behind the parallel conduction model is the independence of the different segments of an interface, of each other. However, there are some phenomena observed (e.g. greater-than-unity ideality factors, the T_0 anomaly, leakages, the dependence of the SBH on the measurement technique,...) that cannot be explained using this model, unless assumptions are made like e.g. a temperature dependence of the SBH and ideality factor. However, the physical reason for the variation of these parameters is unknown in these analysis. Furthermore, numerical simulations at MS interfaces revealed that the parallel conduction model is in significant error when the SBH varies spatially on a scale less than, or comparable to, the width of the space charge region [17].

The "Pinch Off"(PO) theory [7] gives a coherent explanation of many of these anomalies in the experimental results. The main difference to the previous theories is that the PO theory takes into account the interaction between neighbouring sections of the same interface. For example, when a small patch with a low SBH is surrounded by high SBH patches, the interaction between them will cause the small patch to be 'pinched off'. This means that if an electron would come from outside the space-charge region, it would have to overcome a higher potential barrier than the band-edge position at the MS interface, in order to reach the MS interface. Figure 1.4 shows two illustrations of such a situation. One can see that the potential at the saddle point (marked with an arrow) is higher than the potential at the interface. Using

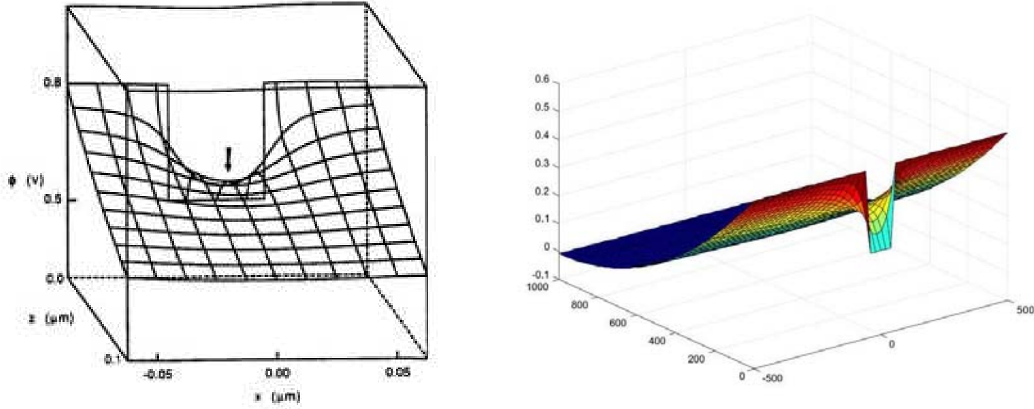

Figure 1.4: *Three-dimensional views of the potential distribution in front of a low SBH patch in a high SBH background. The arrow marks the saddle point.*

this PO theory, Tung explained several experimental phenomena that had no (or only empirical) explanations.

Tung assumes a Gaussian distribution of circular patches* with an area density of patches ρ_p with a constant barrier height:

$$N(\gamma) = \frac{\rho_p}{\sqrt{2\pi\sigma^2}}\, e^{-\frac{\gamma^2}{\sigma^2}}. \tag{1.10}$$

Here, $\gamma = 3(R_p^2 \Delta_p/4)^{1/3}$, with Δ_p the patch parameter. Δ_p is the deviation of the local barrier height from the **homogeneous value** Φ_{B0}, R_p the radius of the circular patch, and σ the standard deviation. The total current through such patchy diodes becomes:

$$\begin{aligned} I_{total} &= AA^{**}T^2 \exp\left(-\frac{\Phi_{B0}}{k_bT}\right)\left[\exp\left(\frac{q\,(V - R_S I_{total})}{k_bT}\right) - 1\right] \\ &\times \left[1 + \frac{8\pi\rho_p\sigma^2\eta^{1/3}}{9\,(V_{b0} - V + R_S I_{total})^{1/3}} \exp\left(\frac{q^2\sigma^2\,(V_{b0} - V + R_S I_{total})^{2/3}}{2k_b^2T^2\eta^{2/3}}\right)\right], \end{aligned} \tag{1.11}$$

with $\eta = \epsilon_s\epsilon_0/qN_D$, ϵ_s and ϵ_0 the permittivity of the semiconductor and the vacuum, respectively, N_D the dopant concentration, R_s the series resistance of the semiconductor bulk and the measurement setup, and V_{b0} the band-bending of the uniform barrier at zero bias.

*In Tung's article, one can find the calculations for the case of strip-patches, and/or for an isolated patch.

Bibliography

[1] R. T. Tung. *Mater. Sci. Eng. R-Rep.*, 35(1-3):1, 2001.

[2] W. Schottky. *Z.Physik*, 113:367, 1939.

[3] N.F. Mott. *Proc. Roy. Soc. (London)*, 171:27, 1939.

[4] R. T. Tung. *Phys. Rev. Lett.*, 52(6):461, 1984.

[5] I. Ohdomari and K. N. Tu. *J. Appl. Phys.*, 51(7):3735, 1980.

[6] Y. P. Song, R. L. Vanmeirhaeghe, W. H. Laflere, and F. Cardon. *Solid-State Electron.*, 29(6):633, 1986.

[7] R. T. Tung. *Phys. Rev. B*, 45(23):13509, 1992.

[8] W. J. Kaiser and L. D. Bell. *Phys. Rev. Lett.*, 60(14):1406, 1988.

[9] H. Sirringhaus, T. Meyer, E. Y. Lee, and H. vonKanel. *Phys. Rev. B*, 53(23):15944, 1996.

[10] R. T. Tung. *Phys. Rev. Lett.*, 84(26):6078, 2000.

[11] R. T. Tung. *Phys. Rev. B*, 6420(20), 2001.

[12] F. Flores and C. Tejedor. 12(4):731, 1979.

[13] J. Tersoff. *Phys. Rev. Lett.*, 52(6):465, 1984.

[14] J. Tersoff. *Phys. Rev. B*, 32(10):6968, 1985.

[15] E.H. Rhoderick and R.H. Williams. *Metal-Semiconductor Contacts*. Clarendon Press, Oxford, second edition, 1988.

[16] H.A. Bethe. *MIT Radiation Lab. Rep.*, 43:12, 1942.

[17] J. L. Freeouf, T. N. Jackson, S. E. Laux, and J. M. Woodall. *Appl. Phys. Lett.*, 40(7):634, 1982.

Chapter 2

Conducting probe Atomic Force Microscope

2.1 Atomic Force Microscopy

BINNIG AND QUATE [1] announced the birth of the Atomic Force Microscope (AFM) as a combination of the principles of the scanning tunnelling microscope (STM) and the stylus profilometer (SP). Like STM, AFM supplies a three dimensional image of a surface, with a high spatial resolution.

An AFM operates by measuring attractive or repulsive forces between a tip and the sample. For this, a small tip at the end of a (very flexible) cantilever (see figure 2.1) is brought near the surface. Due to the forces between the atoms of the tip and the atoms of the surface (repulsive or attractive, depending on the distance between the atoms involved), the cantilever will deform elastically. By measuring this deformation, a topographical image of the surface can be made. The force is defined by Hooke's law $F = k \times \delta z$ with k the force constant of the cantilever and δz the movement/deformation of the cantilever. There are two commonly used scan-modes, namely the contact mode and the non-contact mode (the intermittent mode also exists, but is not discussed). In the first mode, the tip is brought in contact with the surface (which makes the force repulsive). A feedback mechanism moves the sample (or tip) up or down, to compensate the deformation of the cantilever. In the non-contact mode, the distance between tip and sample is typical $10nm - 100nm$, and the force is attractive. The cantilever oscillates at a certain frequency, and when the distance between tip and surface changes, the frequency will alter. Keeping the oscillating frequency constant by moving tip or sample, one gets the topographical information through the feedback mechanism.

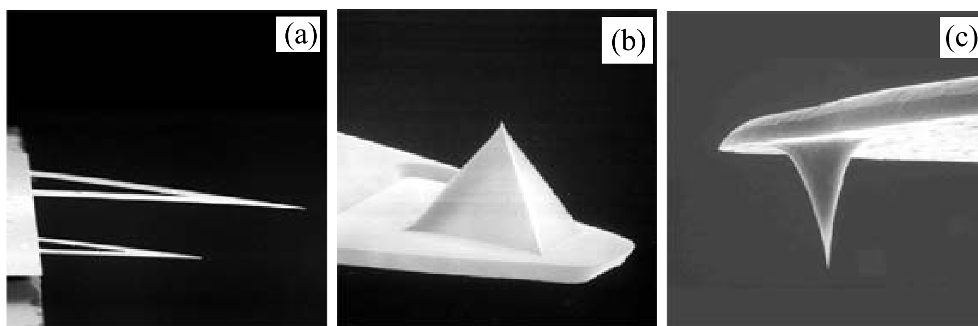

Figure 2.1: *Scanning Electron Microscope (SEM) images of (a) an AFM cantilever, (b) and (c) AFM tips.*

There are lots of options for the detection of the cantilever-deflection: STM(!) [1], capacitance measurements, optical interferometry [2] and laser beam deflection [3]. The latter is the technique used in our system, and will be briefly discussed. For more information on the use of AFM, we refer to [4].

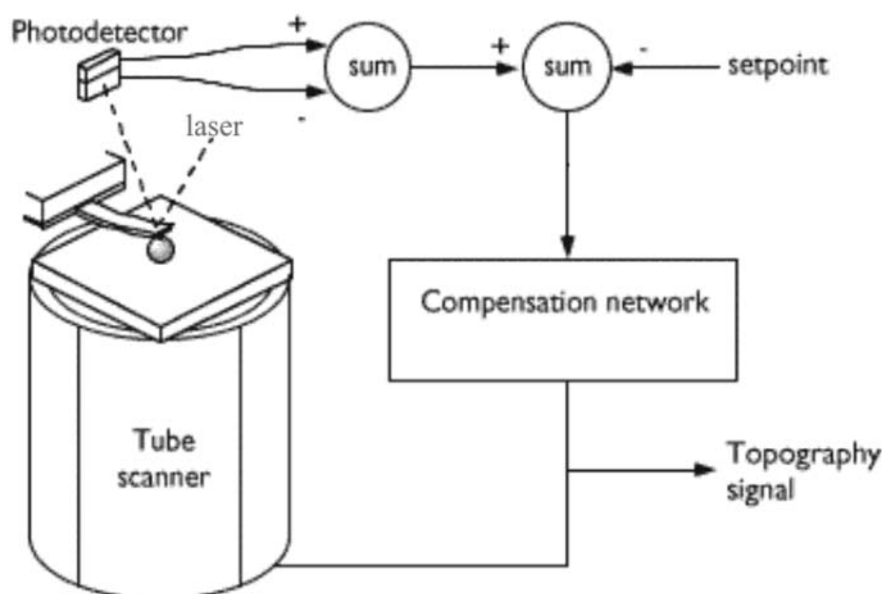

Figure 2.2: *AFM feedback mechanism monitoring the cantilever deflection of a laser beam and adjusting the height of the sample.*

During the operation of the AFM, a laser beam is reflected on the back of the cantilever and detected by a position sensitive photodetector (PSD) (see figure 2.2). If the height of the cantilever would change, the reflected laser beam will move on the PSD. The feedback mechanism now controls the Z-piezo-element to move the sample

up or down, until the reflected beam is back at its original position. Controlling and registering the z-position of the sample, while it is scanned in x- and y-direction, will give a topographic image of the scanned surface.

2.2 The conducting probe AFM

EVER since Binnig and Quate published their invention of the AFM, its usage in research has increased year after year. In microelectronics, the technique has certainly proved its worth, as it enables to envisualize submicron- and nano-sized structures. Due to the miniaturization in microelectronics, it also became harder to test the structures electrically. Therefore, mid the 1990s [5], the AFM was equipped with a conducting probe and researchers tried to combine the excellent topographical properties of the AFM, with (known) electrical characterization techniques.

The C-AFM technique has been used for a wide variety of applications: to measure the resistances of individual molecules and nanoparticles [6], to examine dopant profiles [7], to measure oxide thicknesses in semiconductor devices [8], to image contact resistances across the surfaces of metals [9], and to measure current-voltage dependencies on individual organic semiconductor grains [10]. The work of Freitag *et al.* [11] is relevant in the scope of our work. They used a C-AFM to measure local electronic properties of single-wall nanotube circuits, and thus proved the applicability of this technique in the field of the miniaturization of microelectronics. It is however, the work of Hasegawa *et al.* [12–15] which has the biggest link to previous SB research. They formed nanometer-sized MS interfaces on GaAs and InP by an *in situ* electrochemical process, and used C-AFM to measure the I-V characteristics. The characteristics of the nano-sized contacts showed non-linear $logI - V$ curves with large, voltage-dependent ideality factors, which is one of the typical phenomena for inhomogeneous SBHs.

When using the C-AFM for electrical characterization, the contact between the AFM-tip and the sample is crucial. Bietsch *et al.* [16] give an overview of the basic mechanical requirements for the C-AFM tips:

- mechanically robust: the tip must survive the forces applied when scanning and the additional forces applied to form an electrical contact;
- chemically inert: no passivation by oxidation or electrochemically induced reactions should occur that could interfere with the conductivity of the tip;
- sharp: for a good resolution of the scan images.

Off course, the electrical characteristics of the tip are very important. Schneegans *et al.* [17] characterized the nano-contact between an n-doped silicon tip and a copper sample. They found that this tip-sample system can be considered as an ideal

Schottky diode with a certain resistance in series. However, to characterize the SB at the MS interface, and not at the tip-sample interface, metal-coated or (very) highly doped semiconductor tips are preferred. Bietsch *et al.* [16] suggest platinum-coated tips as having the suitable mechanical stability and a low-ohmic behaviour on various metals. Trenkler *et al.* [18] address the issue that metal-coated tips are frequently affected by wear, and therefore propose the tips with a conductive (i.e. highly-doped) diamond coating as extremely useful. A downside on this last kind of tips is the possible tip-to-tip variation in doping. The work of Thomson *et al.* [19] agrees with the conclusion of Trenkler, for the wearing of the metal-coated tips. However, they stress that with the metal-coated tips, much lower contact resistances can be obtained. As a solution to the wear of the tip, they suggest to use the intermittent mode to scan the surface, instead of the contact mode.

2.3 Our C-AFM system

THE AFM SYSTEM available is a Topometrix TMX2010, for which the C-AFM option is homebuilt (see figure 2.3). It consists of a computer-controlled (through a DAC-interface card) power supply with a range from $-10V$ to $+10V$. For practical use (as the measurement range is mostly between $-1V$ and $+1V$), a $1/10$-voltage divider is included in the system to get a better bias-resolution. The bias is applied between the conducting tip and the sample. The back of the sample (with Ohmic contact) is connected with a Keithley 616 electrometer, by the sample-holder. The electrometers current-sensitivity ranges from $10A$ to $10^{-14}A$, with a manual selection of the sensitivity. The electrometer acts as a $I - V$ converter between sample and computer, which registers the converted voltages.

Before discussing the tips and cantilevers that were used, we elaborate on the procedure to measure an I/V-characteristic with this homebuilt C-AFM. Firstly, an image can be made using the AFM in its normal operation mode. Once this overview image is made, one zooms in to make sure that the tip is above the contact. If the contact is still easily visualized on the CRT-screen of the apparatus (which uses lenses to get a good picture), it is not necessary to perform this topography-scan and the tip can be manually positioned above the contact. Then, the laser is switched off to avoid a photocurrent that would originate from the scattering of the laser light onto the sample. Doing this, the feedback mechanism of the AFM is interrupted, so we do not know what amount of force is applied to the tip. We manually lower the tip onto the contact and apply as much force as needed to establish an electrical contact. A photocurrent can be observed, due to the light of the internal microscope of the AFM. From literature [19] it is known that the force needed for electrical measurements is of the order of $\mu\mathrm{N}$, while for scanning purposes it is of the order of nN. Lantz *et al.* [20] also predict that if C-AFM is undertaken in air (they work in UHV), very large forces, of the order of μN, will be required to establish a stable electrical junction, due to

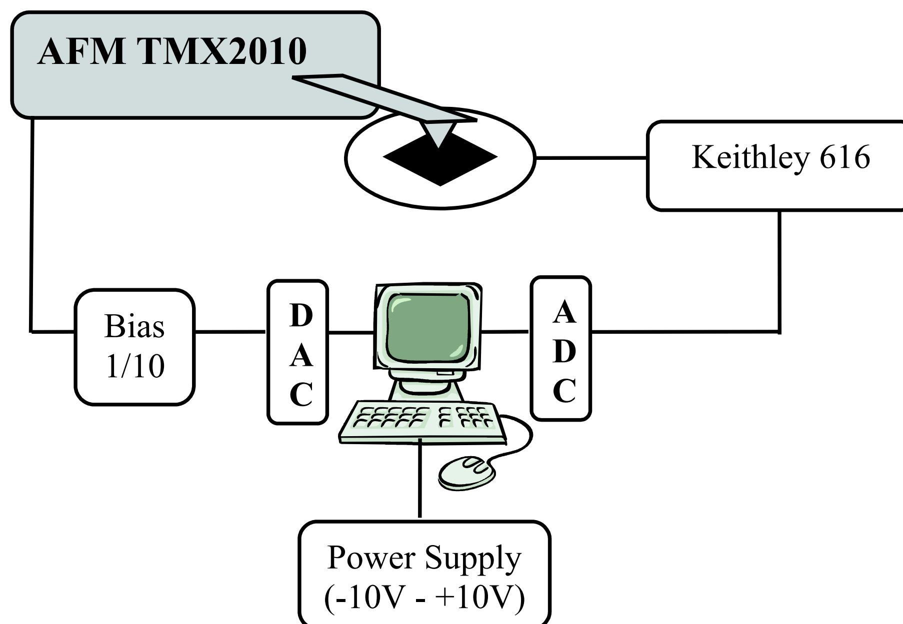

Figure 2.3: *Scheme of the homebuilt C-AFM system.*

contamination of the tip and sample surface.

Once this contact is established, we switch off the light and apply a bias to check if we still have electrical contact. If the current fluctuates, we can increase the pressure of the tip on the contact, by increasing the bias on the z-piezo, thus pushing the sample towards the tip. If we cannot establish a good, stable current, we repeat the process or replace the tip (wear of the coating). It is easier to establish a stable contact with a rather stiff cantilever (with a force constant of about 0.6 to 1.8 N/m) than with a more flexible cantilever (order of 50 mN/m). If a stable electrical contact is established, the bias-sweep and the current registration are started.

Two kinds of C-AFM tips were used in this research: Ultrasharp contact silicon cantilevers (and tips) with either a $25nm\ Pt$-coating, or a $20nmCr/20nmAu$ -coating on both sides (i.e. the tip side and the reflection side). The cantilevers are rectangular (see figure 2.4), and have different force constants. The tip has a height of $\approx 20\mu m$, a tip cone angle of less than $20°$ and the radius of the curvature is less than $35nm$ or $50nm$ for the Pt- or Cr/Au-coated tips, respectively. As shown in appendix A, there was no difference noticed between the two coatings, or the different force constants. We prefer the usage of Pt-coated tips, due to the longer lifetime of the coating.

To determine the series resistance of our measuring-unit (i.e. coming mainly from the tip-cantilever unit), I/V measurements were done on a gold layer with a Pt-coated tip and are shown in figure 2.5(a). A good Ohmic behaviour is observed, and

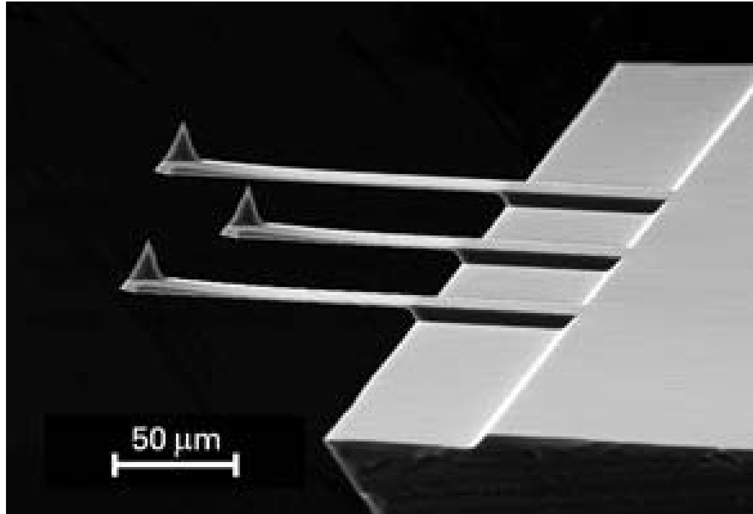

Figure 2.4: *SEM image of the cantilevers (and tips) used in the C-AFM research.*

from the measurements (and Ohm's law), an average series resistance of 407Ω is determined. There is a very good agreement between our value, and the one obtained by Thomson and Moreland [19]. For n-doped Si cantilevers coated with $45nm\ Pt$, they found a series resistance of 350Ω, measured on a $50nm$ gold layer.

Figure 2.5(b) shows a forward and reverse I/V-curve of a Au/n-GaAs Schottky contact, measured using the C-AFM. We can clearly see the rectifying behavior of the contact. Due to the time consumption of measuring the reverse part, we have restricted our other measurements to the forward part of the I/V-curve. We will be using these I/V characteristics to determine BHs and ideality factors for the Schottky contacts. Therefore, we determined the error on both parameters that originates from the measuring setup (see appendix A for more details):

$$\text{error}(\phi_B) = 0.003 \text{ eV and error}(n) = 0.009.$$

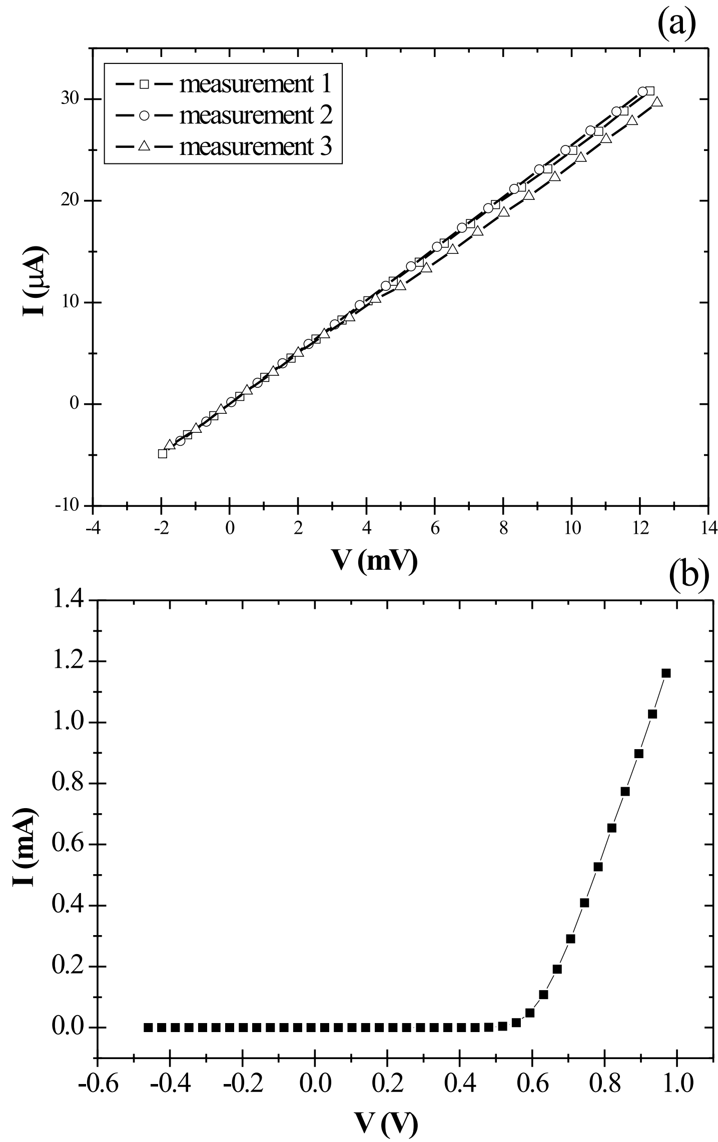

Figure 2.5: *(a) I/V-measurements of a gold layer with the Pt-coated tip shows a good Ohmic behaviour. (b) I/V-measurement on a Au/n-GaAs Schottky contact with a Pt-coated tip, shows a good rectifying behaviour.*

Bibliography

[1] G. Binnig, C. F. Quate, and C. Gerber. *Phys. Rev. Lett.*, 56(9):930, 1986.

[2] D. Rugar, H. J. Mamin, and P. Guethner. *Appl. Phys. Lett.*, 55(25):2588, 1989.

[3] G. Meyer and N. M. Amer. *Appl. Phys. Lett.*, 53(12):1045, 1988.

[4] Veeco Instruments Inc. *A practical guide to Scanning Probe Microscopy*. 2005.

[5] S. Morita, Y. Sugawara, and Y. Fukano. *Jpn. J. Appl. Phys. Part 1 - Regul. Pap. Short Notes Rev. Pap.*, 32(6B):2983, 1993.

[6] B. Alperson, S. Cohen, I. Rubinstein, and G. Hodes. *Phys. Rev. B*, 52(24):17017, 1995.

[7] P. Dewolf, J. Snauwaert, L. Hellemans, T. Clarysse, W. Vandervorst, M. Dolieslaeger, and D. Quaeyhaegens. *J. Vac. Sci. Technol. A*, 13(3):1699, 1995.

[8] A. Olbrich, B. Ebersberger, and C. Boit. *Appl. Phys. Lett.*, 73(21):3114, 1998.

[9] F. Houze, R. Meyer, O. Schneegans, and L. Boyer. *Appl. Phys. Lett.*, 70(26):3619, 1997.

[10] T. W. Kelley and C. D. Frisbie. *J. Vac. Sci. Technol. B*, 18(2):632, 2000.

[11] M. Freitag, M. Radosavljevic, W. Clauss, and A. T. Johnson. *Phys. Rev. B*, 62(4):R2307, 2000.

[12] H. Hasegawa, T. Sato, and C. Kaneshiro. *J. Vac. Sci. Technol. B*, 17(4):1856, 1999.

[13] T. Sato, S. Kasai, H. Okada, and F. Hasegawa. *Jpn. J. Appl. Phys. Part 1 - Regul. Pap. Short Notes Rev. Pap.*, 39(7B):4609, 2000.

[14] T. Sato, S. Kasai, and H. Hasegawa. *Jpn. J. Appl. Phys. Part 1 - Regul. Pap. Short Notes Rev. Pap.*, 40(3B):2021, 2001.

[15] T. Sato, S. Kasai, and H. Hasegawa. *Appl. Surf. Sci.*, 175:181, 2001.

[16] A. Bietsch, M. A. Schneider, M. E. Welland, and B. Michel. *J. Vac. Sci. Technol. B*, 18(3):1160, 2000.

[17] O. Schneegans, L. Boyer, F. Houze, R. Meyer, and P. Chretien. *J. Vac. Sci. Technol. B*, 20(5):1929, 2002.

[18] T. Trenkler, T. Hantschel, R. Stephenson, P. De Wolf, W. Vandervorst, L. Hellemans, A. Malave, D. Buchel, E. Oesterschulze, W. Kulisch, P. Niedermann, T. Sulzbach, and O. Ohlsson. *J. Vac. Sci. Technol. B*, 18(1):418, 2000.

[19] R. E. Thomson and J. Moreland. *J. Vac. Sci. Technol. B*, 13(3):1123, 1995.

[20] M. A. Lantz, S. J. O'Shea, and M. E. Welland. *Rev. Sci. Instrum.*, 69(4):1757, 1998.

Chapter 3

Experimental Details

ALL samples were prepared using $0.35mm$ thick, n-doped GaAs(100) wafers (Si doped), obtained from Wafer Technology Ltd. The average carrier concentration is $N_{\mathrm{D}} \approx 4$ x $10^{16}cm^{-3}$ and the resistivity varies from 0.076 to $0.078\ \Omega cm$. The wafers have a polished front side. Samples of 5 by $5\ mm^2$ were cut from the wafers.

The samples were degreased subsequently in boiling trichloroethylene C_2HCl_3, acetone CH_3COCH_3 and methanol CH_4O. Afterwards, they were chemically etched in a 3:1:1 (volume ratio) mixture of sulfuric acid H_2SO_4 (95%), hydrogenperoxide H_2O_2 (27%) and deionised (DI) water H_2O, at $80°C$. Immediately afterwards, they were dipped for $5s$ in a $1:1$ mixture of chloric acid $HCl(37\%)$ and DI water H_2O at room temperature, to remove the native oxide. Finally the samples were rinsed in DI water and dried with N_2.

Ohmic contacts were made at the back of the samples by thermal evaporation of In in a vacuum of about 10^{-5} mbar, with the substrate held at room temperature. This was followed by annealing the samples at $300°C$ for 10 min in an inert atmosphere (N_2).

For the fabrication of the Schottky contacts, Electron Beam Lithography (EBL) was used[‡]. This technique is comparable to standard lithography techniques, with the difference being the use of electrons to pattern the samples, instead of UV-light. Due to the shorter wave length of electrons, smaller structures can be patterned. For this, a JEOL scanning electron microscope (SEM), type JSM T-330, is used with a homebuilt lithography software. After cleaning the samples, a double layer of (positive) photoresist is spin-coated on the surface. The first photoresist layer is a $200nm$ thick poly(methyl methacrylate)/methacrylic acid copolymer (PMMA/MAA) layer, and is baked for 15 minutes at $165°C$. The top layer is $180nm$ of PMMA, baked for 30 minutes at $165°C$.

Using EBL, squares with different sizes are patterned in the photoresist. The

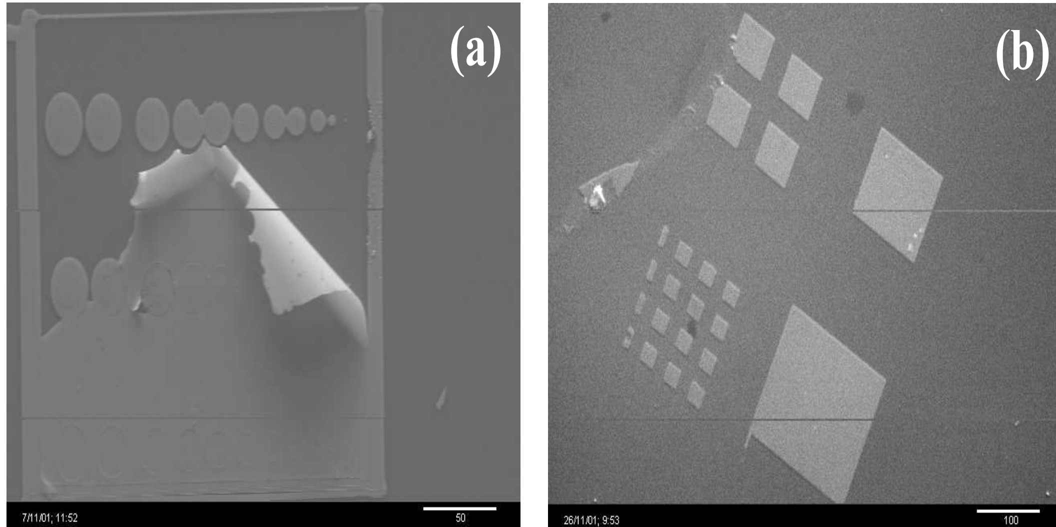

Figure 3.1: *SEM image of (a) the lift-off process (the marker indicates $50\mu m$) and (b) Au/n-GaAs contacts that were made by EBL and measured with C-AFM (the marker indicates $100\mu m$).*

lengths of the sides are: $150\mu m$, $100\mu m$, $50\mu m$, $20\mu m$, $10\mu m$, $9\mu m$, $8\mu m$, $7\mu m$, and $6\mu m$. There were also squares with sides of $2\mu m$, $1\mu m$ and $< 1\mu m$.

After e-beam patterning, the structures were developed in a MIBK (methyl-isobutyl-ketone):IPA (isopropanol) solution with 1:2 concentration at room temperature. Afterwards, they were rinsed in pure IPA and dried with N_2.

Prior to the gold evaporation, some of the patterned samples were dipped for 5 s in $HCl : H_2O$ and rinsed in DI water (see chapter 4 for further details and results). The Schottky contacts were made by evaporating $30nm$ gold onto the sample at a rate of $0.15nm/s$ in a vacuum better than $4 \times 10^{-6}\ mbar$, with a substrate temperature of $100°C$. Finally, a lift-off process was performed on the samples using acetone, slightly heated to maximum $30°C$. Figure 3.1 shows SEM images of an incomplete lift-off process (a) and of some Au/n-GaAs contacts that were typically made (b).

‡See appendix B for an illustration of the EBL process

Chapter 4

The SBH inhomogeneities in identically prepared Au/n-GaAs Schottky contacts

EVER since Tung published his PO theory, there has been research to find out more about the inhomogeneities and their influence on the Schottky contact. Furthermore, due to the downscaling in microelectronics, the influence of these inhomogeneities might become more pronounced, so a more complete characterisation of the SBH and its inhomogeneities is of interest. Then again, miniaturization can also help in the search for experimental evidence for the newly published BPT (see chapter 1): by downscaling the Schottky contacts, one might be able to distinguish more the influence of certain parameters and their (local or general) effect on the SBH. The development of the C-AFM technique supplied a promising characterisation technique to investigate the correlation between the inhomogeneities and the downscaling.

In this chapter, we first discuss the technical issues for measuring submicron Schottky contacts, followed by a more elaborate investigation of the 'micron' contacts (6 to $150 \mu m$).

4.1 The submicron Schottky contacts

THE EBL technique enables us to create diodes with small sizes, but it also allows us to create them with a certain shape and position relative to each other.

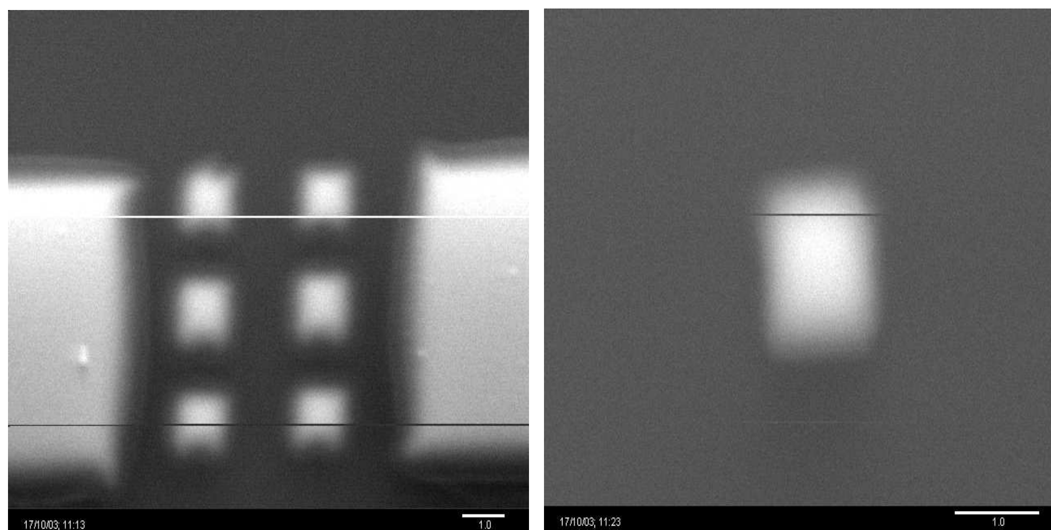

Figure 4.1: *SEM images of some small square-shaped contacts made using EBL. The length-scale (bottom right) is $1\mu m$ for both images.*

Figures 4.1 and 4.2 show some examples of the small-sized contacts that were fabricated using the EBL-technique. The (a)-parts of the figures illustrate the possibility for contact-placement, while the (b)-parts of the figures show a zoomed image of the contact to give a better idea of the size of the contact. Figure 4.3 shows AFM images of similar contacts.

The C-AFM setup should enable us to measure these small-sized contacts. As explained in section 2.3 (page 16), a topographic image (like figure 4.3(b)) is taken, and then the scanning range is zoomed in on the contact, to move the tip on top of the contact. Normally, one should be able to measure I/V-characteristics on these small contacts. However, we did not succeed in this.

Due to the necessity to block out any light, the feedback-mechanism (with laser) used for topographical scanning, needs to be switched off. This causes the tip to move upwards to its default position (above the surface). Theoretically, when the tip is lowered again, it should be at the same position as when the feedback-loop was cut. However, it seems that most of the time, this is not the case. Furthermore, when a first electrical contact was established between tip and small-scale contact, it was either not stable (in current at a fixed bias) or it disappeared after a short time.

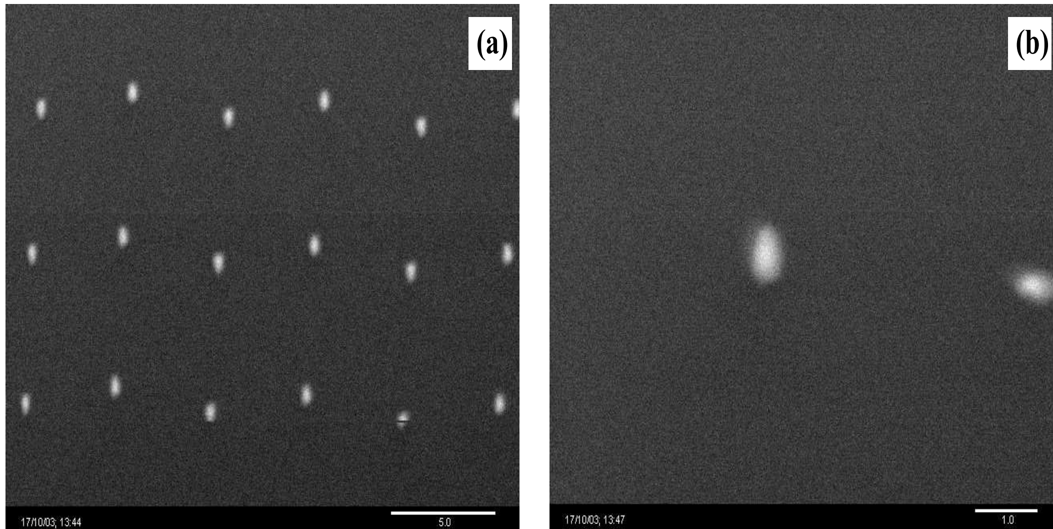

Figure 4.2: *SEM images of some small circular contacts made using EBL. The length-scale (bottom right) is either (a) $5\mu m$ or (b) $1\mu m$.*

The most probable cause for this failure, are the piezo elements which are used to position the sample. A small change in bias over the piezo element, can cause a small change in position of the sample. With the feedback-mechanism on, this change in position would be corrected for. We also believe that temperature changes originating from the current density or the environment, cause a small displacement of the sample. A different sample stage is the first step in solving the problem. A feedback-mechanism that doesn't use light (or at least not in the neighbourhood of the sample) is a necessity to keep the sample at its correct position.

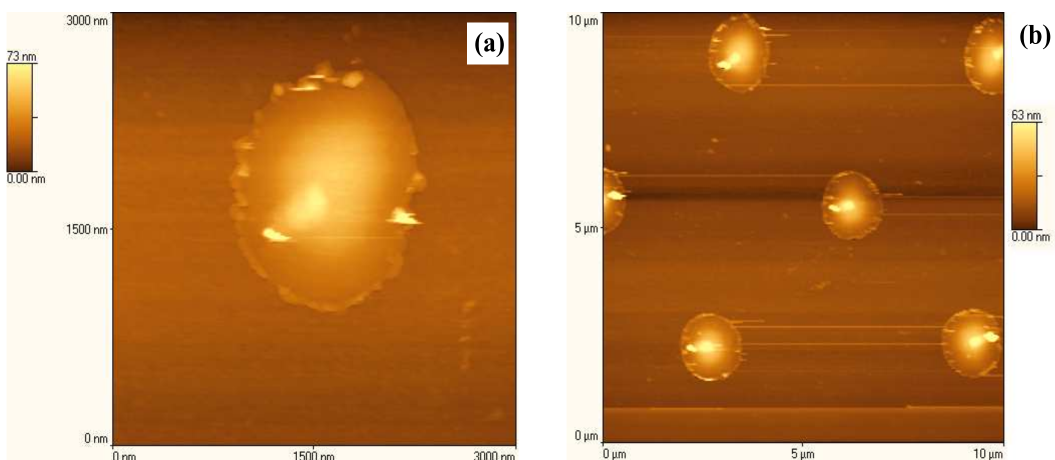

Figure 4.3: *AFM images of some small circular contacts made using EBL.*

4.2 The micron Schottky contacts

For the Au/n-GaAs Schottky contacts with dimensions ranging between $6\mu m$ and $150\mu m$, we observed a difference in electrical characteristics, depending on a certain fabrication process. *Group A* consists of 108 diodes, made using the standard EBL-technique, as described in chapter 3. *Group B* comprises 260 diodes who got an extra HCl-dip*, right before they were mounted in the evaporation machine for the Au deposition.

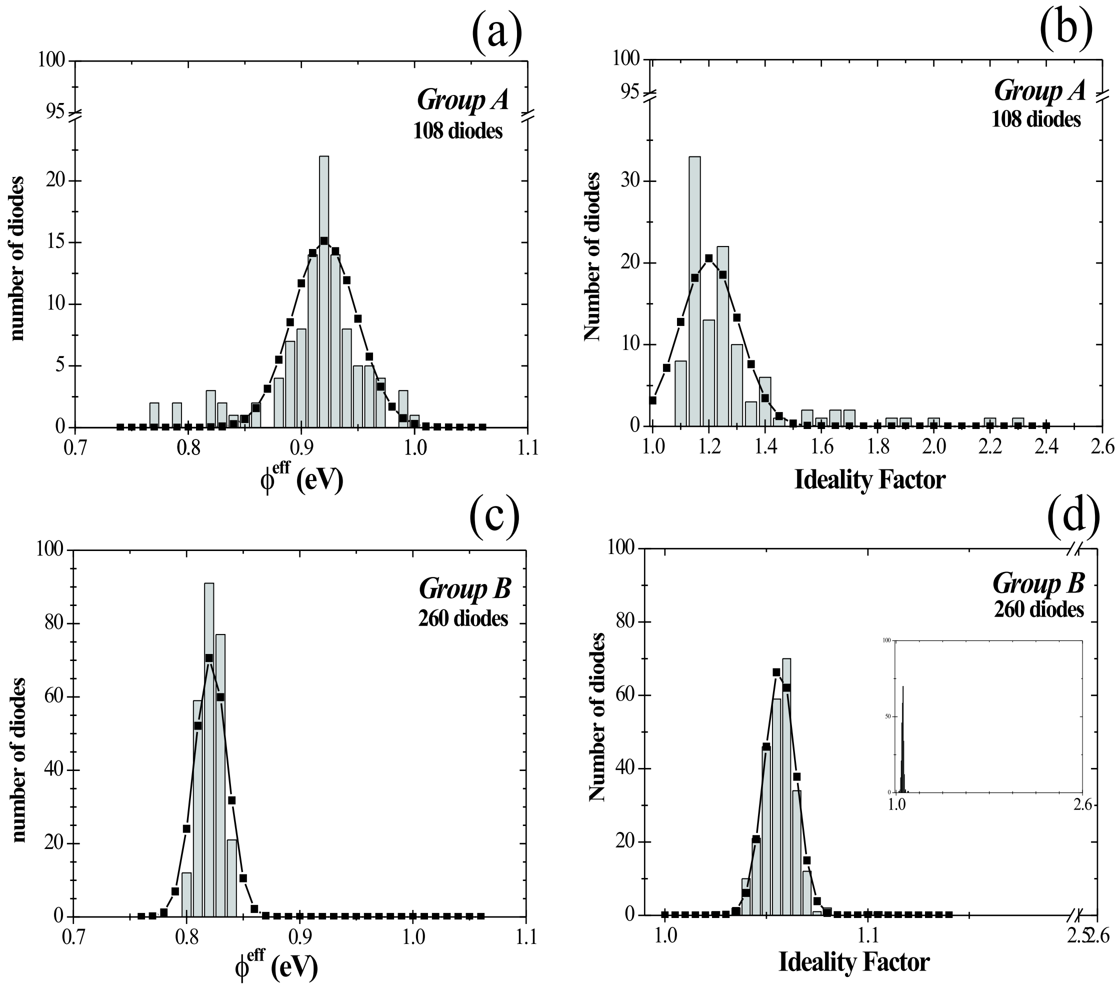

Figure 4.4: *Histograms of the SBH's ϕ^{eff} and ideality factors n^{eff} for the diodes of group A and group B, respectively, determined using the TE model. The inset in (d) shows the histogram on the same x-scale as in (b). Gaussian curves were fitted to the results.*

*The term "HCl-dip" is used here to describe both the 5s dip in $HCl : H_2O$ and the rinsing in DI H_2O.

For each diode, the SBH and ideality factor were calculated using the TE model (see equation 1.8) and we will refer to these as ϕ^{eff} and n^{eff}, respectively. All diodes within each group were identically prepared, but they exhibit a difference in SBH and ideality factor. The diodes were by no means ideal; their ideality factors are larger than the ideality factor determined by the image-force effect (see section 1.2) which is close to 1.01. Figure 4.4 shows a summary of the results, by means of a histogram for each group and each parameter. Concerning the ideality factors, one clearly observes that the *group B*-diodes are 'more ideal' (i.e. ideality factors closer to 1). The inset of figure 4.4(d) shows the histogram of the ideality factors of *group B* on the same x-scale as for the histogram for *group A*. This clearly shows that the spread on the ideality factors is much smaller for *group B*. The spread on the SBH's shows a similar behaviour, and one observes that the SBHs of *group A* are (generally) larger than for *group B*. Gaussian curves were fitted to the histograms, which supplied us with averages for the parameters:

		group A	*group B*
$< n^{eff} >$		1.202	1.057
$< \phi^{eff} >$	(eV)	0.920 $\pm$0.028	0.819 $\pm$0.010

From the histograms and the gaussian curves, one could conclude that the ideality factor and the SBH are higher for the diodes of *group A*, compared to the ones for *group B*. However, the histograms disregard the pronounced correlation between the effective barrier heights and the ideality factors [1–4]. They can illustrate a certain trend in the results, but other parameters should be used to make a good comparison between the two groups.

When lateral inhomogeneities occur, the saddle-point potentials in front of small-size patches are lower than the SBH of the surrounding regions. Tung [5] derived an analytical expression for the I/V characteristics of laterally inhomogeneous Schottky contacts, as explained in section 1.3.

The equation derived by Tung supplies us with a method of determining a homogeneous barrier height, which we note as Φ_{B0}. Using equation (1.11) with Φ_{B0}, σ, ρ_p as fitting parameters, all the experimental I/V characteristics were fitted. Figure 4.5 shows two experimental curves, each from a different diode, with their fitted curves. One can see that the fitted curves closely follow the experimental data. From all these PO parameters, obtained by fitting the curves, we derived the average values:

		group A	*group B*
$< \Phi_{B0} >$	(eV)	1.021$\pm$0.037	0.848$\pm$0.016
$< \sigma >$	($V^{1/3}cm^{2/3}$)	9.961$\times 10^{-5}$	6.226$\times 10^{-5}$
$< \rho_p >$	(cm^{-2})	3.790$\times 10^{7}$	5.116$\times 10^{10}$

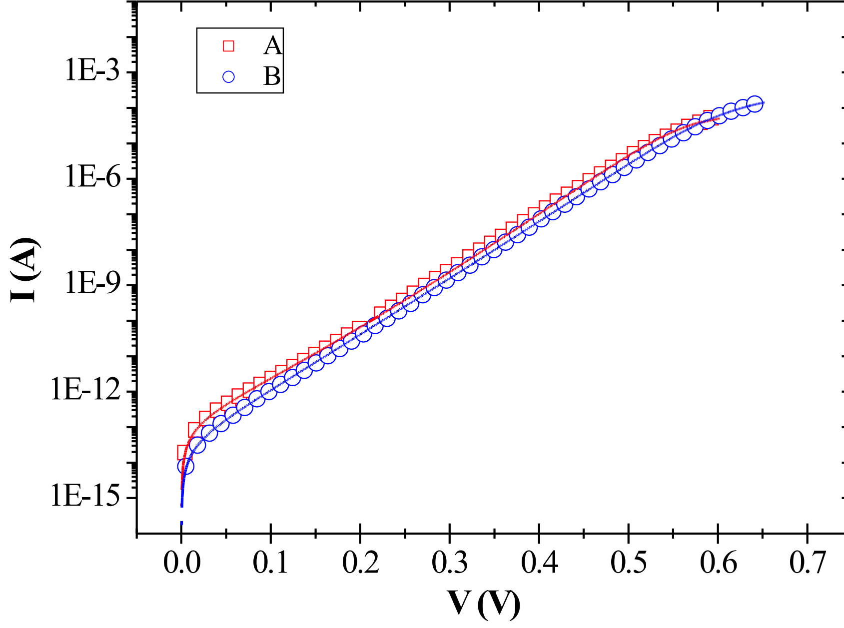

Figure 4.5: *I/V characteristics of two Au/n-GaAs Schottky diodes. The full lines are fits of Tung's equation for patchy diodes.*

Schmittsdorf *et al.* [1, 3] applied Tung's theory to experimental data of Ag-, Pb- and $Sn/Si(111)$ diodes, and found that the **linear extrapolation** of the experimentally observed ϕ^{eff} vs n^{eff} curves to n_{if} (the ideality factor of the ideal diode, with image-force included) gives the lateral homogeneous barrier height Φ_{lat}^{hom}. For completeness, we define n_{if} as [6]

$$n_{if} = \left[1 - \frac{1}{4} \left(\frac{q^3 N_{\rm D}}{8\pi^2 (\epsilon_{\rm s}\epsilon_0)^3} \right)^{1/4} \left(\Phi_{\rm B0} - V - \xi - \frac{k_{\rm B}T}{q} \right)^{-3/4} \right]^{-1} . \tag{4.1}$$

They used sets of $\phi^{eff}(n^{eff})$ with ideality factors of $n < 1.4$ to make their linear fitting. To get an idea of the upper limit for the ideality factor for our contacts (since we are using a different substrate), we did a similar simulation as Schmittsdorf *et al.*. We used the average values $< \Phi_{B0} >$ and $< \sigma >$ (obtained previously for each system), and varied the patch density ρ_p stepwise from *zero* to $1.0 \times 10^9 cm^{-2}$. Subsitituting these parameters in equation (1.11), an I/V -curve is calculated for each value of ρ_p. Using the TE formula (equation (1.8)), values for ϕ^{eff} and n^{eff} are calculated. Figure 4.6 shows the resulting $\phi^{eff}(n^{eff})$ -plot for both groups. Linear regions can be assumed for $n \leq 1.18$ and $n \leq 1.17$, for *group A* and *group B* respectively.

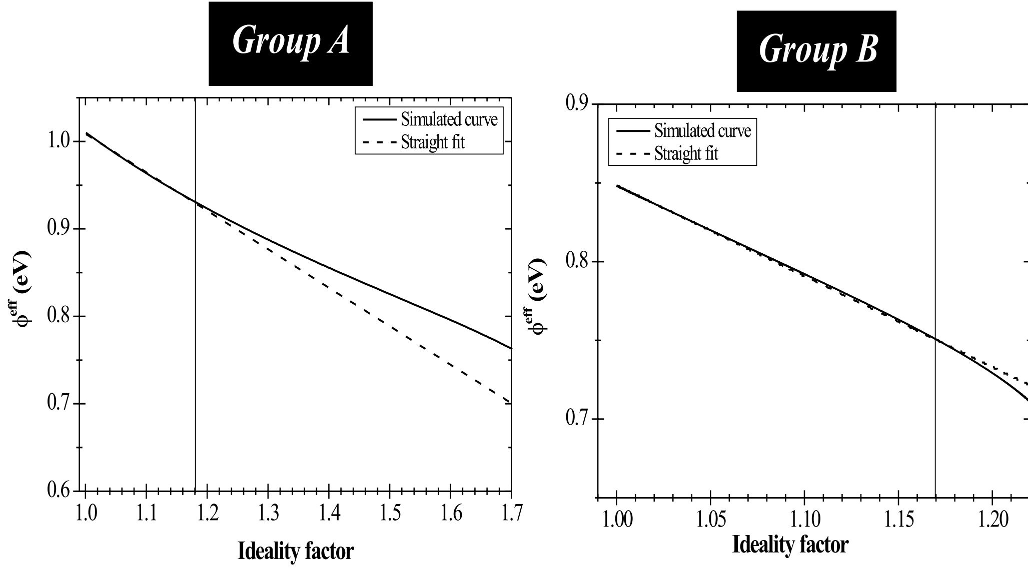

Figure 4.6: *The full lines are numerical simulations using the average PO parameters, and varying the patch density. The dashed line shows the linear relation for $\phi^{eff}(n^{eff})$-values up to $n \leq 1.18$ and $n \leq 1.17$ for group A and group B, respectively.*

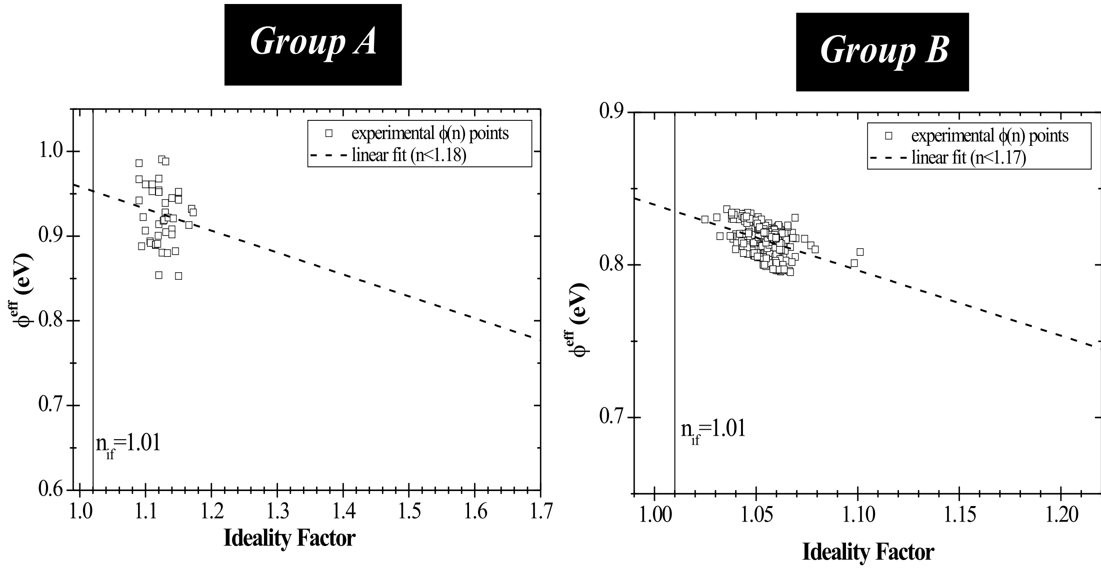

Figure 4.7: *Linear fit of the experimental $\phi^{eff}(n^{eff})$ data points. The linear extrapolation to $n_{if} = 1.01$ gives a lateral homogeneous barrier height $\Phi_{lat}^{hom}(A) = 0.959\ eV$ for group A, and $\Phi_{lat}^{hom}(B) = 0.835\ eV$ for group B.*

Knowing the upper limit for the linear fitting, we can determine the lateral homogeneous barrier height Φ_{lat}^{hom}, using the method of Schmittsdorf. Figure 4.7 shows these linear extrapolations to n_{if}, yielding:

		group A	*group B*
Φ_{lat}^{hom}	(eV)	0.959 ± 0.034	0.835 ± 0.010

Before discussing the results, we take a closer look at the pinch-off theory for a more physical picture of the patches. We can write the local lowering of the barrier height at the saddle point in front of a circular patch of radius R_p as [5]

$$\delta\Phi_p^{sad} = \Phi_{B0} - \Phi_B^{sad} = 3\left(\frac{1}{2}\frac{\Delta_p}{qV_{b0}}\frac{R_p^2}{W^2}\right)^{1/3} qV_{b0}, \tag{4.2}$$

where $W = [2\epsilon_s\epsilon_0(V_{b0}-\xi)/qN_D]^{1/2}$ is the depletion layer width, and Δ_p the patch parameter (see equation (1.10) on page 9 for more explanation). Furthermore, the standard deviation σ may be interpreted as an average patch-parameter

$$\sigma =< \gamma >= 3\left\langle(\Delta_p R_p^2/4)^{1/3}\right\rangle . \tag{4.3}$$

When we combine equation (4.2) and (4.3) with the averages obtained here, we can make an estimation of the BH lowering by

$$< \delta\Phi_p^{sad} >=< \Phi_{B0} - \Phi_B^{sad} >= \sigma\left(\frac{2}{qV_{b0}W^2}\right)^{1/3} qV_{b0}. \tag{4.4}$$

With these formulae, we calculate the following properties of the patches, for both groups:

		group A	*group B*
$< \delta\Phi_p^{sad} >$	(eV)	0.173	0.102
diameter $2R_p$	(nm)	18	12
% of W		10	7

Summary:

Table 4.1: *Summary of the results for the two groups of Au/n-GaAs Schottky contacts. The last column indicates the method used (TE: Thermionic Emission model, PO: Pinch-off model, S: Schmittsdorf method).*

		Group A	*Group B*	
$< \phi^{eff} >$	(eV)	0.920 ± 0.028	0.819 ± 0.010	TE
$< n^{eff} >$		1.202	1.057	TE
$< \Phi_{B0} >$	(eV)	1.021 ± 0.037	0.848 ± 0.016	PO
$< \sigma >$	($V^{1/3}cm^{2/3}$)	9.961×10^{-5}	6.226×10^{-5}	PO
$< \rho_p >$	(cm^{-2})	3.790×10^{7}	5.116×10^{10}	PO
$< \delta\Phi_p^{sad} >$	(eV)	0.173	0.102	PO
diameter $2R_p$	(nm)	18	12	PO
Φ_{lat}^{hom}	(eV)	0.959 ± 0.034	0.835 ± 0.010	S

Table 4.1 gives an overview of the parameters that were discussed. The values for the homogeneous SBH determined using different techniques (PO-fitting and Schmittsdorf-method), agree within the range of the experimental error. One can see from figure 4.7 that the linear fit to the $\phi^{eff}(n^{eff})$ data is better for *group B* than for *group A*. This results, for *group A*, in a bigger difference between the PO homogeneous SBH and the lateral homogeneous SBH, although they are comprised within the error ranges. However, we may conclude that **both methods are reliable** for obtaining the value of the homogeneous SBH. Care should be taken when Schottky contacts with large ideality factors are researched, and for these the PO method is probably the most accurate to obtain the homogeneous SBH.

Furthermore, from table 4.1 one can see a clear difference between the two groups of diodes; the (homogeneous) SBH of *group A* diodes is always higher than the one for *group B* diodes. The difference between the diodes of the two groups, is a HCl-dip before gold deposition. A HCl-treatment is known in the GaAs-fabrication process to remove oxide layers. The oxygen contamination, which would still be present in *group A* diodes, can originate from the EBL-fabrication process. During the fabrication, PMMA-resist layers are used, and also chemical solvents containing much oxygen, like IPA and MIBK (see chapter 3). Barbe *et al.* [7] reported the growth of thin oxide layers on GaAs in methanol. We believe a similar process occurs here, only in a more limited amount (i.e. a very thin oxide layer).

Biber *et al.* [8] studied the effect of an anodic oxide growth on Au/n-GaAs Schottky contacts. They found an increase by at least $110\ meV$ due to the oxide. This is comparable to the difference we observe between the diodes of the two groups. Furthermore, Forment *et al.* [9] observed a higher SBH for electrochemically-deposited Au/n-GaAs diodes than for vacuum-deposited ones. This difference is explained by the presence of a dipole layer containing oxygen at the MS interface of the electrochemical contacts. Because of the large electronegativity value of O, as compared to Au, it can be assumed that a $Au^{\delta+} - O^{\delta-}$ dipole is formed. The voltage drop across this interfacial dipole then leads to an increase if the SBH.

Our results confirm these previously obtained results, and show the possibility to modify the SBH for vacuum-deposited samples using organic solvents. Even more, as a consequence of the PO model, where only patches with a lower SBH are considered (see [5]), we find the 'high SBH' as the homogeneous SBH for the *group A* diodes. From the characterisation of the patches we found a BH-lowering of $\approx 0.173\ eV$, which is comparable to the value found by Biber *et al.*. So one could visualize the *group A* diodes as having a SBH dominated by the $Au^{\delta+} - O^{\delta-}$ dipole, with the patches being places where the 'normal' SBH (i.e. the SBH for *group B* diodes) is present.

The **experimental confirmation of this 'dipole-model'** is very important regarding the acceptance of the BPT-theory [10], which states that the SBH is locally determined by the bonding of the atoms forming the interface.

Bibliography

[1] R. F. Schmitsdorf, T. U. Kampen, and W. Monch. *J. Vac. Sci. Technol. B*, 15(4):1221, 1997.

[2] W. Monch. *J. Vac. Sci. Technol. B*, 17(4):1867, 1999.

[3] R. F. Schmitsdorf and W. Monch. *Eur. Phys. J. B*, 7(3):457, 1999.

[4] R. T. Tung. *Mater. Sci. Eng. R-Rep.*, 35(1-3):1, 2001.

[5] R. T. Tung. *Phys. Rev. B*, 45(23):13509, 1992.

[6] E.H. Rhoderick and R.H. Williams. *Metal-Semiconductor Contacts*. Clarendon Press, Oxford, second edition, 1988.

[7] H. Barbe, R. L. Van Meirhaeghe, and F. Cardon. *Semicond. Sci. Technol.*, 3(9):853, 1988.

[8] M. Biber, M. Cakar, and A. Turut. *J. Mater. Sci.-Mater. Electron.*, 12(10):575, 2001.

[9] S. Forment, R. L. Van Meirhaeghe, A. De Vrieze, K. Strubbe, and W. P. Gomes. *Semicond. Sci. Technol.*, 16(12):975, 2001.

[10] R. T. Tung. *Phys. Rev. Lett.*, 84(26):6078, 2000.

Part II

THIN FILM SOLID-STATE REACTIONS FORMING CARBIDES

Chapter 5

General properties of carbides

5.1 Introduction

WHEN looking to foreign atoms of all kinds in metal lattices, one will presumably stumble upon the term of ***Interstitial Alloy***. This term implies the existence of a pure metal lattice acting as a host to foreign atoms (of smaller size) which fill the room between the metal atoms (i.e. the interstices). However, this is only the case for the primary solid solutions (and defines this group of interstitial alloys), but still the term *interstitial alloy* is used in a more broadened sense. The most important interstitial alloys are the *interstitial compounds*, where the non-metal atom forms an integral part of the compound. Without it, the metal lattice would differ entirely. The ***interstitial compounds*** have proven their worth and many examples of such materials will feel familiar: *e.g.* certain silicides, hydrides (like in nickel-metalhydride (NiMH) batteries), and off course the carbides.

When reading the description of an interstitial alloy, steel was probably the first material that popped to mind. The most elementary steel is a solid solution of iron (Fe) and carbon. The first indication towards the fabrication of steel (and not iron) tools, can be found in China around 500 BC. Around 250 BC, quality steel was made in India and spread around the world. Nowadays, China is by far the top steel producing country. Of course, the steel produced nowadays has gone through a long period of modification, and it's no longer only carbon which is dissolved in the iron. Other atoms as chromium (Cr) and manganese (Mn) are added to improve certain properties, but also amounts of iron carbide (Fe_3C) are introduced into the steel. Steel has become a complicated subject, being a mixture of all these elements, and it is a research topic in its own right.

CARBIDES are interstitial compounds, where the non-metal atom is carbon. In this work, when we talk about carbides, we imply the transition metal carbides, where the metal is one of the transition metals. They have extremely high melting points, which procured them also with the name of *refractory carbides*. Besides being stable at high temperatures, they are extremely hard, and their hardness is retained to very high temperatures, which are typical ***ceramic*** properties. Therefore, carbides have found many applications in the industry of cutting tools and wear-resistant parts. Tungsten carbide (WC) and titanium carbide (TiC) are the main players in this field, and they can be found on the tips of the so-called 'diamond-coated' tools, and as scratch-resistant coatings in jewellery as wedding rings and watches. Carbides can also be found in more technologically advanced applications. WC is an efficient neutron reflector and can be used in the field of nuclear reactions (*e.g.* in nuclear weapons), niobium carbide NbC and zirconium carbide ZrC are used as refractory coatings in nuclear reactors. A (more peace-friendly) high-tech application is the use of carbides as heat shields for the atmospheric re-entry of space shuttles and similar vehicles.

In addition to their ceramic properties of high hardness and stability at high temperatures, carbides are also examined for their catalytic properties in a number of reactions. Noble metals have been the commonly used catalysts for many years, but carbides offer the potential to replace the expensive rare noble metal catalysts (Pt, Pd, Ru, Rh). A few 'hot' catalytic processes being researched are the elimination (hydrogenation) of the toxic carbon monoxide CO ($CO + 3H_2 \longrightarrow CH_4 + H_2O$) [1], and the decomposition of nitrogen monoxide NO (known from the polluting NO_x compounds produced by cars etc.) to N_2 and O_2 gas, without forming other pollutants [2]. Because of the lower production cost of the carbides, the carbides do not even have to be more active in catalyzing given reactions, compared with the noble metals.

The properties of some carbides will be summarized and discussed in section 5.2.

Looking at the applications of the carbides mentioned above, one can easily see that most of the research interest has gone to the mechanical properties of the carbides. Nevertheless, more and more research concentrates on the electrical properties of carbides, because there are now requirements for electrical materials that are hard, or that can sustain harsh environments. The conductivity of carbides is via electrons, not ions, but they have covalent, ionic and metal bonding, and therefore they are often named ***metallic ceramics***. It is within this area that our research finds its place. Some examples of this technologically advanced research on carbides are the use of carbides to contact advanced semiconductors containing carbon like silicon carbide SiC [3], diamond [4], and even carbon nanotubes (CNTs) [5].

Regarding the formation of carbide materials, one can roughly distinguish three forms of material appearance: powders, single crystals and thin films [6]. Each has its typical and most popular techniques for preparing the carbides. Growing carbide single crystals is done using specialized techniques (which we won't be discussing here) as the Verneuil technique, the Czochralski technique, and other. The most common powder-metallurgy technique is the direct reaction of metal or metal hydride powders with carbon. These and other reactions used are summarized in Table 5.1.

Table 5.1: *Preparation techniques for carbide powders.*

Methode	Reaction
Direct reaction of metal with carbon	$M + C \longrightarrow MC$
Direct reaction of metal hydride with carbon	$MH + C \longrightarrow MC + H_2$
Reaction of the metal oxide and excess carbon in inert or reducing atmosphere	$M_xO_y + C \longrightarrow MC + CO$
Reaction of the metal with a carburizing gas	$M + C_xH_{2x+y} \longrightarrow MC + H_2$ $M + CO \longrightarrow MC + O_2$
Reaction of the metal halide or carbonyl vapour with hydrogen	$MCl_n + C_xH_{2x+y}$ $\longrightarrow MC + HCl + (C_qH_r)$ $M(CO)_n + H_2$ $\longrightarrow MC + (CO, CO_2, H_2, H_2O)$

These powder-based methods require several hours of annealing at temperatures over $2000°C$, with a great influence of these parameters on the homogeneity and final composition of the carbide. An advantage to the high temperatures used, is that the carbide can be purified from oxygen contamination under certain conditions, such as a good vacuum.

Thin films of carbides are probably the most useful for applications, especially if one considers the electronics industry. Some possible applications include: interconnects that do not suffer from electromigration, diffusion barriers, high-temperature resistors, and hard and corrosion-resistant electrical contacts. The deposition technique most found in literature, is probably Chemical Vapour Deposition (CVD). Different gasses in a certain ratio are combined, and through the chemical reaction of these gasses, a thin film is deposited. As an example, Lundberg *et al.* [7] deposited WC films from a $WF_6/C_3H_8/H_2$ $(1 : 15 : 16)$ mixture. CVD is a relatively slow process, so other techniques are preferred for their more production-friendly deposition speed. *Co-evaporation* is the evaporation of the transition metal and of the carbon

from another source, at the same time. Similar to this is *co-sputtering*, where the materials are sputtered from different (one-element) targets, at the same time. In *reactive sputtering*, one adds a 'reactive' gas to the sputtering plasma (so extra to the Ar gas, used for sputtering). For carbide formation, methane CH_4 is the obvious choice for the reactive gas. Further, *sputtering from sintered compound-targets* and, last but not least, *sputtering of layered thin films* are also used. The latter technique is used in this work. Each deposition technique has its own essential parameters (like heat treatments, gas pressure, substrate temperature,...).

The goal of this work is to be a guide for the production of carbide thin films starting from sputtered (one-element) thin films, followed by a solid-state reaction. This kind of reaction is very important in the industry of micro-electronics. In silicon-based technology (i.e. the largest part of the micro-electronics industry), metal-silicon compounds (silicides) are widely used as contact materials, since they offer several advantages as compared to metal contacts. Firstly, unlike pure metals several silicide phases are thermodynamically stable in contact with silicon. Secondly, when silicides are formed by a solid-state reaction between metal and Si, contact formation can be achieved by means of a self-aligned process (SALICIDE) [8]. The solid-state reaction between the thin metal film and Si only occurs in those regions of a patterned substrate, where the metal is in direct contact with the Si (or C for the present case of carbides). Therefore, there is no need for alignment and lithographic patterning of the metal film, since the formation of the silicide will be automatically restricted to the contact region. One can expect the same advantages when using carbides to contact carbon-based semiconductors, and this depicts the relevance of this work towards the field of micro-electronics.

5.2 General properties of carbide materials

IN our research, we concentrate on the transition metal carbides, thus being a compound of carbon with a transition metal. Therefore, the properties discussed here will be limited to these carbide phases. Not all transition metals will form a stable phase with carbon, and by using the binary phase diagrams [9], we limited our research to the following: Ti, V, Cr, Mn, Fe, Zr, Nb, Mo, Hf, Ta, and W. Table 5.2 gives an overview of some basic properties of the transition metal carbide phases. As a reference, the melting point and hardness for tungsten are $3422°C$ and $350kg/mm^2$, respectively. Tungsten is known for its high melting point, and one can see that most of the carbides have similar melting points. Worth mentioning is that TaC has the highest melting point known for any material. For the hardness, the carbides outrun tungsten (and other metals) by far, and their hardness values lie between those of Al_2O_3 and diamond.

Table 5.2: *General properties of transition metal carbides. The crystal structure and density (g/cm^3) are obtained from crystallographic data, the melting point ($°C$), microhardness (kg/mm^2), and the heath of formation ($kJ/mole$) were obtained from different sources: (a) L.Toth [6]; (b) H.J. Goldschmidt [10]; (c) M. Karapet'yants [11].*

Carbide Phase	Crystal Structure	Density	Melting Point$^{(a)}$	Micro-hardness$^{(b)}$	Heath of Formation
			example metal		
W	bcc	19.25	3422	350	
			group IV		
TiC	fcc	4.94	3140	3200	-184.5^a
					-238.5^b
					-186.2^c
ZrC	fcc	6.57	3550	2600	$-196.6^{a,c}$
					-200.8^b
HfC	fcc	12.67	3890	2900	-209.5^a
					-338.9^b
					-226.8^c
			group V		
V_2C	hcp	5.67	2200	2140	-138.1^a
					-147.3^c
VC	fcc	5.60	2830	2850	-102.5^{a-c}
Nb_2C	hcp	7.80	3100		-194.5^a
					-376.6^b
					-145.6^c
NbC	fcc	7.79	3480	2400	-140.5^a
					-138.1^b
Ta_2C	hcp	15.22	3400	947	-208.4^a
					-384.9^b
					-197.5^c
TaC	fcc	14.48	3880	1800	-142.7^a
					-159.0^b
					-150.6^c
			group VI		
Cr_3C_2	orth.r.	6.68	1895	1300	-69.0^a
					-131.8^b
					-103.0^c

continued on next page

continued from previous page

Carbide Phase	Crystal Structure	Density	Melting Point$^{(a)}$	Micro-hardness$^{(b)}$	Heath of Formation
Cr_7C_3	compl.hex.	6.92	1665	1600	-414.9^b
$Cr_{23}C_6$	compl.cub.	6.97	1580	1000	-236.0^b
Mo_2C	hcp	9.06	2410	1479	-46.0^a
					-92.0^b
					-49.0^c
MoC	s.hex.	9.46	2690	1800	-12.6^a
					-10.5^b
					-17.7^c
W_2C	hcp	17.2	2800	1450	$-52.7^{a,b}$
WC	s.hex.	15.77	2755	2100	-40.5^a
					$-35.1^{b,c}$
group VII					
Mn_3C	orth.r.	6.90	1520		-288.7^b
					-15.6^c
Mn_7C_3	compl.hex.	7.37	1340		
$Mn_{23}C_6$	compl.cub.	7.46	1010		
group VIII					
Fe_3C	orth.r.	7.20	1650		31.4^b
					24.9^c

Most of the carbides have close-packed or nearly close-packed structures, where the metal atoms are on the lattice sites and the smaller carbon atoms are inserted into the interstitial sites. This description is often named 'the interstitial model', and has the advantage of being the easiest to visualize and is the most familiar. Another way of visualizing the lattice is the model of 'coordination polyhedra'.

In 1931, Hägg formulated an empirical rule, regulating the structure types formed by transition metal carbides. Although minor exceptions to the rule have been found, its general features remain valid. According to Hägg, the structure of transition-metal carbides is determined by the radius ratio:

$$H = r_C/r_{Me},$$

where r_C and r_{Me} are the radius of the carbon atom and the transition metal atom, respectively. The Hägg rule states that if $H > 0.59$, then the transition metal and interstitial carbon form complicated structures. However, if $\boldsymbol{H < 0.59}$, the metal atoms will form a simple structure as face-centered cubic (fcc), body-centered cubic (bcc), hexagonal close-packed (hcp), or simple hexagonal (s.hex.), and the carbon atoms are accomodated in the largest interstitial sites of the simple metal host structure. The interstitial site must necessarily be smaller than the interstitial atom which

it is to accommodate; otherwise there will be insufficient bonding between the metal and nonmetal atoms and the structures will become unstable. On the other hand, the interstitial site cannot be too much smaller than the interstitial atom; otherwise the presence of the interstitial atom will expand the metal host lattice to the point where the metal-metal interactions will become weak and the structure will lose its stability. Table 5.3 gives an overview of the values for the radius ratio H, for the transition metals that form carbide phases. Comparing these values with the crystal structures noted in Table 5.2, one can see that the Hägg-rule is accurate, as we get more complex structures for the Fe, Mn and Cr carbide phases.

Table 5.3: *Radius ratio H for transition metal atoms that form carbide phases. Reproduction from L.E. Toth [6].*

Element	Ti	V	Cr	Mn	Fe
Atomic Radius	1.467	1.338	1.267	1.261	1.260
C/Me ratio (H)	0.526	0.576	0.609	0.611	0.612
Element	Zr	Nb	Mo		
Atomic Radius	1.597	1.456	1.386		
C/Me ratio (H)	0.483	0.530	0.556		
Element	Hf	Ta	W		
Atomic Radius	1.585	1.457	1.394		
C/Me ratio (H)	0.486	0.529	0.553		

Hägg also calculated the H-values for the interstitial sites of the simple metal lattices, and concluded that the tetrahedral interstitial sites are too small to accommodate the carbon atoms. Therefore, only the octahedral interstitial sites for the fcc, bcc and hcp lattices, and the trigonal prism interstitial sites for the s.hex. lattices are occupied. Figure 5.1 shows where these sites are located in the fcc, hcp and simple hex. lattice. If all of the octahedral sites in a (simple) fcc metal lattice would be filled, one would obtain the $B1$(NaCl)-structure, as is the case for TiC, ZrC, HfC, VC, NbC, and TaC. Randomly filling half of the interstitial sites in the hcp lattice, will result in the L_3'-structure (V_2C, Nb_2C, Ta_2C, Mo_2C, and W_2C) and occupation of trigonal prism interstitial sites in the s.hex. structure will result in the WC structure (MoC and WC).

The reason why the interstitial model is used to visualize the carbide structures, i.e. seeing a (nearly-) close-packed metal lattice with interstitially located carbon atoms, is a very important property of the carbides, namely their **defect structure**. Most carbide phases can exist over a certain range of composition, which means that large amounts of vacancies can occur on the carbon sites, and thus, the original $B1$, L_3' or WC (or other) structure of the carbide phase might not be so easily recognized. The presence of vacancies significantly affect the physical properties of the carbides, as they will act as powerful scattering centers for electrons and phonons.

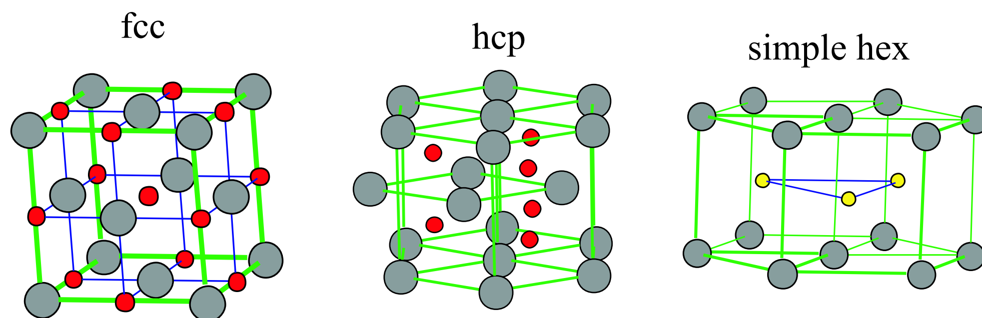

Figure 5.1: *Illustration of the mentioned crystal structures: face centered cubic (fcc), hexagonal close-packed (hcp), and simple hexagonal. The metal atoms are marked grey, the octahedral interstitial sites have been marked red and the trigonal prism interstitial sites yellow.*

The properties affected include the lattice parameters and density, the Hall coefficient, the transition temperature to the superconducting state, but also the thermodynamic, magnetic and electrical properties. As it is important to know the range of composition for the carbide phase, we will be showing the binary phase diagrams for each system, in its appropriate section.

Though it is not within the scope of our work, we do want to direct attention to the complexity of the bonds in carbides. The bonding in transition metal carbides involves simultaneous contributions of metallic, covalent, and ionic bonding to the cohesive energy. Several theories have put the metal-nonmetal bonds in the center of their attention, while other theories emphasized the interstitial nature of the carbon, and thus stress the metal-metal bond. Using the latter theory, the metallic conductivity of the carbides and the wide range of composition over which the carbides are stable, have been explained. Vines *et al.* [12] showed from DFT calculations, that the chemical bonding in transition metal carbides is strongly covalent. Nevertheless, there is also an indication that some metal to carbon charge transfer occurs. On the other hand, Goldschmidt [10] showed that the melting points decrease from carbides over nitrides to oxides (also interstitial alloys), which can be explained by the dominance of the metal-nonmetal bonds in these phases. There is a decrease in the number of electrons contributed to the metal atom, when going from carbon to nitrogen and oxygen. Consequently, these bonds are progressively weakened and the melting points are decreased. This small example shows that the bonding in carbides is really a mixture of metal-metal and metal-nonmetal interactions. Both are important and it is difficult to assign a relative importance to each of them.

Bibliography

[1] P. M. Patterson, T. K. Das, and B. H. Davis. *Appl. Catal. A-Gen.*, 251(2):449, 2003.

[2] J. X. Wang, S. F. Ji, J. Yang, Q. L. Zhu, and S. B. Li. *Catal. Commun.*, 6(6):389, 2005.

[3] S. K. Lee, C. M. Zetterling, M. Ostling, J. P. Palmquist, H. Hogberg, and U. Jansson. *Solid-State Electron.*, 44(7):1179, 2000.

[4] T. Tachibana, B. E. Williams, and J. T. Glass. *Phys. Rev. B*, 45(20):11975, 1992.

[5] R. Martel, V. Derycke, C. Lavoie, J. Appenzeller, K. K. Chan, J. Tersoff, and P. Avouris. *Phys. Rev. Lett.*, 87(25), 2001.

[6] L.E. Toth. *Transition Metal Carbides and Nitrides*, volume 7 of *Refractory Materials, A Series of Monographs*. Academic Press, New York, 1971.

[7] N. Lundberg, M. Ostling, C. M. Zetterling, P. Tagtstrom, and U. Jansson. *J. Electron. Mater.*, 29(3):372, 2000.

[8] S. L. Zhang and M. Ostling. *Crit. Rev. Solid State Mat. Sci.*, 28(1):1, 2003.

[9] T. B. Massalski. *Metall. Trans. B*, 20(4):445, 1989.

[10] H. J. Goldschmidt. *Interstitial Alloys*. Butterworths, London, 1967.

[11] M.Kh.; Karapet'yants and M.K. Karapet'yants. *Thermodynamic constants of inorganic and organic compounds*. Ann Arbor - Humphrey Science Publishers, London, 1970.

[12] F. Vines, C. Sousa, P. Liu, J. A. Rodriguez, and F. Illas. *J. Chem. Phys.*, 122(17), 2005.

Chapter 6

Experimental Details

ALL samples were made, starting from silicon wafers with a SiO_2 layer deposited at $950°C$. This gives a dense oxide-layer, which disables any reaction with the silicon underneath. The base layer above this SiO_2, is a 200nm sputter deposited amorphous carbon layer. The metals examined are: titanium Ti, vanadium V, chromium Cr, manganese Mn, iron Fe, zirconium Zr, niobium Nb, molybdenum

I	II	IIIb	IVb	Vb	VIb	VIIb	----VIIIb----			Ib	IIb	III	IV	V	VI	VII	VIII
H																	He
Li	Be											B	C	N	O	F	Ne
Na	Mg											Al	Si	P	S	Cl	Ar
K	Ca	Sc	Ti	V	Cr	Mn	Fe	Co	Ni	Cu	Zn	Ga	Ge	As	Se	Br	Kr
Rb	Sr	Y	Zr	Nb	Mo	Tc	Ru	Rh	Pd	Ag	Cd	In	Sn	Sb	Te	I	Xe
Cs	Ba	Lu*	Hf	Ta	W	Re	Os	Ir	Pt	Au	Hg	Tl	Pb	Bi	Po	At	Rn

Figure 6.1: *Periodic table of the elements. The metals that form stable carbide phases with carbon and that are researched are marked in green; the metals which form stable carbide phases, but haven't been researched, are marked in yellow yellow; the metals that do not have stable carbide phases are marked in red; for the elements that haven't been marked, there was no binary phase diagram available.*

Mo, hafnium Hf, tantalum Ta, and tungsten W. They were sputter deposited on top of the base-layer. The sputtering was done at a base pressure of $2 \times 10^{-7} mbar$ and an argon working pressure of $5 \times 10^{-3} mbar$. Some of the metals (Cr, Mn and V) were also deposited using e-gun evaporation at a base pressure of $10^{-6} mbar$. When used, the capping layers (i.e. the layers on top of the metal layers) were sputtered after the metal deposition, without breaking the vacuum. Samples were prepared in Gent and in IBM Research, and for the latter we gratefully thank Mr. R.A. Carruthers.

The *in situ* X-ray diffraction (XRD) measurements were performed at the X20C-beamline of **the National Synchrotron Light Source (NSLS) at Brookhaven National Laboratory (BNL)**. During annealing, the sample is continuously illuminated by an intense beam of monochromatic X-rays (λ = 0.177 to 0.180 nm). During the measurement, the samples were heated from $100°C$ to $1100°C$ in a purified He-atmosphere, at different ramp rates (from $0.3°C/s$ to $27°C/s$). There is a $\pm 3°C$ error on temperature registration for the *in situ* measurements. Diffracted photons from the sample are continuously detected by an array of photodiodes covering $14°$ in 2θ. Acquisition times can vary from 100 ms to several seconds depending on the annealing conditions. The standard experiments were done at $3°C/s$ in a He atmosphere, with an acquisition time of 0.5s. If other conditions are used, they will be mentioned. The *in situ* XRD measurements will be shown graphically (e.g. see figure 7.2 on page 57) either in grey-scale or in colour. For the gray-scale, the highest intensity will be coloured black, while for the colour-scale, red is the highest and blue the lowest

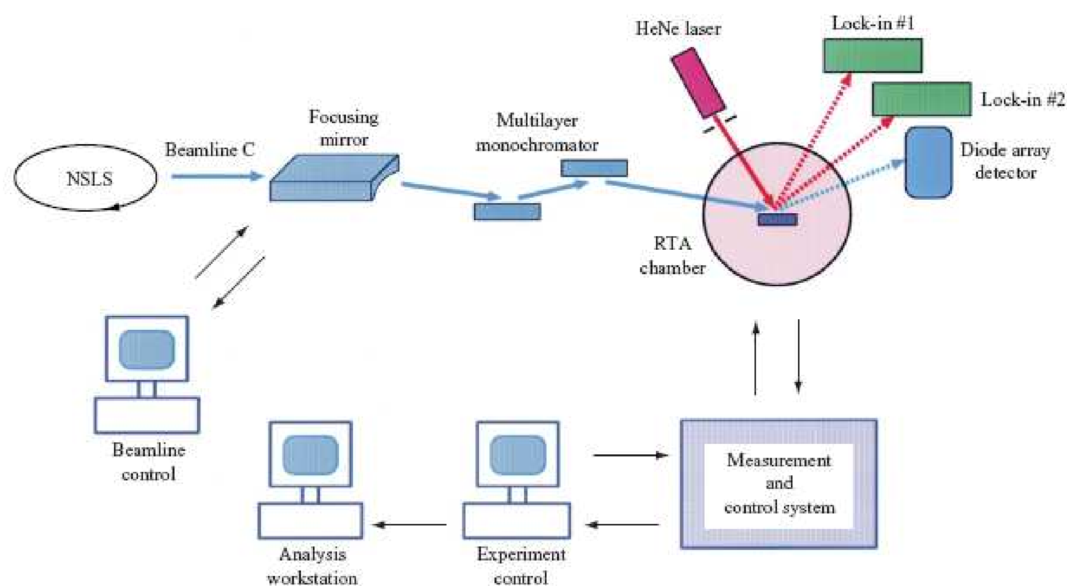

Figure 6.2: *Schematic overview of the in situ setup at the X20C-beamline at the National Synchrotron Light Source, Brookhaven National Laboratory, New York, USA (reproduction from Jordan-Sweet [1]).*

intensity. On both there will also be contour lines, indicating a same level of intensity.

The *ex situ* XRD measurements were done in our laboratory using a Bruker D8 Discover, equipped with a $CuK\alpha$ ($\lambda = 0.154nm$) x-ray source and a Vantec linear detector.

Annealings for the *ex situ* XRD measurements and XPS measurements, were done using the *in situ* setup at Ghent University. It was evidenced by Deduytsche [2] that the temperature calibration is within $\pm 3°C$ identical to the setup at BNL. This allows us to reproduce the experimental conditions used at the X20C-beamline.

The X-ray Photoelectron Spectroscopy (XPS) depth profile measurements were performed on a Perkin-Elmer Phi 5500 system. Photoelectrons are emitted from a sample upon irradiation with X-rays ($AlK\alpha$ energy), and the energy of these photoelectrons is measured using a hemispherical analyzer. Depth profiling is obtained by alternating the photoelectron measurements with sputtering of the surface over a certain time. The XPS data was analyzed using the Multipak© software from Physical Electronics. XPS was done to get information on the phase composition of the samples.

Rutherford Backscattering Spectroscopy (RBS) was used for contamination and thickness measurements, which were done at IBM Research. We acknowledge Mr. A.J. Kellock for these measurements. High-energy (2 to $4MeV$), low mass ions are scattered by the sample and collected at a scattering angle. By measuring the energy-loss of the ions, the chemical composition of the sample can be deduced. Because of the gradual energy loss as the ions penetrate the sample, a depth profile can also be obtained.

Bibliography

[1] J. L. Jordan-Sweet. *IBM J. Res. Dev.*, 44(4):457, 2000.

[2] D. Deduytsche. *An in-situ study of the stability of thin Ni-silicide layer*. Ph. d. thesis, Ghent University, 2006.

Chapter 7

Thin film solid-state reactions forming carbides

ELEVEN transition metals have been examined in a thin film solid-state reaction, to form transition metal carbides. Figure 6.1 gives a visual overview of the metals researched. From the binary phase diagrams [1] one can learn that there are a few other metals which form a stable carbide phase. These are also marked in figure 6.1, but weren't included in our research. In the following sections, our results (for the phase formations) will appear in order of the atomic number of the metal.

7.1 The Titanium - Carbon system

THE 22nd element of the periodic table was discovered in 1791 by William Gregor and rediscovered in 1795 by M. H. Klaproth, who named it *Titanium*, the Latin word for *Earth*. It's most noteworthy characteristic is its combined strength and light weight. Titanium exhibits allotropy, as below $880°C$ it has a hexagonal structure, while at higher temperatures it changes to a cubic structure. Table 7.1 gives a comparison between some basic properties of the metal and the carbide. Again, it can be seen that the carbide has a very high melting point, and is much harder than the metal.

Figure 7.1 shows the binary phase diagram for the Ti-C system, and one can observe that the only stable carbide phase is the monocarbide TiC, with quite a broad range of composition. From the phase diagram, we have estimated the composition for TiC_x to range between $0.70 \leq x \leq 0.98$, with x being the carbon-to-metal ratio. Worth mentioning is that the binary phase diagrams have an x-scale showing the atomic percentage of carbon. This means that for homogeneous TiC, the atomic

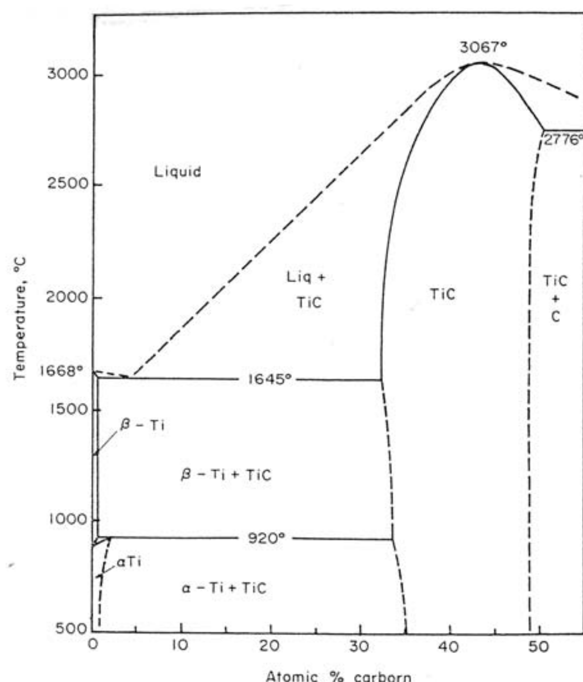

Figure 7.1: *Binary phase diagram for the Ti-C system. The broad range of composition for the TiC phase can be clearly seen. Reproduction from L.E. Toth [2]*

percentage of carbon will be 50%, while the carbon-to-metal ratio x will be 1.

It has been reported [3] that TiC_x phases exist that are still stable with a carbon-to-metal ratio as low as 0.56. This means that almost half of the available octahedral C sites in the fcc lattice are vacant.

Table 7.1: *Comparison between some basic properties of the pure metal Ti, and the carbide phase TiC.*

	Ti	**TiC**
Crystal Structure	hex.	fcc
Melting Point $(°C)$	1668	3140
Density (g/cm^3)	4.51	4.94
Moh's hardness	6	8-9
Electrical resistivity $(\mu\Omega cm)$	40	68
Thermal conductivity $(W/K\ m)$	21.9	17.2

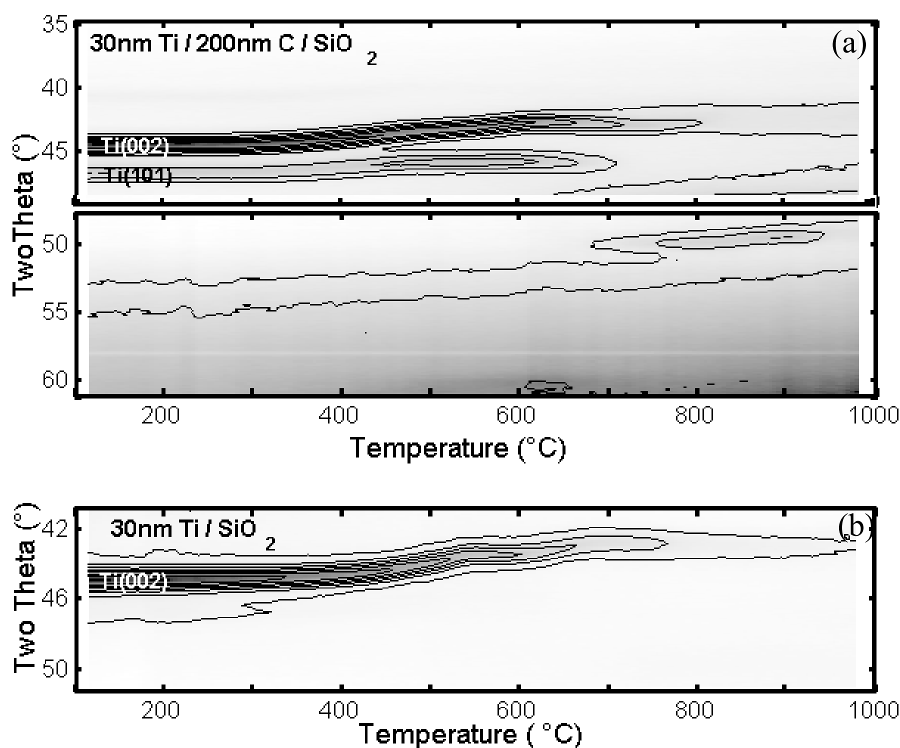

Figure 7.2: *(a): In situ XRD measurement of 30nm of Ti on 200nm C (on SiO_2), annealed from $100°$ to $1000°C$. (b): Same experiment for 30nm Ti on SiO_2.*

To study the solid-state reaction between carbon and titanium, we performed *in situ* XRD measurements in a temperature range from $100°C$ to $1000°C$, of which figure 7.2(a) shows the 2θ windows from $35°$ to $61°$. At the start of the experiment, the (002) and (101) peaks of the hexagonal Ti can be observed. Around $500°C$, one can observe the metal peaks shifting towards lower 2θ values, which means that the d-spacing is increasing. Both carbon and oxygen could inflict this shift, and from this measurement it is impossible to tell which species is introduced into the metal lattice. Oxidation of the metal layer is suspected when looking at figure 7.2(b), where a Ti layer on SiO_2 was annealed under the same conditions as the previous samples. Around $500°C$, there is the same shift of the metal peak towards lower 2θ values. As there is no C present in this sample setup, only the possibility of oxidation remains. It is known from literature, that Ti readily oxidizes, and even as-deposited films contain a certain amount of oxygen.

Other techniques should be used to get an idea of the oxygen concentration, and the shift of the metal peak in the XRD diagram can only be used as a first guidance. Figure 7.3 shows RBS-measurements done on samples quenched at different temperatures: the red and the black line are both for 30nm *as-deposited* Ti on 200nm C

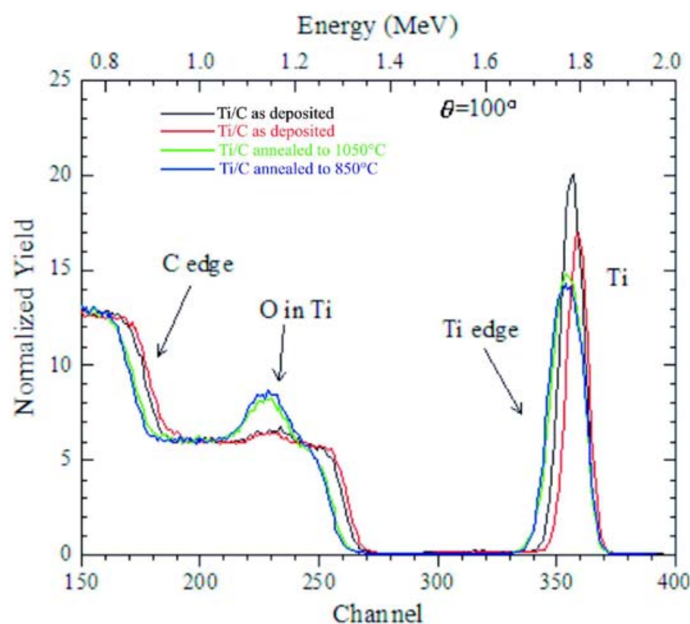

Figure 7.3: *RBS measurement on $Ti/C/SiO_2$ samples, as deposited (black and red lines), annealed to $850°C$ (blue line), and annealed to $1050°C$ (green line). The first two and the last two, respectively, have similar spectra.*

on SiO_2, the blue line is on a sample annealed to $850°C$, and the green line on a sample annealed to $1050°C$. Oxygen (marked on the figure) can clearly be observed in the annealed samples, but also in the as-deposited samples, there is a smaller bump noticeable, as was mentioned before. The oxidation during the annealing, can either be a reaction with the oxygen impurities left in the annealing atmosphere, or with oxygen that was present in the substrate. RBS has evidenced that the latter option is highly unlikely, as there was no sign of oxygen in the C layer (detection limit of RBS is around 3 at.%).

As the oxygen mainly originates from outside the sample, the logical way to avoid oxidation is to apply a capping layer which acts as a diffusion barrier for oxygen. Therefore, different capping layers were applied on top of the metal layers: 30nm C, 5nm Ta, 5nm W, 5nm Si, and 30nm TiN. To find out which of the capping layers were effective to block the oxygen out of the sample, *in situ* XRD measurements were done on these samples, and these can be seen in figure 7.4. As a reference, the experiment without a capping layer has also been included in the figure. The samples capped with Ta or W have a same shift towards lower 2θ values, similar to the uncapped sample. The Ti peaks in the sample with TiN capping layer, are a bit more difficult to follow ($Ti(002)$ and $Ti(101)$ around $2\theta \approx 45°$ and $\approx 47°$, respectively), but they also show a similar shift.

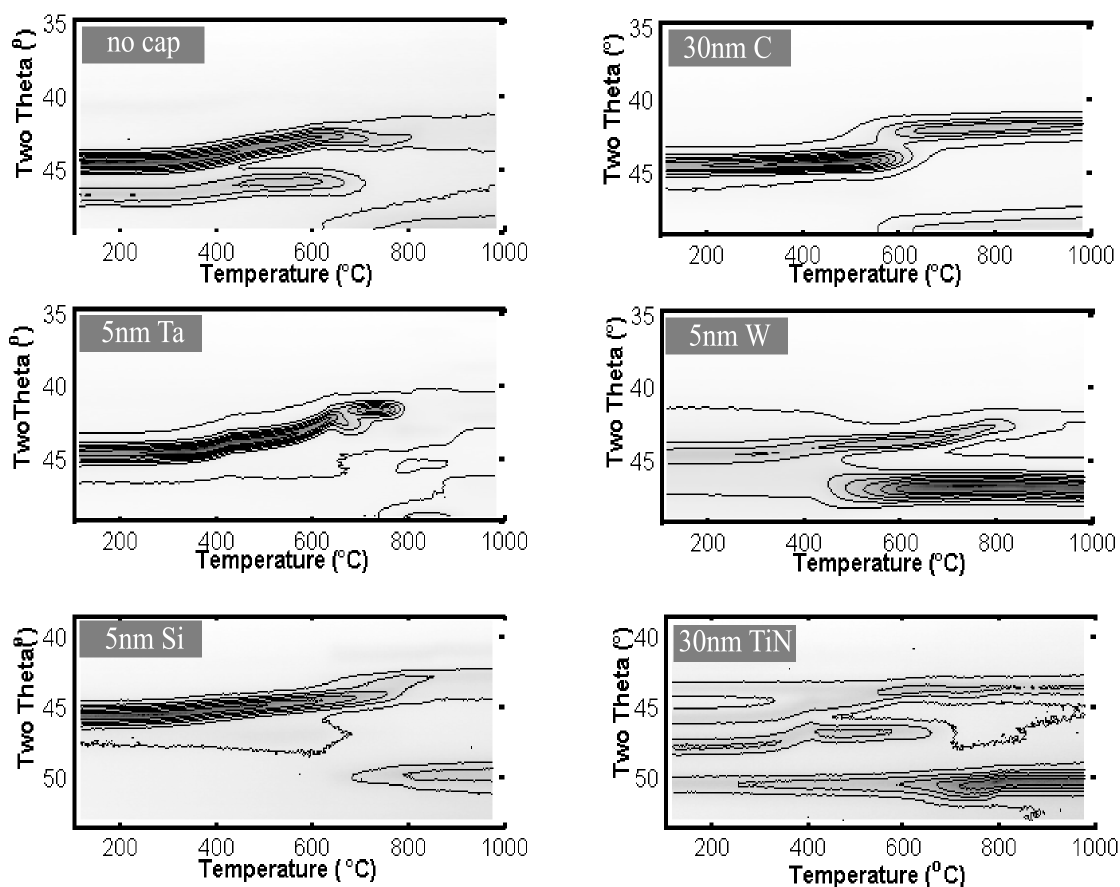

Figure 7.4: *Different capping layers were applied on top of the $Ti/C/SiO_2$ structures. The reaction of the whole system was studied in situ during annealing to $1000°C$.*

Another difficulty poses itself for these structures, namely the possible formation of phases. The formation of other phases, due to the capping layer, might influence the carbide formation, but will also have an effect on the final properties of our produced film. Therefore, the most appropriate capping layer consists of the same material as the base layer, carbon.

In figure 7.5 one can observe the clear phase transition, for the Ti-C system with a 30nm carbon capping layer. The *in situ* XRD measurements were done for 2θ values ranging from $35°$ to $74°$, but only in the windows shown here, there were diffraction peaks observed (two $14°$ windows in 2θ have been combined for this figure).

Between $550°$ and $650°C$ a new phase gets formed, with diffraction peaks $2\theta \approx 42.1°$ and $\approx 49°$. As mentioned before, the shift of the metal peak is only an indication towards the possibility of oxidation. On the other hand, the absence of shift does not

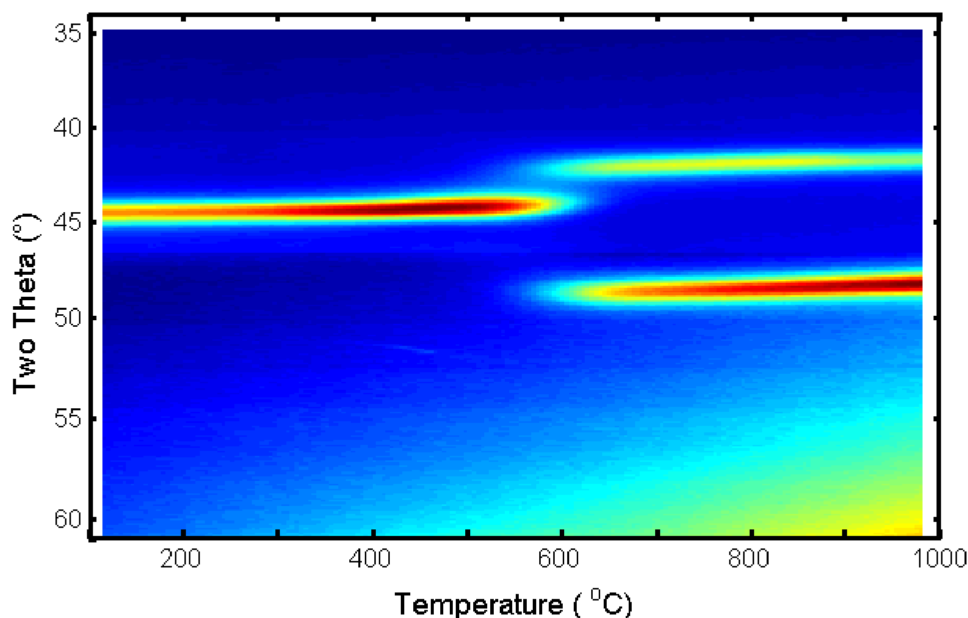

Figure 7.5: *Combined in situ XRD measurements on a Ti-C system, with 30nm C capping layer. The* $Ti(002)$ *peak disappears around* $600°C$ *and the* $TiC(111)$ *and* $TiC(200)$ *appear at* $2\theta \approx 42.2°$ *and* $\approx 49.1°$*, respectively.*

necessarily imply no oxidation. As can be seen from table 7.2, there are also titanium oxides with diffraction peaks around the positions observed in the *in situ* experiment.

Therefore, to confirm carbide or oxide formation, XPS depth profiles were measured on the sample. The depth profiles shown in figure 7.6, evidence the effectiveness of the 30nm C capping layer which was used. There is a clear difference in oxygen concentration in the metal layer. We must remark that even with the capping layer, a certain amount of oxygen can be found in the Ti layer, but this was probably already present in the as-deposited Ti layer (see the RBS measurements of as-deposited Ti-layers in figure 7.3).

More evidence for the carbide formation can be obtained by a careful analysis of the C and Ti binding energies in the XPS spectra. Ramqvist *et al.* [4] studied the charge transfer in transition metal carbides by XPS. They concentrated their work on measurements of the energy shifts of the core electrons in TiC, and in the related materials TiB_2, TiN, TiO, TiO_2, and pure Ti. Examining the $Ti2p$ peak, they observed a shift to a higher binding energy, in TiC compared to pure Ti. Important to mention is that the $Ti2p$ peak also shifts towards a higher binding energy when an oxide is formed, although the amount of energy over which the peak shifts is different. Therefore, from careful examination of the metal peak, one should be able

to evidence the existence of TiC, but it is much more straightforward to look at the $C1s$ peak. They report that the $C1s$ spectra from the transition metal carbides TiC, ZrC, HfC, VC, NbC, TaC, Cr_3C_2, Mo_2C and WC, consist of two lines, instead of one: the hydrocarbon line (i.e. the normal $C1s$ line at $284.6\ eV$), and a second line originating from carbon in the carbide. The latter line was in all cases found at a lower binding energy ($3.3 \pm 0.2\ eV$ lower for TiC) than the hydrocarbon line. This implies that electrons are transferred from the metal to the carbon atoms, when a carbide is formed. Even more, if C-O bonds would exist (C-O compounds are highly volatile, so difficult to observe), the $C1s$ peak would shift to a higher binding energy, thus in the opposite direction of when a carbide is formed.

For our Ti-C system, figure 7.7(a) shows XPS spectra of the $Ti2p$ peak. The solid line spectrum was measured on an annealed, uncapped sample at a certain depth in the Ti layer (to avoid measuring the top oxide layer); the dashed line spectrum was measured on an annealed sample capped with 30nm C. The vertical line in the graph marks the position of the $Ti2p$ peak in pure Ti. Both spectra have shifted towards a higher binding energy, compared to the 'pure' peak. The difference between the two spectra is rather small, with the peak of the uncapped sample at slightly lower binding energy. Comparing our measurement with the one from Ramqvist *et al.* [4], and with the data from the XPS handbook [5], we conclude that the solid line spectrum belongs

Table 7.2: *Overview of the (most intense) diffraction peaks near $2\theta = 42°$ and $= 50°$, for hexagonal Ti, cubic TiC, cubic TiO, orthorhombic TiO_2 ('brooktite'), tetragonal TiO_2, and monoclinic Ti_3O_5, respectively.*

2θ	Ti		TiC		TiO		TiO_2 (b)		TiO_2 (t)		Ti_3O_5	
	°	*hkl*	°	*hkl*	°	*hkl*	°	*hkl*	°	*hkl*	°	*hkl*
42			42.1	(111)			42.4	(102)	42.4	(101)	42.5	(310)
43					43.7	(111)	43.7	(021)				
44												
45	45.1	(002)										
46									46.1	(200)		
47	47.2	(101)					47.1	(202)				
48									48.5	(111)	48.6	(402)
49			49.1	(200)			49.7	(221)				
50					50.9	(200)						

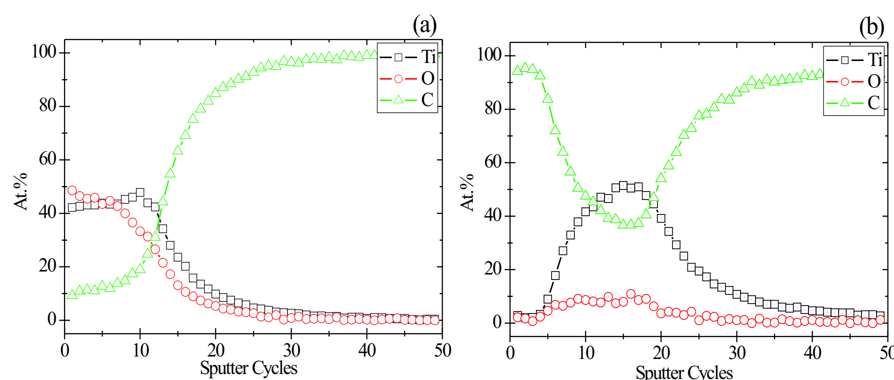

Figure 7.6: *XPS depth profiles, (a) of a Ti-C system without a capping layer, (b) of a Ti-C system with a capping layer. Both samples were annealed to* $1000°C$*. There is a clear difference in oxygen concentration.*

to TiO and the dashed spectrum to TiC. Figure 7.7(c) shows single $C1s$ spectra from the annealed sample with the 30nm capping layer. The solid line spectrum was taken from a region where no Ti was present, so where the carbon peak is at its normal position, and the dashed spectrum from the reaction zone. The 'carbide' peak ($C1s'$) occurred throughout the entire metal layer, and did not shift from its lower binding energy of $282.2\ eV$. Despite the high oxygen level in the uncapped sample, we did observe the $C1s'$ peak throughout most of the metal layer. And although the intensity is smaller than for the capped sample, the position of the peak is the same, as can be seen in figure 7.7(b).

Combining the *in situ* XRD, with the RBS and XPS measurements, we conclude that the Ti-C system without a capping layer mainly forms an oxide, but there is some carbide formation. The 30nm C capping layer prevents the oxidation, so carbide formation can prevail.

Sinclair *et al.* [6] investigated trilayered samples consisting of a Ti layer sandwiched in between two amorphous carbon layers, using Transmission Electron Microscopy (TEM). Their sample setup differs from ours due to the thickness of the metal layer (10 or 20nm, compared to 30nm in this work). They also applied a different annealing regime, using 30 minutes isothermals at increasing temperatures. Upon annealing at $400°C$, TiC formed, and no further changes were detected up to $1000°C$. Miller *et al.* [3] studied 15nm Ti layers on diamond with XPS between room temperature and $700°C$ (the annealing parameters are not clear). Between $150°C$ and $430°C$, their Ti layer consisted of two phases, metallic Ti and $TiC_{0.56}$. At $430°C$ all the metallic Ti is transformed into $TiC_{0.56}$. These examples from literature are consistent with the phase formation we observed, taking the differences in the thickness of the metal layer and annealing conditions into account. In the work of Roth *et al.* [7] we find the interesting observation, that in the Ti-C system, both oxide and

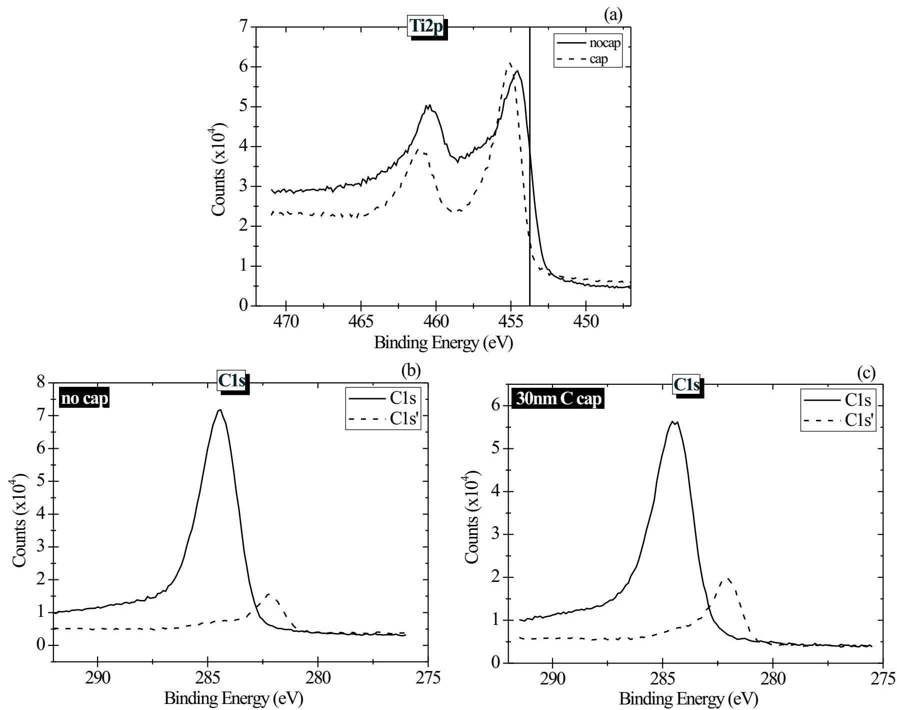

Figure 7.7: *XPS spectra. (a) $Ti2p$ peaks from the uncapped and the capped sample; the vertical line marks the position of the $Ti2p_{3/2}$ peak in pure Ti. (b) and (c) $C1s$ spectra from the uncapped and the capped sample, respectively. $C1s$ is the normal position of the carbon XPS peak, while $C1s'$ is the so-called 'carbide' position.*

carbide phases coexist at lower temperatures. This is probably what happened in our uncapped sample; a coexistence of the oxide and carbide phase, with the oxide phase becoming more prominent upon annealing to higher temperatures. Roth *et al.* found the carbide phase as victor over the oxide, but their annealing was done in high vacuum (better than 3×10^{-9} $mbar$), thus eliminating the oxygen supply from the annealing ambient.

7.2 The Vanadium - Carbon system

VANADIS, the goddess of youth, love, beauty and the dead in the Norse mythology, lends her name to the 23rd element of the periodic table, because this metal has beautiful multicoloured chemical compounds. It was discovered in 1801 by J.M. del Rio in Mexico city, and rediscovered and named in 1830 by a Swedish chemist, N.G. Sefstr$\ddot{o}$m.

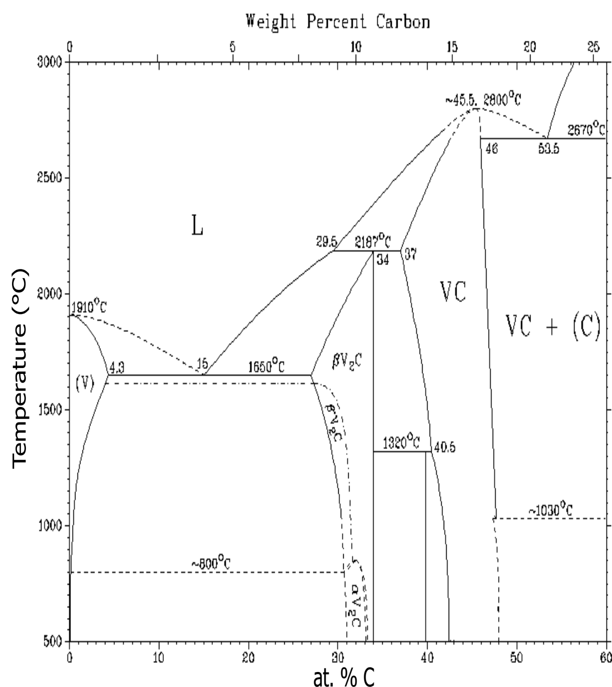

Figure 7.8: *Binary phase diagram for the V-C system [1].*

Table 7.3: *Comparison between some basic properties of the pure metal V, and the carbide phases V_2C and VC.*

	V	V_2C	VC
Crystal Structure	bcc	hcp	fcc
Melting Point $(°C)$	1910	2200	2830
Density (g/cm^3)	6.11	5.67	5.60
Moh's hardness	7	8-9	9-10
Electrical resistivity $(\mu\Omega cm)$	20		60
Thermal conductivity $(W/K\ m)$	31		24.7

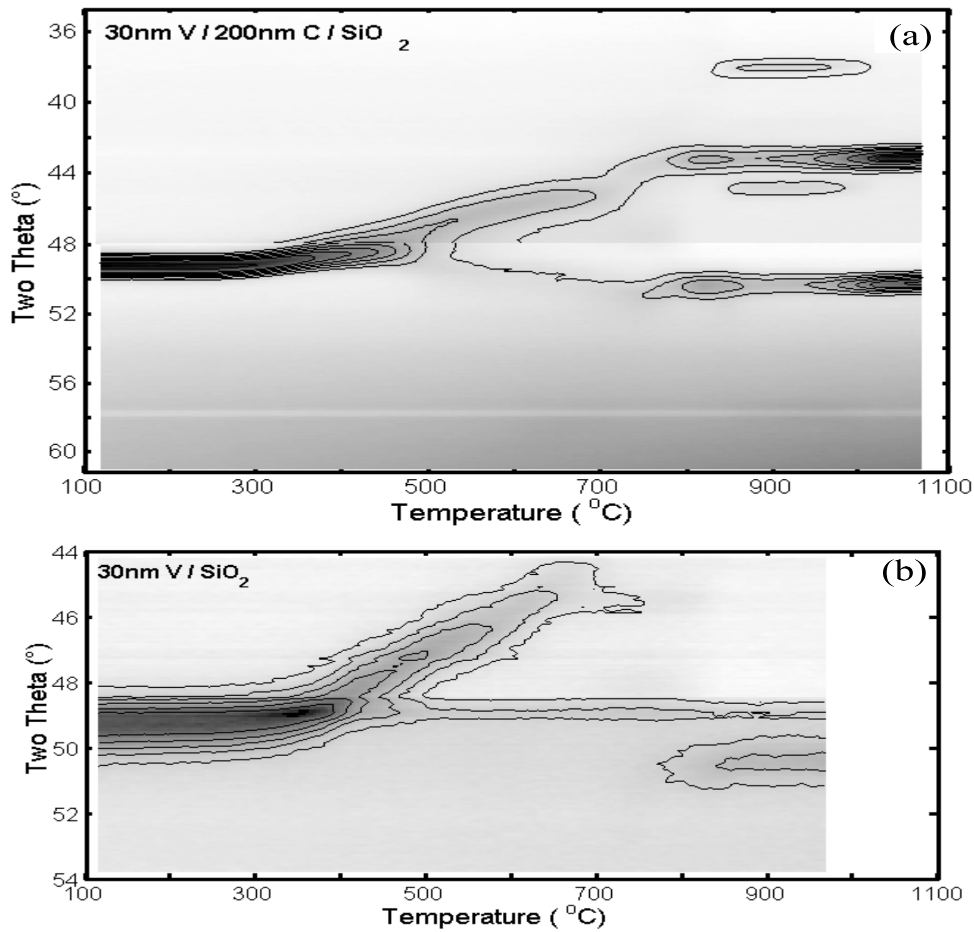

Figure 7.9: *In situ XRD measurements. (a) Two measurements on a V-C system, without a capping layer, annealed to $1100°C$ combined to one figure. (b) Measurement on a 30nm V layer on SiO_2, annealed to $1000°C$.*

Vanadium is most known and used in a compound form, *e.g.* V_2O_5 is a catalyst used in the production of sulphuric acid, and VO_2 is a glass coating to block infrared radiation. Its monocarbide VC is mainly used in cutting tools. Table 7.3 gives a quick comparison between some basic parameters of the metal and the carbides. The binary phase diagram (figure 7.8) shows two stable carbide phases, the vanadium-rich carbide V_2C and the monocarbide VC. The vanadium-rich phase has a rather small composition range ($0.47 \leq x \leq 0.50$), while the range of composition for the monocarbide is $0.74 \leq x \leq 0.92$, with x the carbon-to-metal ratio. The binary phase diagrams give an atomic percentage of carbon, which means that for stoichiometric V_2C the atomic percentage of carbon would be 0.33, and one could write $V_{0.66}C_{0.33}$. Recalculating to the carbon-to-metal ratio, one gets $VC_{0.5}$. In this work, we use the carbon-to-metal notations, as it emphasizes the fact that the vacancies occur at the

Table 7.4: *Overview of the observed XRD peaks in the in situ experiment, and the XRD peaks of the suggested phases for the temperature ranges. The proposed phase sequence can be easily compared with the experimentally observed sequence, as seen in figure 7.9.*

2θ	as dep.	750 $^\circ C$	820 $^\circ C$	1030 $^\circ C$	V		VC		V_2O_3	
					$^\circ$	*hkl*	$^\circ$	*hkl*	$^\circ$	*hkl*
38			■						38.6	(104)
40										
42									42.5	(110)
		■	■	■			43.8	(111)		
44										
			■						45.3	(006)
46										
48									48.5	(113)
	■				49.6	(110)				
50		■	■	■						
							51.1	(200)	51.9	(202)

carbon sites. Actually, the binary phase diagram should also note the V_6C_5, V_4C_{3-x} and V_8C_7 phases. These are carbide phases in which the vacancies are ordered instead of being random (as we generally assume). The order-disorder transition is quite difficult and will not be treated in this work. More information can be found in [8, 9].

Figure 7.9(a) shows *in situ* measurements done on a 30nm V layer, on 200nm C on SiO_2 (two measurements have been pasted together). Figure 7.9(b) shows the annealing of a pure metal layer on SiO_2. Again -as it was for the Ti-C system- we notice a resemblance between the two spectra measured, i.e. the metal peak curls towards lower 2θ values upon heating. We already explained for the Ti-C that this is a first indication towards oxidation. The shift of the metal peak stops around $750°C$, when a new phase seems to form. The 2θ peaks at $\approx 43°$ and $\approx 50.1°$ are at the position where the $VC(111)$ and $VC(200)$ of the cubic monocarbide would be. At $820°C$ another phase is formed, with extra peaks at $2\theta \approx 38°$ and $45°$. As the two possible carbide phases have no peaks there, it is clear that an oxide formed. As can be seen from table 7.4, V_2O_3 has peaks at the observed 2θ values. Around $1030°C$, the extra peaks disappear again, and only the carbide peaks remain. *Ex situ* XRD

measurements on samples quenched at the appropriate temperatures, confirm the occurrence of these phases.

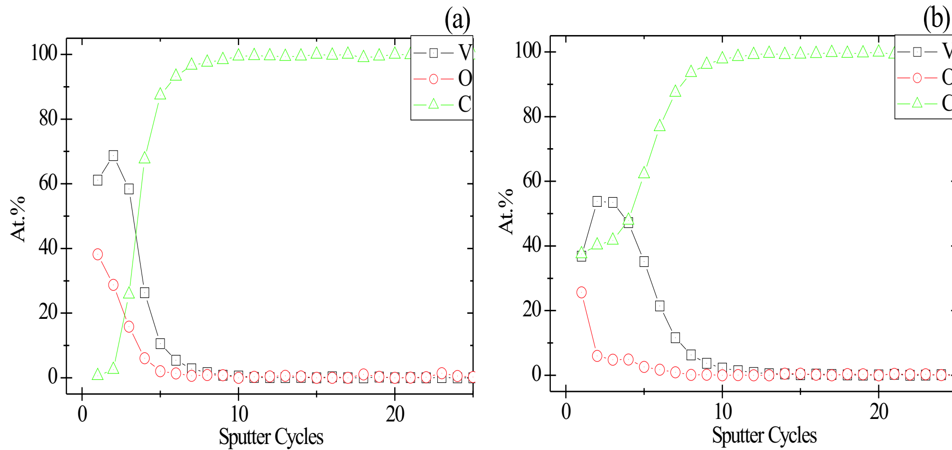

Figure 7.10: *XPS depth profiles on V-C systems without a capping layer, quenched at (a)* $600°C$ *and (b)* $1100°C$.

That the oxygen gets annealed out at higher temperatures, can be seen from figure 7.10, where two XPS depth profiles are shown. The first was done on a sample quenched at $600°C$, the second sample was quenched at $1100°C$. There is a high oxygen concentration in the layer annealed at the lower temperature, but this oxygen concentration has nearly disappeared at higher temperatures. Also, the carbon concentration shows that at these higher temperatures carbon has diffused into the metal layer, and so the carbide formation that was suggested from the XRD measurements is supported by these XPS measurements.

To avoid the oxidation of the V-C sample, we applied a 30nm C capping layer. Figure 7.11 shows the *in situ* XRD experiment for this setup. The shifting of the metal peak at low temperatures has almost entirely disappeared, which provides a first indication that the capping layer is successful at preventing oxidation. Between $680°C$ and $750°C$, we see the formation of the monocarbide phase VC. No other XRD peaks were visible in the other 2θ windows that were measured *in situ*. One immediately notices a vague region, beginning around $550°C$ and preceding the carbide formation. To get an idea of what is happening there, XPS measurements were done on a sample quenched at $600°C$ and one at $1100°C$.

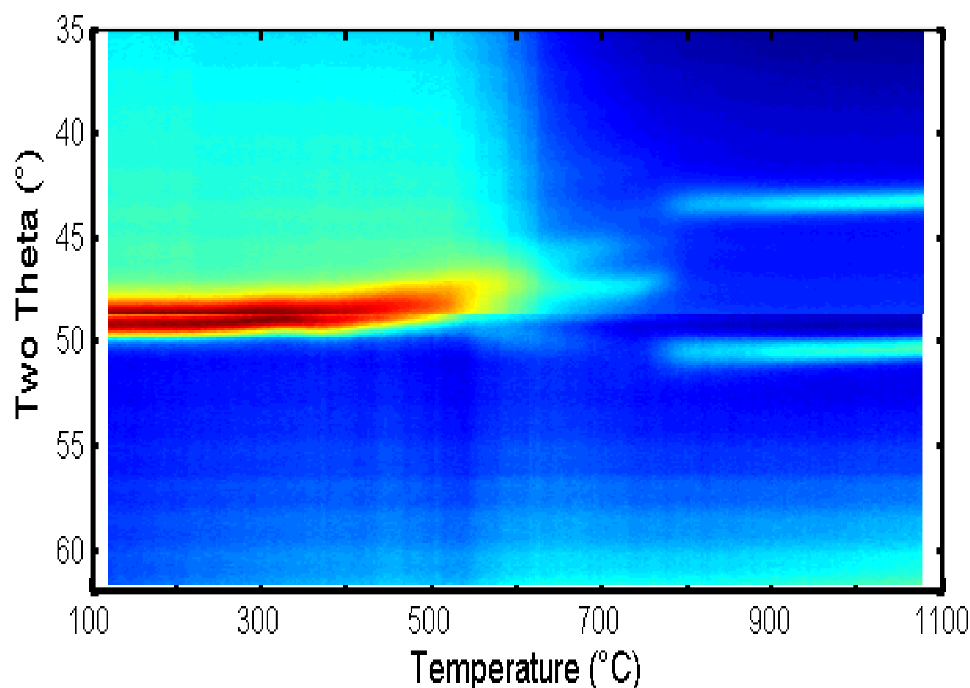

Figure 7.11: *In situ XRD measurements on a V-C system with 30nm C capping layer.*

Comparing figure 7.12(a) and (b), the difference in oxygen concentration is clearly visible. As an extra help, figure 7.12(c) and (d) show the respective single $O1s$ spectra, taken at the depth marked with the dashed line in the depth profiles. Combining these XPS results with additional *ex situ* XRD measurements on quenched samples, we conclude that in the region between $550°C$ and $680°C$, a mixture of the metal-rich carbide V_2C and oxides exists. At higher temperatures, only the monocarbide VC remains. Also, the V_2O_3 phase isn't observed in the region $820°C - 1000°C$

Chen *et al.* [10] produced thin vanadium carbide films on a $V(110)$ surface by exposing the surface to ethylene or 1,3-butadiene, and studied the growth process using Auger Electron Spectroscopy (AES), Electron Energy-Loss Spectroscopy (EELS), and Fluorescence-Yield Near-Edge x-ray absorption Spectroscopy (FYNES). Their data suggest that a significant amount of diffusion occurs at temperatures above approximately $652°C$. This is quite consistent with the formation temperature for VC which was observed in this work.

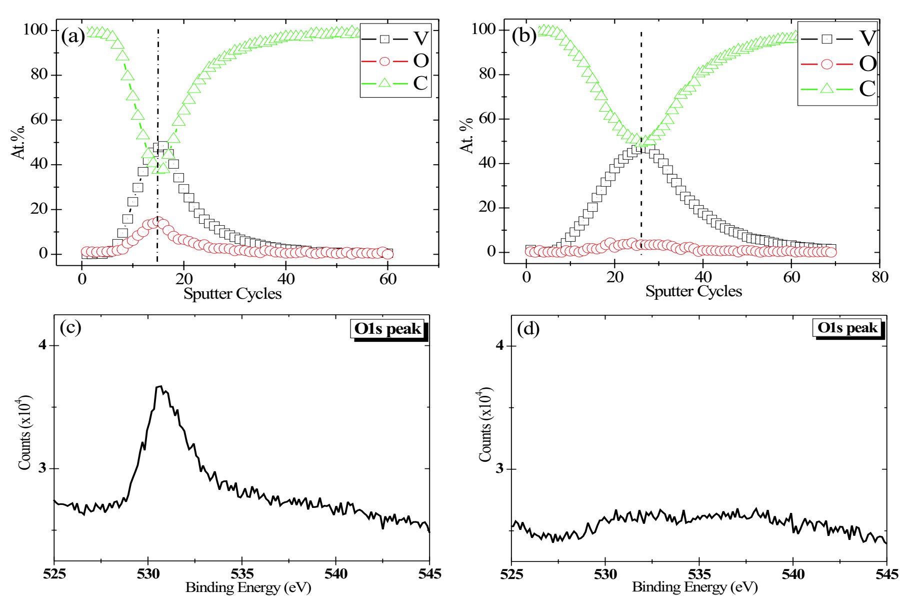

Figure 7.12: *XPS depth profiles measured on V-C samples with 30nm C capping layer, quenched at (a) $600°C$ and (b)$1100°C$. (c) and (d) show single $O1s$ spectra taken at the depths marked with the dashed line in the respective profiles.*

7.3 The Chromium - Carbon system

CHROMA or $\chi\rho\omega\mu\alpha$, the Greek word for colour, can easily be recognized in the name of the 24th element, chromium. In nature, only compounds of this metal occur, and they were already used in the 18th century as pigments in paints, in dyeing and in the tanning of leather. Lead chromate or 'crocoite', for example, gives a bright yellow colour. Although being used before 1797, it was only then that the French pharmacist L.N. Vauquelin succeeded in isolating the metallic chromium. Its most important use nowadays, is in the steel industry where it is a constituent of several alloy steels, *e.g.*, chromium steel or chrome steel. Stainless steel contains from 11% to 18% chromium.

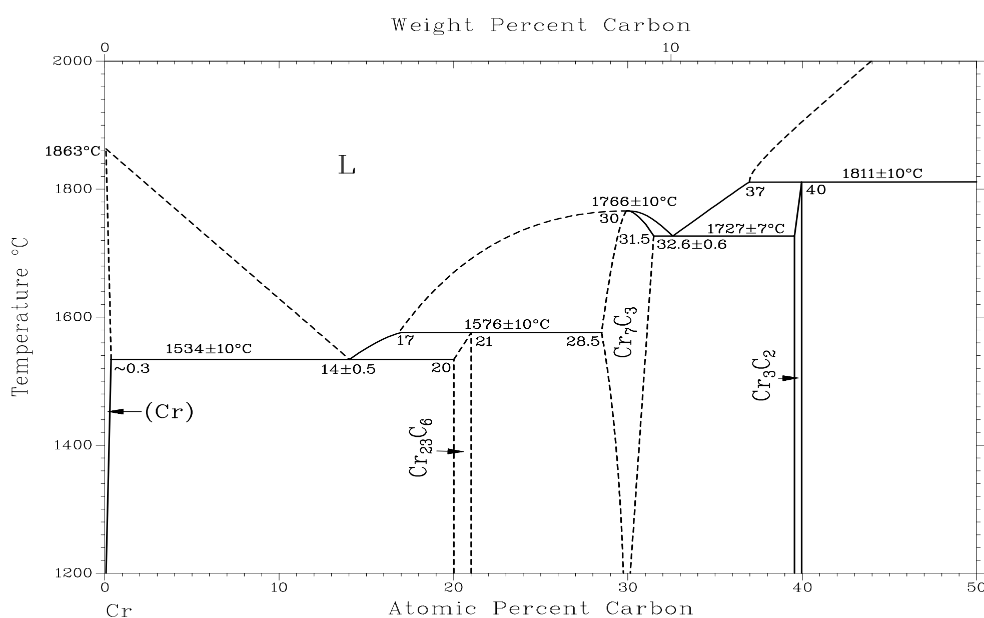

Figure 7.13: *Binary phase diagram for the Cr-C system [1].*

According to the binary phase diagram of Cr and C, as seen in figure 7.13, there are three stable chromium carbides: $Cr_{23}C_6$, Cr_7C_3 and Cr_3C_2. For these three carbide phases and the pure metal, we give some basic properties in table 7.5. All three carbide phases have a very narrow range of composition, being only $0.65 \leq x \leq 0.66$ (with x the carbon-to-metal ratio) for the most important carbide phase Cr_3C_2. From the comparison of the metal with the carbide phases, we see that Cr is a metal with a high melting point, even higher than its carbide phases, which is quite irregular. It also is quite hard, with a Moh's hardness of 8.5 compared to 7 for V, or 6 for Ti. We further mention that the carbide phases have more complex structures than most carbides (which have close-packed structures), in accordance with the Hägg rule, see table 5.3 on page 45.

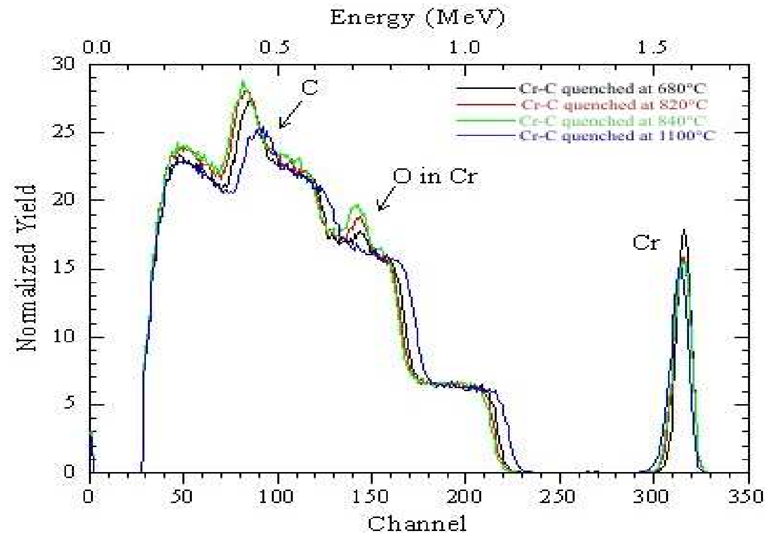

Figure 7.14: *RBS measurements on uncapped Cr-C samples, quenched at $680°C$ (black), $820°C$ (red), $840°C$ (green), and $1100°C$ (blue).*

Figure 7.15 shows the *in situ* experiment on the Cr-C system without a capping layer. Up to $580°C$, the (110) peak of the bcc Cr metal can be observed. There is no significant shift of the peak, unlike what was observed for the uncapped Ti-C and V-C samples. At higher temperatures, three phases can be distinguished. Figure 7.16 shows the *in situ* experiment for the Cr-C system with 30nm C capping layer and one can easily observe that the same three phases are formed. The formation temperatures are slightly different, but this topic will be discussed later, in section 7.8. Additional information is provided by RBS measurements on (uncapped) samples quenched at $680°C$, $820°C$, $840°C$ and $1100°C$, shown in figure 7.14. These measurements show that there is a non-negligible oxygen concentration in all quenched samples except for the sample annealed to the highest temperature of $1100°C$. Ap-

Table 7.5: *Comparison between some basic properties of the pure metal Cr, and the carbide phases $Cr_{23}C_6$, Cr_7C_3 and Cr_3C_2.*

	Cr	$Cr_{23}C_6$	Cr_7C_3	Cr_3C_2
Crystal Structure	bcc	compl.cub.	compl.hex.	orth.rh.
Melting Point $(°C)$	1907	1580	1665	1895
Density (g/cm^3)	7.15	6.97	6.92	6.68
Moh's hardness	8.5	9		
Electrical resistivity $(\mu\Omega cm)$	12.7	127	109	75
Thermal conductivity $(W/K\ m)$	94			189.8

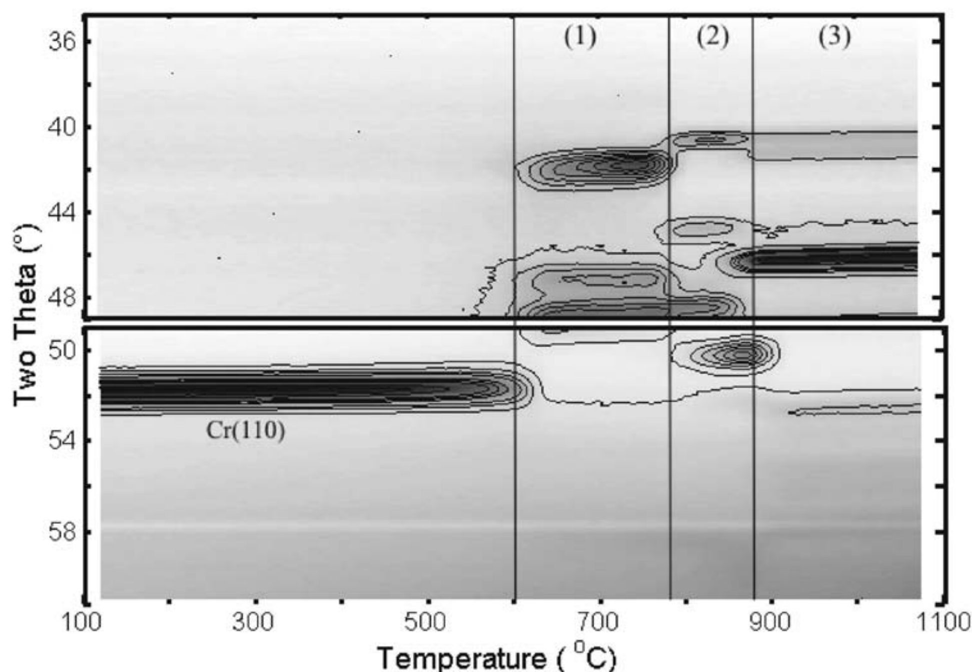

Figure 7.15: *In situ experiment on a Cr-C sample, without capping layer.*

parently the oxygen gets annealed out, something we also observed with the V-C system. To get a better idea of which phases are formed in the three regions, *ex situ* XRD measurements were performed on (capped) samples from the three regions, quenched at $700°C$, $840°C$ and $1100°C$. Combining all the results, we conclude that for the capped Cr-C system, the $Cr(110)$ peak disappears between $580°C$ and $620°C$, and the new phase formed is a mixture of the meta-stable carbide phase Cr_2C and the oxide CrO_2. At about $740°C$ to $770°C$ the next phase occurs, and can be identified as the orthorhombic Cr_3C_{2-x}. Between $900°C$ and $950°C$ the formation of the stable orthorhombic Cr_3C_2 phase (also called 'tongbaite') takes place. An overview of the observed phase peaks and the theoretical peaks for the different phases can be found in table 7.6.

The annealing-out of the oxygen was also observed by Hou *et al.* [11]. They observed a decrease of carbon concentration with an increase of oxygen concentration close to the surface. They argue that the carbon diffuses to the surface, where it is oxidized to CO or CO_2, and then is released into the environment. This method of oxygen reduction is supported by the work of Roth *et al.* [7]. In their study of the chemical interaction of Si, Ti and Mo with graphite surfaces, they found that the release of oxygen from the layer can sometimes only be understood by considering a simultaneous reaction of oxygen with carbon. Most of the oxides are stable up to considerably high temperatures in the absence of carbon. In the presence of an

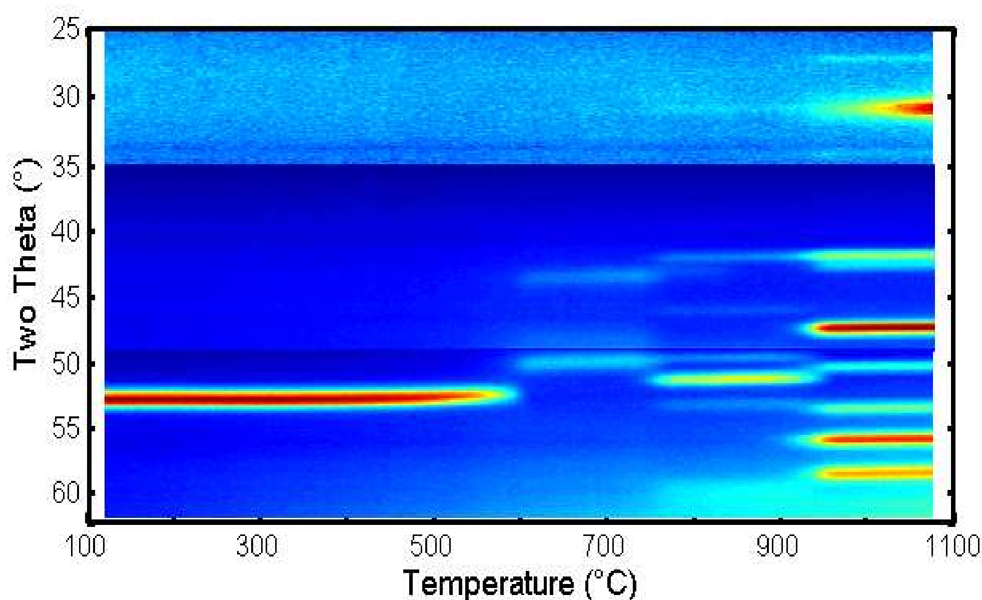

Figure 7.16: *In situ experiment on a Cr-C sample, with 30nm capping layer.*

abundance of carbon, the reaction of oxygen with carbon and subsequent release of the volatile carbon monoxide, appears plausible. We believe a similar mechanism takes place here.

The meta-stable Cr_3C_{2-x} phase, mentioned before, was first discovered by Bouzy *et al.* [12], who observed the formation of it during the crystallisation of C-rich amorphous Cr-C alloys. In an extended version of their experiment [13], an amorphous matrix crystallised into the cubic CrC, followed by crystallisation into the Cr_3C_{2-x} phase, and finally the stable Cr_3C_2 phase. Although the latter two phases were found in our solid-state reaction, the fcc CrC phase has not been observed in our thin film experiments. Sinclair *et al.* [6] used cross-sectional TEM to study a Cr layer, sandwiched between amorphous carbon layers (similar to our sample setup). Upon annealing they observed the formation of the meta-stable hexagonal Cr_2C phase, followed by a second meta-stable phase, orthorhombic Cr_3C_{2-x} and finally the graphitization of amorphous carbon on top of the sample. The Cr_3C_{2-x} formation occurred after annealing the sample at $650°C$ for 20 minutes. Due to the slightly thinner metal layers and the different annealing conditions used by Sinclair *et al.*, it is difficult to relate the formation temperatures to the ones we observed. Also, they didn't observe the formation of the stable Cr_3C_2 phase, but their annealing temperatures didn't go beyond $900°C$. However, Sinclair *et al.* did observe the formation of a graphite layer starting from $750°C$, which they named 'carbide-mediated carbon crystallization'. This graphitization can also be seen in our experiment. In figure 7.16, a broad peak can be observed near $2\theta \approx 31°$ for temperatures above $930°C$. This is not a peak from the Cr_3C_2 phase, but is identified as a graphite peak.

Table 7.6: *Overview of the most intense XRD peaks for the different phases discussed for the Cr-C system. The theoretical most intense peaks are marked with a star. The peaks not visible on the experimental in situ XRD graph, are marked in grey. There is a very good resemblance between this table and the experimental graph.*

T	$100°C$	$600°C$	$755°C$	$925°C$	$1100°C$

2θ	Cr °	Cr hkl	Cr_2C °	Cr_2C hkl	CrO_2 °	CrO_2 hkl	Cr_3C_{2-x} °	Cr_3C_{2-x} hkl	Cr_3C_2 °	Cr_3C_2 hkl
40										
							41.5	(111)	41.4	(104)
42										
									42.4	(202)
			43.9	(100)	43.3	(101)*			43.0	(111)
44										
							45.7	(040)	45.9	(112)*
46										
									46.6	(013)
			47.7	(002)					47.3	(203)
48										
					48.0	(200)	48.3	(041)		
					49.9	(111)	49.5	(112)		
50										
			50.3	(101)*			50.8	(130)	50.2	(105)
							51.4	(023)*		
52										
	52.5	(110)*								
							53.3	(131)	53.7	(204)
54										
									55.0	(211)
56										
									56.1	(006)
									57.6	(212)
58										
									59.3	(301)
60										
							60.1	(132)	60.7	(015)
							61.1	(113)		
62										

T	$100°C$	$600°C$	$755°C$	$925°C$	$1100°C$

7.4 The Manganese - Carbon system

GROUP VIIb in the periodic table is led by element number 25, Manganese (Mn). This metal resembles iron, but it is harder and more brittle. Manganese exhibits

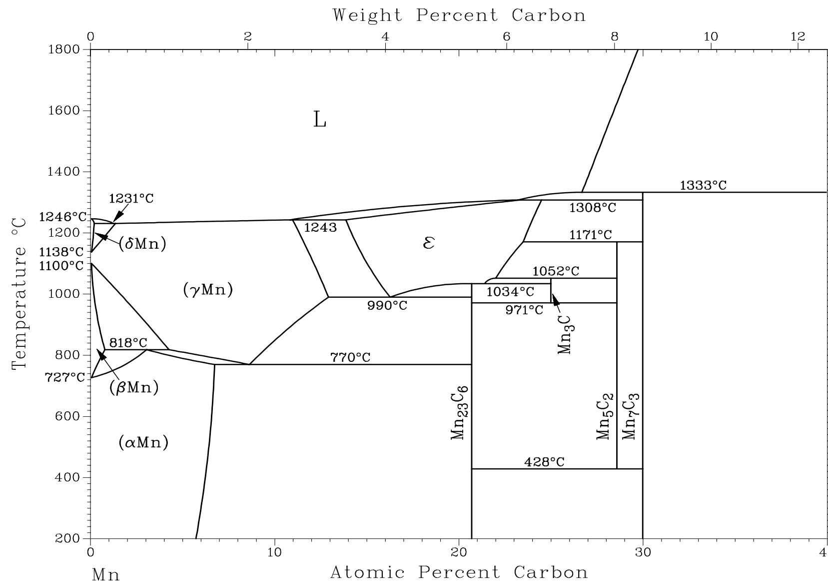

Figure 7.17: *Binary phase diagram for the Mn-C system [1].*

allotropy and has four(!) different forms, as can be seen in the binary phase diagram in figure 7.17. The name of this element is derived from the Latin word '*magnes*', meaning magnet. Compounds of manganese were already used 17 000 years ago, as paints were pigmented with manganese dioxide (black colour). Further it has been used in glass-making, steel-making and (more recently) in batteries. The Swedish chemist C.W. Scheele was the first to recognize that manganese was an element,

Table 7.7: *Some basic properties of the pure metal Mn and the carbide phases $Mn_{23}C_6$, Mn_3C, Mn_5C_2, and Mn_7C_3.*

	Mn	$Mn_{23}C_6$	Mn_3C	Mn_5C_2	Mn_7C_3
Crystal Structure	bcc	compl.cub.	orth.r.	monocl.	compl.hex.
Melting Point $(°C)$	1246	1010	1520		1340
Density (g/cm^3)	7.21	7.5	6.9		7.4
Moh's hardness	6				
Electrical resistivity $(\mu\Omega cm)$	160				
Thermal conductivity $(W/K\ m)$	7.8				

and his colleague, J.G. Gahn, isolated the pure element in 1774. As seen in figure 7.17, Mn can form several carbide phases, $Mn_{23}C_6$, Mn_3C, Mn_5C_2, and Mn_7C_3. All these carbide phases have a very narrow range of composition. Table 7.7 lists some properties of the metal and of the carbide phases. The carbide phases all have a relatively complex crystal structure, as was predicted by Hägg's law (see Chapter 5, section 5.2 on page 42).

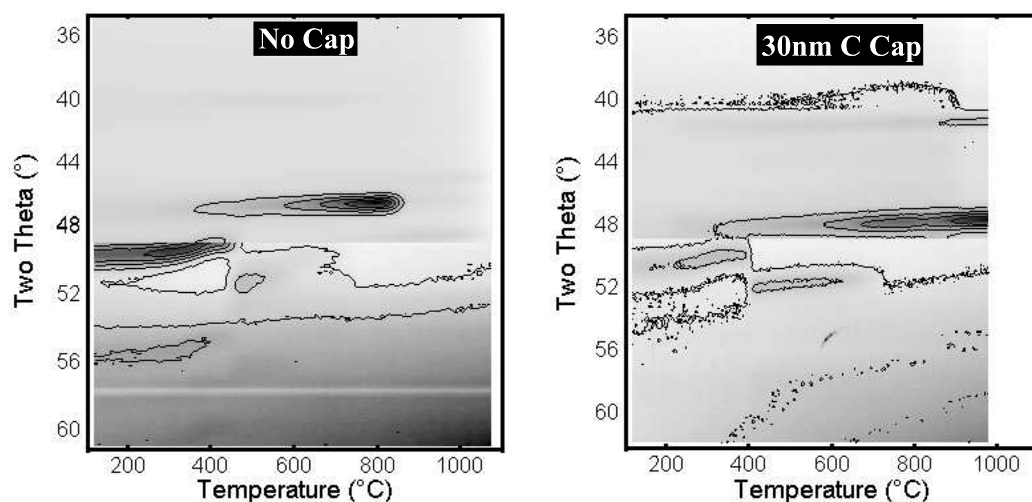

Figure 7.18: *in situ XRD measurements performed on a Mn-C samples, without a capping layer (left), and with 30nm C capping layer (right). Two 2θ windows have been combined for each figure. No carbide formation is observed.*

The *in situ* XRD measurements for the Mn-C system are shown in figure 7.18. Both without and with a 30nm C capping layer, the Mn metal peak makes a shift towards lower 2θ values, around $300°C$. After that, the Mn peak disappears, indicating the formation of a carbide or oxide phase. RBS measurements on the uncapped sample, suggest the formation of Mn_2O_3. For the capped sample a MnO composition is proposed from *ex situ* XRD, for which the peaks at $2\theta \approx 41°$ and $47.7°$ are visible in the *in situ* measurement, from $300°C$ to the end of the experiment. It is possible that an additional phase exists between $400°C$ to $700°C$. But as the MnO peaks remain to the end, oxidation prevails and no more time was dedicated in examining the exact phases. Unfortunately for this system, no final carbide formation was obtained and a possible explanation will be given later in this chapter.

7.5 The Iron - Carbon system

ATOMIC number 26 is given to the most abundant heavy metal in the universe (and on earth), iron. It has an entire 'age' named after it, and the first signs of usage come from the Sumerians and the Egyptians, who used iron from meteorites to make some items like daggers and ornaments. The word 'iron' probably comes from the

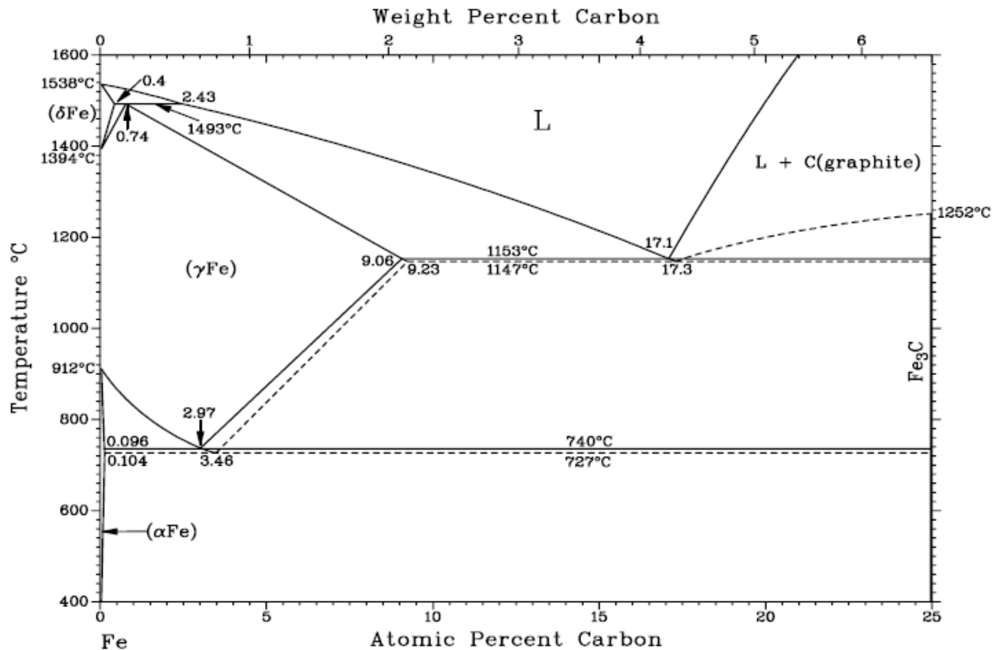

Figure 7.19: *Binary phase diagram for the Fe-C system [1].*

Etruscan word *aisar*, 'the gods', which refers to the meteorites that fell from the sky. Iron (Fe) is the most used metal of all, due to its low cost and high strength. The word 'iron' immediately makes one think of 'steel', the best known alloy of iron, but there are also other forms which iron can take (like Pig Iron, Cast Iron, Wrought Iron, etc). Figure 7.19 shows the binary phase diagram for the Fe-C system, where one can see the metastable Fe_3C phase, called 'cementite'. Cementite is sometimes called cohenite, especially when found mixed with nickel or cobalt compounds. In addition to cementite, numerous Fe-C compounds have been reported (FeC, Fe_2C, Fe_4C, Fe_7C_3,...), but the lack of additional evidence explains their absence in the phase diagram.

Table 7.8 gives some properties of the pure metal and the carbide phase. Properties for the cementite phase are hard to find, as it is most commonly found as facets inside white cast iron, and not so much as an alloy on its own.

Table 7.8: *Some basic properties of the pure metal Fe and the carbide phase Fe_3C.*

	Fe	Fe_3C
Crystal Structure	bcc	orth.rh.
Melting Point $(°C)$	1538	1650
Density (g/cm^3)	7.9	7.2
Moh's hardness	4	
Electrical resistivity $(\mu\Omega cm)$	10.1	
Thermal conductivity $(W/K\ m)$	80.4	

In figure 7.20, one can compare the *in situ* XRD measurements on Fe-C samples, without and with a 30nm C capping layer. The diffraction peaks observed are similar, so we conclude that the same phases are formed with or without a C capping layer. Between $510°C$ and $550°C$ (for the capped samples), the Fe_3C phase gets formed. Table 7.9 lists the diffraction peaks for this carbide phase.

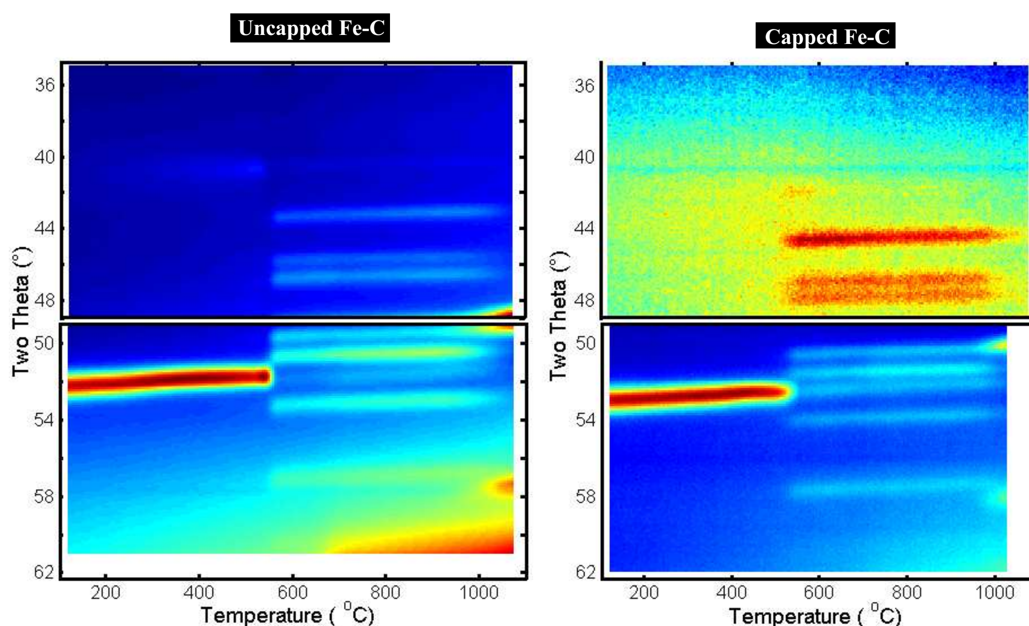

Figure 7.20: *In situ XRD measurements on Fe-C samples, without a capping layer (left) and with 30nm C capping layer (right). The two measurements show the same diffraction peaks. For the capped sample, the 2θ window from $\approx 35°$ to $\approx 49°$, shows quite a high background, which explains the yellow colour (higher intensity).*

Table 7.9: *The most important diffraction peaks of the carbide phase Fe_3C, in the 2θ window $\approx 35^\circ$ to $\approx 61^\circ$.*

2θ	hkl	2θ	hkl
44.2	(121)	52.5	(220)
44.3	(210)	53.0	(031)*
46.8	(002)	54.0	(112)
47.8	(201)	57.4	(131)
50.5	(211)	58.0	(221)
51.5	(102)	61.3	(122)

A special feature can be observed around $630^\circ C$ at $2\theta \approx 29^\circ$ and $\approx 61^\circ$, namely the formation of a graphite layer on top of the carbide layer. These peaks are shown in figure 7.21 and can be identified as the (002) and (004) peak, respectively. RBS measurements confirmed that there is a carbon layer on top of the carbide, and it should be stressed that this segregation occurs, even for samples without an as-deposited C capping layer.

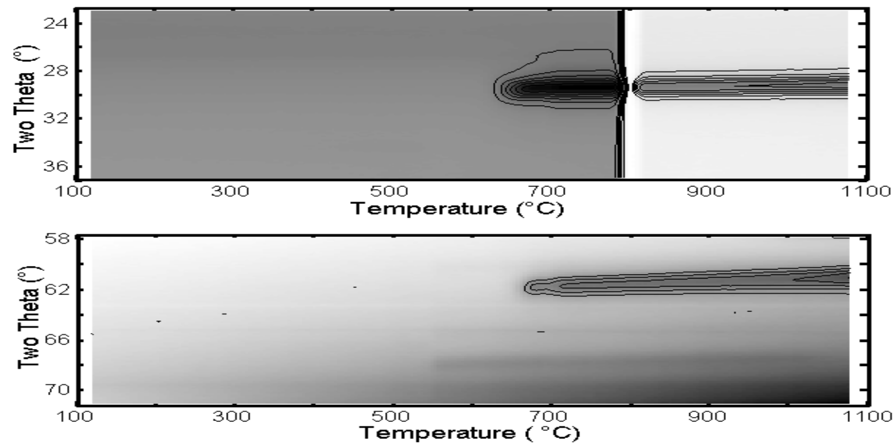

Figure 7.21: *Two 2θ windows of in situ XRD measurements performed on Fe-C samples. A graphite layer segregates on top of the carbide layer. The measurements shown here have been done on samples without a carbon capping layer, to accentuate the graphite segregation.*

At high temperature, the start of another phase can be seen, just within the limits of our measurement. The 2θ peaks around 49.5° and 57.7° can be related to the (111) and (200) of austenite (or $\gamma - Fe$), respectively. However, additional *ex situ* XRD measurements on samples annealed to this last phase, always showed an extra diffraction peak which could not be accounted for by austenite. Figure 7.22 shows the

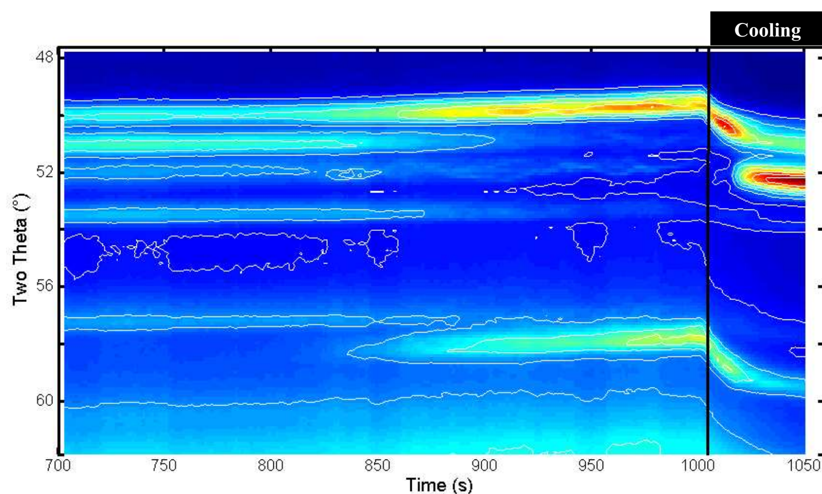

Figure 7.22: *Last part of an in situ XRD measurement on a Fe-C system, annealed at $1°C/s$. The x-scale is the elapsed time in the experiment (not the temperature, as in the other experiments). The full line marks the point where the heating stopped, and the sample got quenched.*

last part of an *in situ* XRD measurement on a Fe-C system. The sample was annealed at $1°C/s$, and the x-scale shows the elapsed time, instead of the temperature. The full line in the figure shows where the heating stopped, and the quenching of the sample started. Up to $850s$, the diffraction peaks of cementite are visible, and upon further heating, these peaks transform in the austenite phase. Once the cooling kicks in, the two austenite peaks shift to higher 2θ values, which is a consequence of the thermal shrinking of the lattice (smaller d-spacing, thus higher 2θ values). However, the most striking observation is at $2\theta \approx 52°$, where the $\alpha - Fe(110)$ pops back up. This is the extra diffraction peak which was observed in the *ex situ* experiment, as shown in figure 7.23. The graphite (002) peak can be clearly seen at $2\theta(CuK\alpha) \approx 26.2°$, and the $\alpha - Fe(110)$ and (002) peaks are also observed. Another small peak is visible (look at the enlargement) at $2\theta \approx 43.7°$, which we identified as carbon-iron $Fe_{1.88}C_{0.12}(101)$.

As a conclusion for the Fe-C system we summarize that for the capped sample, (meta-stable) cementite Fe_3C gets formed between $510°C$ and $550°C$. Around $630°C$, a graphite layer segregates on top of the cementite layer, which finally forces the cementite layer to transform in fcc $\gamma - Fe$ ('austenite'). When cooling down, most of the austenite transforms back into normal bcc iron, $\alpha - Fe$, but some Fe is left with a high carbon content.

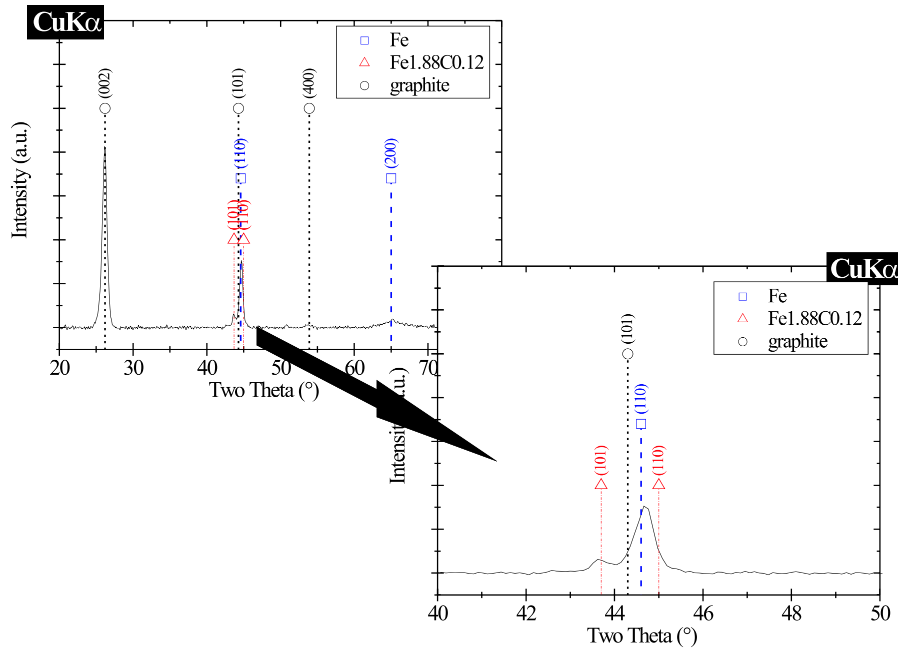

Figure 7.23: *Ex situ XRD measurement ($CuK\alpha$) of a Fe-C sample with carbon capping layer, after annealing it to $1100°C$. The 2θ range between $40°$ and $50°$ has been enlarged to get a better view.*

Sinclair *et al.* [6] studied thin (10nm or 20nm) Fe layers between amorphous carbon layers using cross-sectional TEM. After annealing at $500°C$ for 20 minutes, the metal layer had entirely transformed into the metastable carbide, cementite. Like in the Cr-C system, they also saw a carbide-mediated graphitization, this time after annealing at $600°C$. Santaniello *et al.* [14] irradiated 100nm Fe-layers on high-purity pyrolitic graphite with D^+ beams at temperatures ranging from room temperature to $900K$, and studied the layers with Mössbauer spectroscopy. Their results suggest a complete transformation of Fe into the carbide at $700K$ ($427°C$). The carbide formation appears to be a precursor of the segregation of C atoms at the surface of the sample for temperatures above $800K$.

7.6 The Zirconium - Carbon system

ZIRCONIUM is a fairly abundant element and it is widely found in minerals, mostly as the mineral 'zircon' ($ZrSiO_4$). Zirconium is the 40th element in the periodic table, is lighter than steel and has the same hardness as copper. An exciting characteristic is its spontaneous ignition in air (especially at high temperatures), when it is finely divided. The element was discovered in 1789 by M.H. Klaproth, but it took until 1914 to get the pure metal.

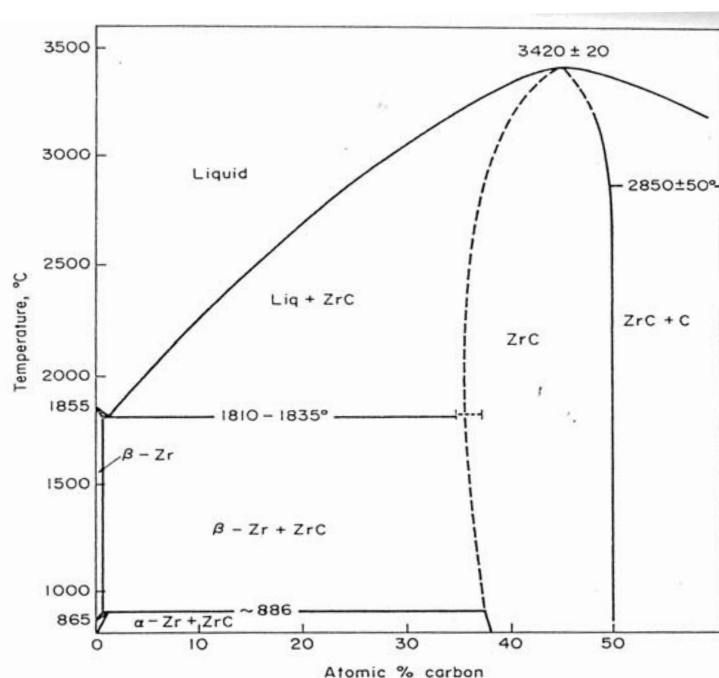

Figure 7.24: *Binary phase diagram for the Zr-C system, reproduction from L.E. Toth [2].*

Looking at the binary phase diagram for the Zr-C system in figure 7.24, one can observe only one carbide phase, namely the monocarbide ZrC. This carbide phase has a relatively large range of composition, $0.61 \leq x \leq 1$, with x the carbon-to-metal ratio. Some properties of the pure metal and the monocarbide have been summarized in table 7.10.

From the table, one can learn that the Zr metal is quite soft, and the carbide has a higher strength and melting point, while other properties like the thermal conductivity and electrical resistivity, are in the same range. These properties make the carbide a good candidate to be used in engineering ceramics, but applications are still quite rare (mostly in prototypes).

Table 7.10: *Some basic properties of the pure metal Zr and the monocarbide phase ZrC.*

	Zr	ZrC
Crystal Structure	hex.	fcc
Melting Point $(°C)$	1855	3550
Density (g/cm^3)	6.52	6.73
Moh's hardness	5	8-9
Electrical resistivity $(\mu\Omega cm)$	42	63
Thermal conductivity $(W/K\ m)$	22.6	21

Figure 7.25 shows the *in situ* XRD measurement on a Zr-C system without a capping layer. The peaks at the start of the experiment, are (from top to bottom) the (100), (002), and (101) of the hex. Zr metal. The diffraction peaks observed at the end of the experiment, do not correspond to any known peaks of a carbide. Therefore, oxidation is most probable. RBS measurements on this sample confirm the high oxygen concentration and hint that the film has transformed into ZrO_2. The diffraction peaks of this oxide correspond to the ones observed in the *in situ* experiment, i.e. a (111) and (002) peak at $2\theta \approx 36.9°$ and $\approx 39.8°$, respectively, and a few peaks between $2\theta \approx 40° - 42°$.

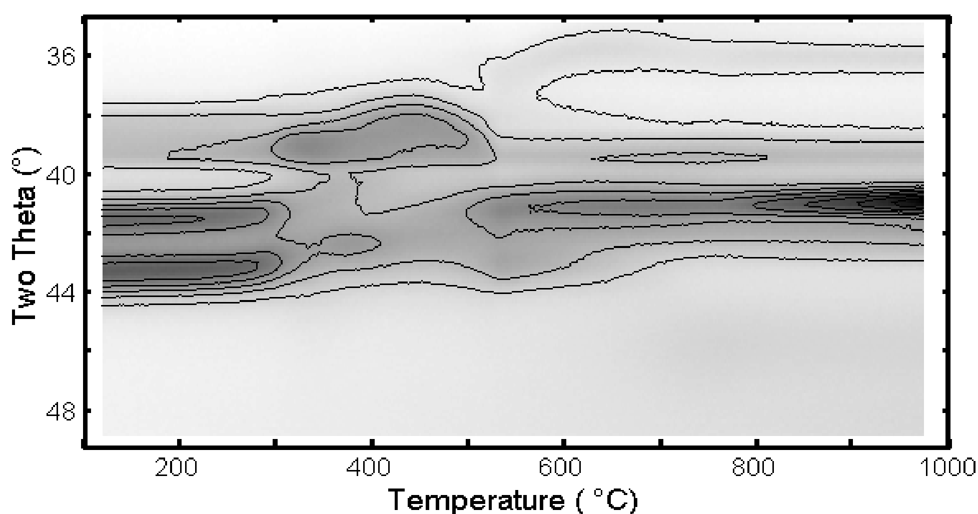

Figure 7.25: *in situ XRD measurements on an uncapped Zr-C sample.*

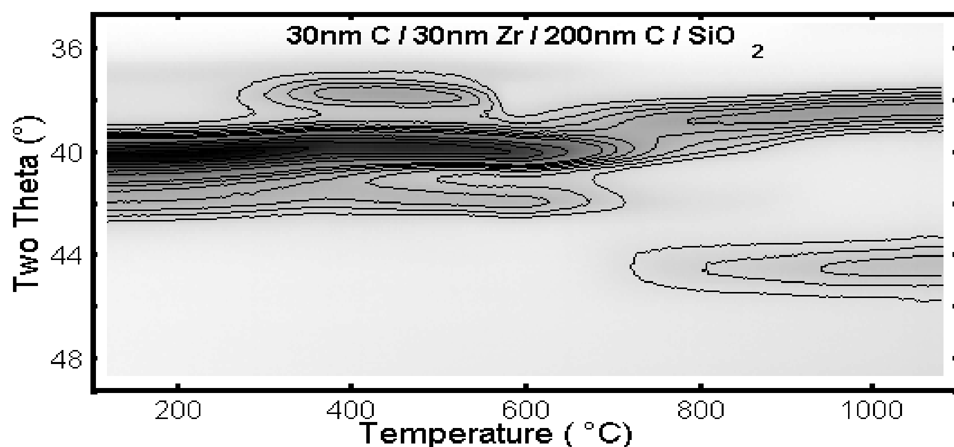

Figure 7.26: *in situ XRD measurements on a Zr-C sample with 30nm C capping layer.*

To avoid oxide formation, a capping layer of 30nm C was applied and the experiment was redone. Figure 7.26 shows the *in situ* XRD measurement on capped Zr-C samples. The XRD data for the capped sample is clearly different than that of the uncapped sample. Around $300°C$ a new phase seems to form, which in turn transforms to a next phase with peaks around $2\theta \approx 38.5°$ and $\approx 44.3°$. Around those 2θ values, both ZrO and ZrC have their (111) and (200) diffraction peaks. As a first step we tried to identify the phase that forms at lower temperatures. However, both Zr and Zr_3O have diffraction peaks at about the same positions (the ones observed in the experiment). The most probable explanations for the extra peak appearing at $2\theta \approx 37.5°$ is the formation of Zr_3O (presuming the experiment started with a Zr

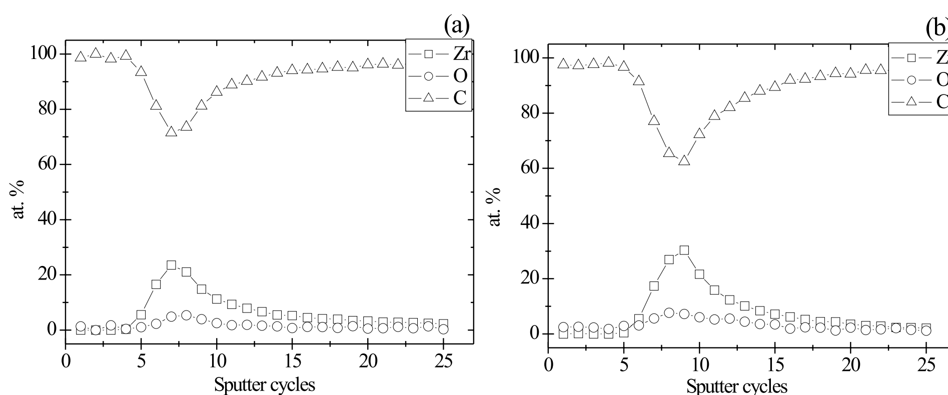

Figure 7.27: *XPS depth profile of a Zr-C sample with 30nm C capping layer, as deposited (a) and annealed to $450°C$ (b).*

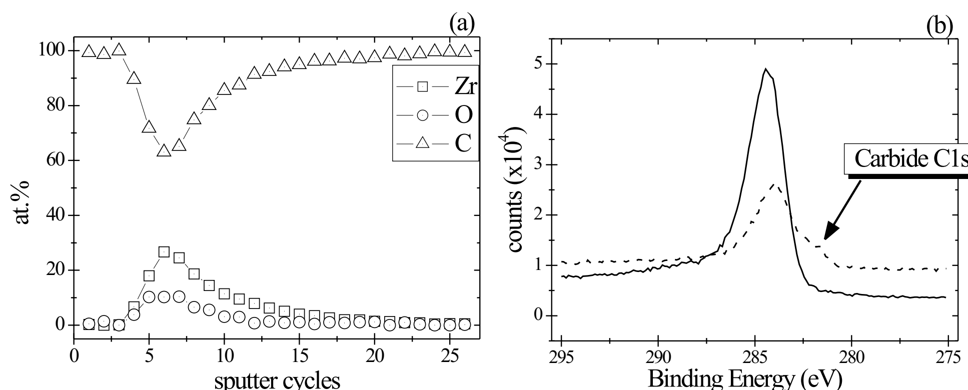

Figure 7.28: *(a) XPS depth profile of a Zr-C sample with 30nm C capping layer, annealed to $1000°C$. (b) Two single $C1s$ spectra taken from either the region where no Zr metal was present (full line), or from the reactive zone (dashed line). There is sign of some carbide formation, which is marked with the arrow.*

metal layer). Other explanations could be the appearing of the diffraction peak of the (100) plane of Zr (presuming the experiment started with a Zr metal layer), or the appearing of the diffraction peak of the (110) plane of Zr_3O (presuming the experiment started with a Zr_3O layer). Figure 7.27 shows additional XPS measurements on an as deposited sample and a sample quenched at $450°C$. There was no difference observed between the two depth profiles, nor bteween the single element spectra. They both have a certain oxygen content, so no undivided conclusion can be drawn. The first explanation seems the most plausible.

To find out which phase is formed at higher temperatures, an XPS measurement was done on a sample quenched at $1000°C$, as shown in figure 7.28(a). One can observe a high oxygen concentration in the layer, so the formation of ZrO is most probable. Inspecting the XPS $C1s$ spectra, a very small shift towards the 'carbide' position was observed, as can be seen in figure 7.28(b), where the shoulder has been marked. We therefore conclude that a small amount of carbide has formed, but that oxidation of Zr was predominant, in spite of the presence of a capping layer.

7.7 The Niobium - Carbon system

COLUMBIUM was the name originally given to the 41st element, which was discovered by C. Hatchett in 1801 in some columbine ore, sent to him from Connecticut.

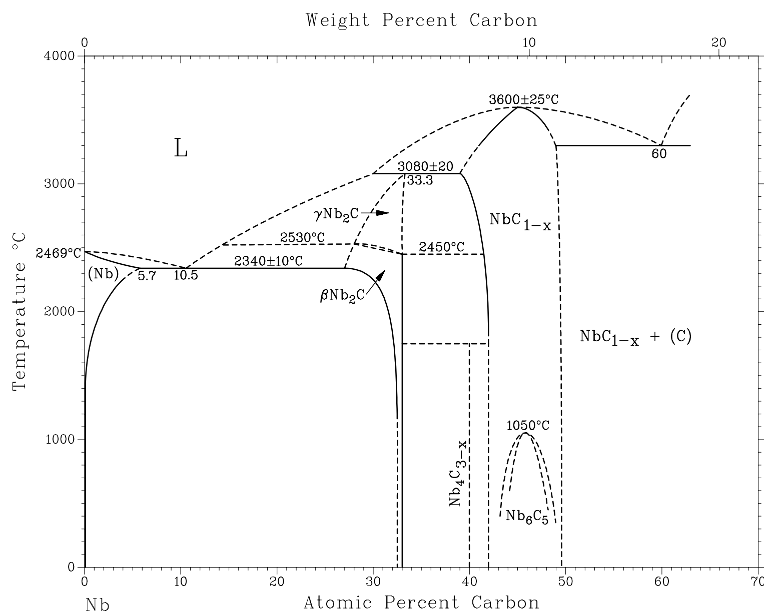

Figure 7.29: *Binary phase diagram for the Nb-C system [1].*

In 1846, H. Rose rediscovered the element and named it after Niobe, the daughter of a son of Zeus, Tantalus. After 100 years of controversy, the IUPAC (International Union of Pure and Applied Chemistry) officially adopted 'niobium' as the name for this element. Niobium is widely distributed in nature, occurring about one and a half times

Table 7.11: *Some basic properties of the pure metal Nb and the carbide phases Nb_2C and NbC.*

	Nb	Nb_2C	NbC
Crystal Structure	bcc	hcp	fcc
Melting Point $(°C)$	2477	3100	3480
Density (g/cm^3)	8.6	7.8	7.8
Moh's hardness	6		8-9
Electrical resistivity $(\mu\Omega cm)$	15.2	60	35
Thermal conductivity $(W/K\ m)$	53.7		30

as abundant as lead, and it is found in minerals such as columbite and tantalite.

From the binary phase diagram shown in figure 7.29, one can learn that there exist two stable carbide phases. The metal rich carbide Nb_2C has a narrow range of composition $0.48 \leq x \leq 0.49$, with x the carbon-to-metal ratio. The monocarbide NbC, however, can exist over a wide range of composition $0.72 \leq x \leq 0.98$. For certain compositions within this range, ordered structures of the carbon-vacancies have been reported. However, in our work the entire range will be labelled as NbC_x. Table 7.11 gives the basic properties for the metal and its carbides.

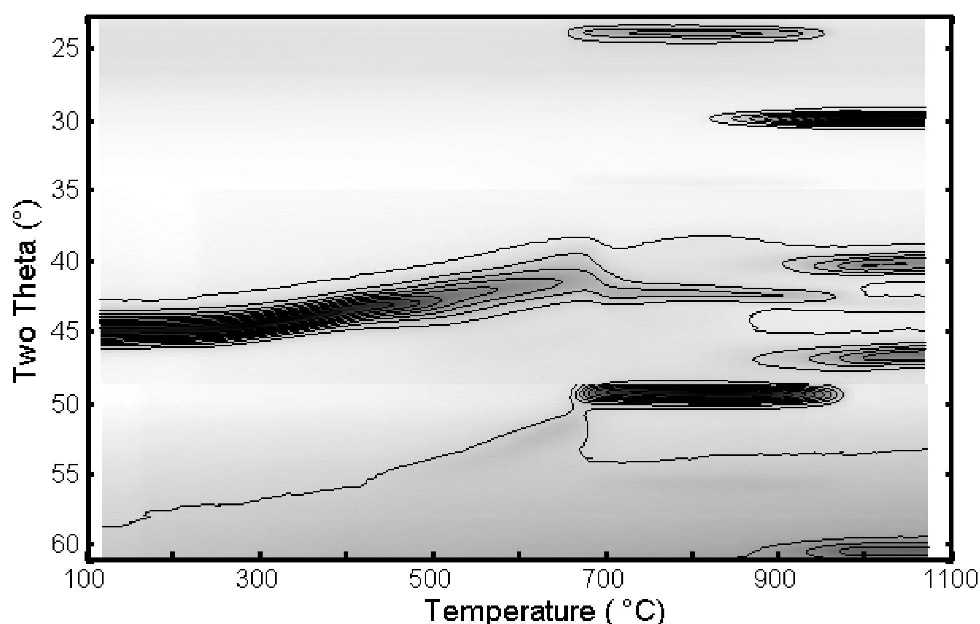

Figure 7.30: *in situ XRD measurements performed on a Nb-C sample, without a capping layer.*

Like the other systems, Nb-C samples were examined using *in situ* XRD and figure 7.30 shows the measurement for an uncapped sample. The metal peak of Nb is clearly seen at the start of the experiment. However, upon annealing, the peak shifts towards lower 2θ-values, which hints towards oxidation. RBS measurements confirmed the oxidation of Nb. The *in situ* XRD peaks $2\theta \approx 24.3°$, $\approx 42.8°$, and $\approx 49.9°$ are identified as the (100), (111) and (200) peaks of NbO, respectively. Around $700°C$ the formation of this oxide can be observed, followed by the formation of NbO_2 around $900°C$. The peaks observed, from top to bottom, are (220) at $2\theta \approx 29.9°$, (202) at $\approx 40.7°$, (400) at $\approx 42.8°$, (222) at $\approx 46.2°$ and (422) at $\approx 60.6°$.

A capping layer of 30nm C was applied to the Nb-C samples, and this resulted in different results for the *in situ* experiments. Figure 7.31 shows the combination of two different 2θ windows into one figure. The discontinuity in the background near $49°$ is

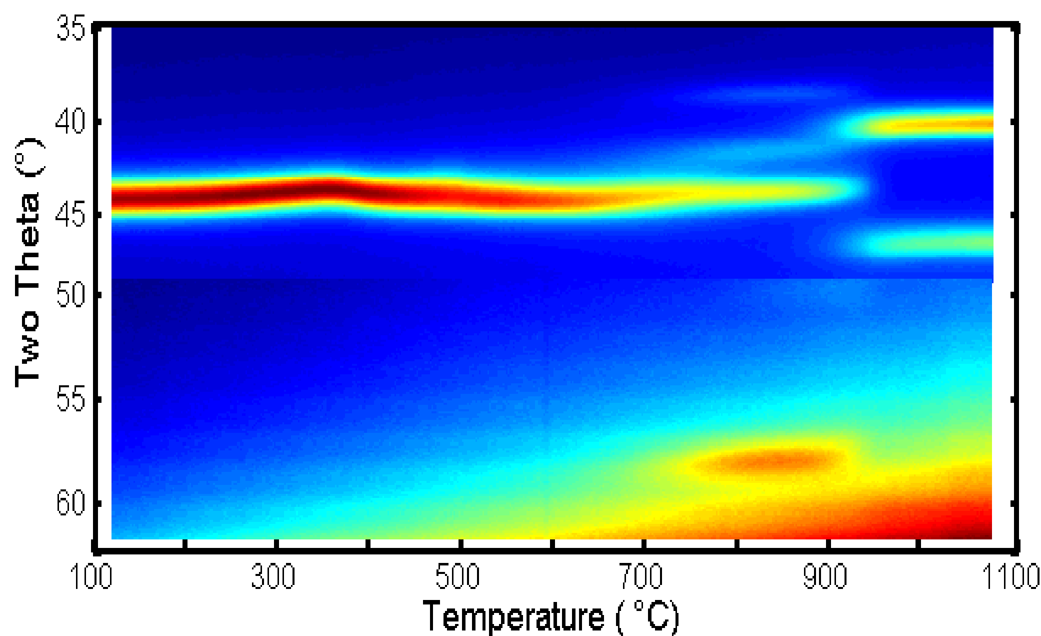

Figure 7.31: *in situ XRD measurements performed on a Nb-C sample, with 30nm C capping layer. Two 2θ windows have been combined into one figure. Due to the difference in backgrounds, the stitching isn't perfect, as can be seen around $2\theta \approx 49°$.*

caused by the pasting of two different measurements. In the *in situ* measurement, one can observe the formation of the hexagonal Nb_2C phase from $690°C$, with its (100), (002), (101) and (102) peaks at $2\theta \approx 38.8°$, $\approx 42.4°$, $\approx 44.4°$ and $\approx 58.9°$, respectively. For completeness, we must mention that the Nb_2C phase can also be orthorhombic, which has about the same XRD pattern. This transition to the metal-rich carbide has not so definite boundaries as the next transition to the face-centred cubic (fcc) monocarbide, NbC. From $880°C$ to $940°C$, one observes the appearance of the (111) and (200) peaks of the NbC phase, at $2\theta \approx 40.7°$ and $\approx 47.4°$.

Extra evidence is given by XPS measurements performed on an uncapped and a capped sample, both quenched at $1050°C$. Comparing the oxygen concentrations in figure 7.32(a) and (b) and combining these results with the XRD measurements, one can easily see that the Nb-C system has formed an oxide when the system had no capping layer. Figure 7.32(c) and (d) show single $C1s$ spectra taken at different depths from an uncapped and a capped sample, respectively. The spectra from the capped sample show, as was expected, the $C1s'$ peak at the 'carbide' position, throughout the carbide layer. There is also a $C1s$ peak shown taken at a depth, where no metal nor reaction has taken place, as a reference to the normal $C1s$ position. Figure 7.32(c) shows the spectra from the uncapped sample. There was also a small $C1s'$ peak found, taken at the interface between the metal layer and the carbon

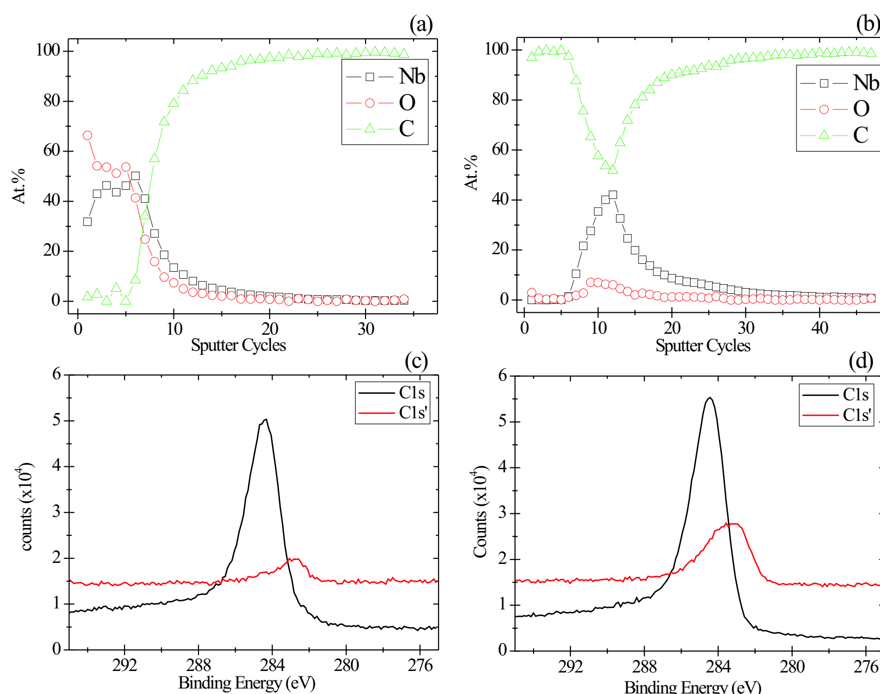

Figure 7.32: *XPS depth profile of an uncapped (a) and a capped (b) Nb-C sample. (c) and (d) show single $C1s$ spectra of the uncapped and the capped sample, respectively. The black line shows the normal $C1s$ peak position, while the red line shows the carbide $C1s'$ peak. The latter were found throughout the entire metal layer for the capped sample, and only in a very limited region near the metal-carbon interface in the uncapped sample.*

base-layer. However, the peak is smaller than for the capped sample, and only one or two $C1s'$ spectra were found. So we conclude for the uncapped sample, that a very small amount of carbide formed at the interface between the metal and the carbon, while the rest of the film oxidized completely.

The Nb-C system has been widely investigated in literature. Most of the production processes used are carburization methods using C-containing gases that react with the metal layer, or CVD methods. However, solid-state reactions can also be found. Barzilai *et al.* [15] examined $8 - 12\mu m$ thick Nb coatings on graphite, and found Nb_2C and NbC formation, after a heat treatment of 3h at $1100°C$ and $1500°C$, respectively. On diamond, Guarnieri *et al.* [16] annealed $200nm$ thick Nb layers for 30 minutes and observed the formation of Nb_2C at $700°C$, and NbC at $900°C$. NbC formation was observed by Zhang and Iijima [17] for carbon nanotubes (CNTs) that were heated for 20 minutes at $950°C$ on a Nb substrate.

7.8 The Molybdenum - Carbon system

CONFUSION with lead (Pb) up to the 18th century, led to the name of the 42nd element Molybdenum (*lead-like*). C.W. Scheele recognized molybdenum as

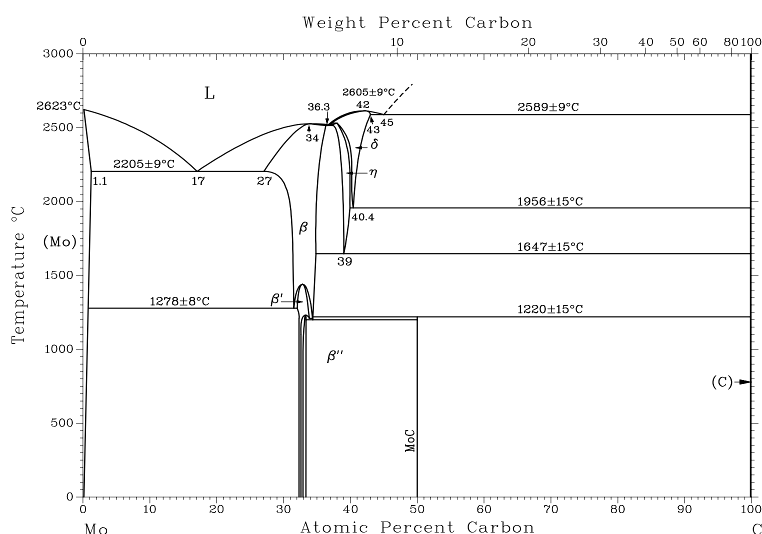

Figure 7.33: *Binary phase diagram for the Mo-C system [1].*

a distinct element in 1778 and in 1782, P.J. Hjelm isolated an impure extract of the metal by reducing the oxide with carbon. Molybdenum does not occur uncombined in nature, and its alloys are widely used because of their considerable heat- and corrosion-resistance. The use of Mo exploded during World War I, when tungsten became scarce for use in high-strength steels. In small amounts, Mo is very effective at hardening steel and improves the properties at high temperatures. That's why such alloys are found in aircraft parts and high-speed cutting tools.

Table 7.12: *Some basic properties of the pure metal Mo and the carbide phases Mo_2C and MoC.*

	Mo	Mo_2C	MoC
Crystal Structure	bcc	hcp	simple hex.
Melting Point $(°C)$	2623	2410	2690
Density (g/cm^3)	10.3	9.1	9.5
Moh's hardness	5.5	7-9	7-8
Electrical resistivity $(\mu\Omega cm)$	5	71	77
Thermal conductivity $(W/K\ m)$	139		30

According to figure 7.33, two stable molybdenum carbides exist, Mo_2C and MoC. Table 7.12 lists some properties of the different phases. One can learn from the table that the pure metal has a very high melting point and a high density (both higher than its carbide phases). The monocarbide phase MoC does not have the expected fcc structure, but a *simple hexagonal* structure.

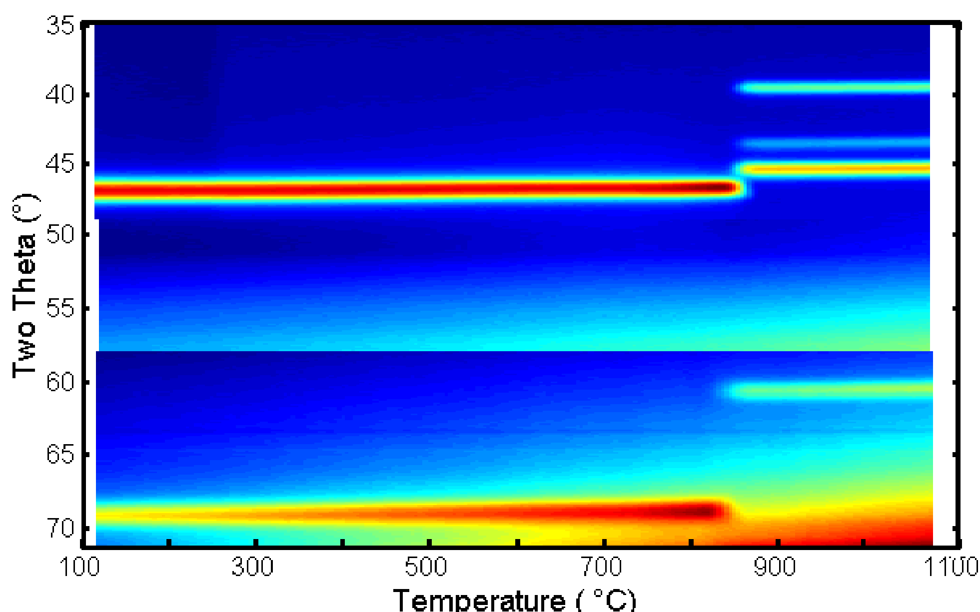

Figure 7.34: *in situ XRD measurements performed on a Mo-C sample, without a capping layer. Three 2θ windows have been combined.*

Figure 7.34 shows the *in situ* experiment for an uncapped Mo-C sample. Three 2θ windows have been combined in this figure. Between $830°C$ and $900°C$ a new phase is formed. The peak positions of the new phase correspond to the peaks of the hexagonal Mo_2C carbide phase, as evidenced in table 7.13. For completeness, we must mention that the Nb_2C phase can also be orthorhombic, which has about the same XRD pattern. RBS and XPS confirmed that the oxygen concentration of the annealed sample was very low. The *in situ* experiment on a sample with 30nm C capping layer, can be seen in figure 7.35. Clearly, the same phase formation occurred as for the uncapped sample.

While the phase sequence is identical for capped and uncapped Mo samples, there is a distinct difference in the reaction kinetics. Figure 7.35 shows *in situ* experiments of Mo-C samples with different capping layers. From top to bottom, the Mo-C system has no capping layer, 5nm C, 30nm C, or 30nm TiN capping layer. In all cases, the Mo_2C phase is formed, but the formation temperature varied significantly. Transition temperatures between $T^{5nmC} = 730°C$ and $800°C$, $T^{30nmC} = 700°C$ and

Table 7.13: *The most important diffraction peaks of the pure Mo metal and the carbide phase Mo_2C, in the 2θ window $\approx 35°$ to $\approx 70°$.*

Mo		Mo_2C	
2θ	hkl	2θ	hkl
		40.3	(100)
		44.6	(002)
		46.3	(101)
47.6	(110)		
		61.8	(102)
69.6	(200)		

$770°C$ and $T^{TiN} = 750°C$ and $830°C$ were observed, for the 5nm C, 30nm C and 30nm TiN capping layers respectively. The difference in formation temperature can be attributed to a competition between C, O and N, for the interstitial sites [18]. Without a capping layer, some impurities from the annealing atmosphere can enter the lattice and occupy interstitial sites. These interstitial locations facilitate C diffusion and are therefore important during carbide formation. As a result, the more interstitial sites that are occupied by other elements than C, the harder it is to form the carbide phase, and the higher the formation temperature. We observe that a 5nm C capping layer already reduces the O diffusion within the Mo film, which makes it easier for the C to occupy the interstitial sites, and we get a lower formation temperature. Increasing the thickness of the C capping layer to 30nm, blocks the O diffusion even more and thus the formation temperature for the carbide is lowered again. When a 30nm TiN capping layer is used, there may be some N moving into the Mo lattice, which would explain the increase in formation temperature, compared to the C capping layers.

Roth *et al.* [7] studied the chemical interaction of a 100nm Mo layer on a graphite surface. Mo_2C was formed after annealing for 15 minutes at $927°C$, and they observed that oxygen does not influence the carbide formation. They suggest that the oxygen, which is present in the as-deposited layer, reacts with carbon, followed by a subsequent release as the volatile CO. On polycrystalline diamond films, Mikhailov *et al.* [19] observed the transformation of a 200nm Mo layer into Mo_2C after 1 hour annealing at $800°C$.

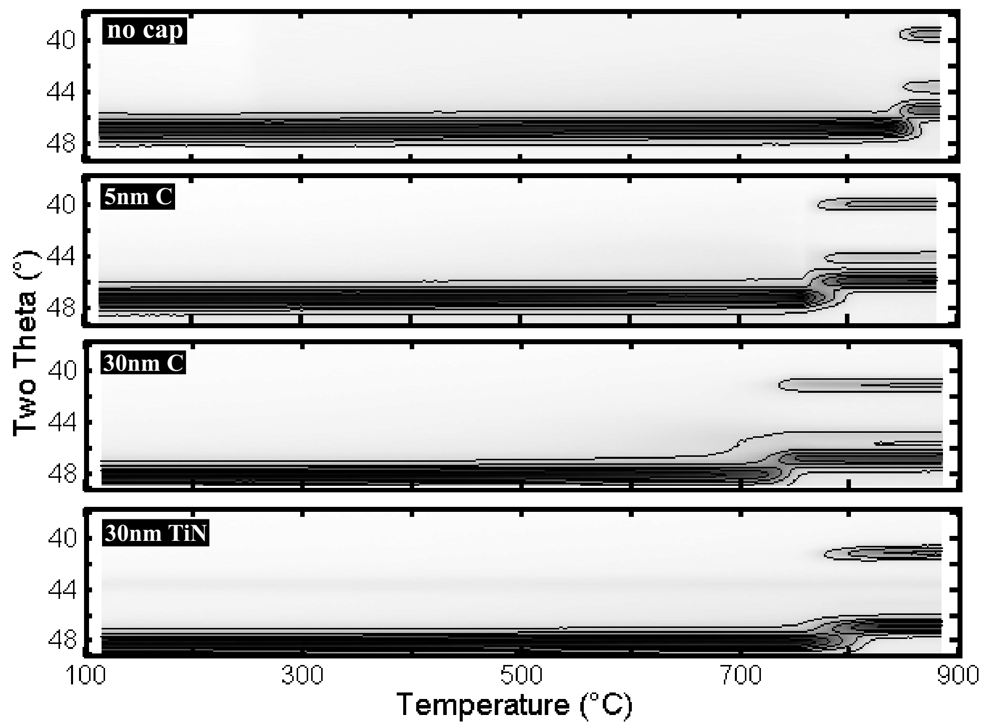

Figure 7.35: *in situ XRD measurements performed on Mo-C samples with different capping layers. From top to bottom: no capping layer, 5nm C, 30nm C, and 30nm TiN capping layer.*

7.9 The Hafnium - Carbon system

COPENHAGEN in Latin is '*Hafnia*', which is the basis of the name of the 72nd element. The existence of hafnium was suspected for years by many scientists, who, by using the Bohr theory (whom himself is from Copenhagen), predicted an element that was associated with zirconium. Finally in 1923, D. Coster and G. von Hevesy demonstrated the existence of the element using X-ray spectroscopy. The

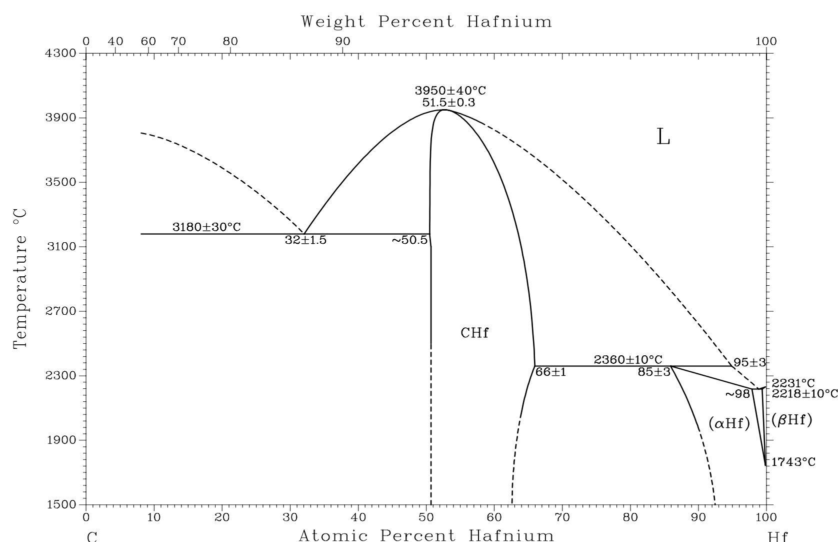

Figure 7.36: *Binary phase diagram for the Hf-C system [1].*

metal hafnium cannot be found in its pure form in nature, and it is usually found as an impurity in zirconium. Both elements have comparable chemical properties and are among the most difficult to separate. About half of all hafnium metal manufactured is produced as a by-product of zirconium refinement. Finely powdered, hafnium can

Table 7.14: *Some basic properties of the pure metal Hf and the carbide phase HfC.*

	Hf	HfC
Crystal Structure	hcp	fcc
Melting Point $(°C)$	2233	3890
Density (g/cm^3)	13.3	12.7
Moh's hardness	5.5	9-10
Electrical resistivity $(\mu\Omega cm)$	30	37
Thermal conductivity $(W/K\ m)$	23	22

spontaneously ignite in air; because of this reactivity the metal has found use in the manufacturing of light bulbs and vacuum tubes as a scavenger for small amounts of oxygen and nitrogen.

Figure 7.36 shows the binary phase diagram of the Hf-C system. Only the mono-carbide HfC is stable, and it has a very broad range of composition $0.59 \leq x \leq 0.96$, with x the carbon-to-metal ratio. Table 7.14 gives some basic properties of the metal and its carbide phase.

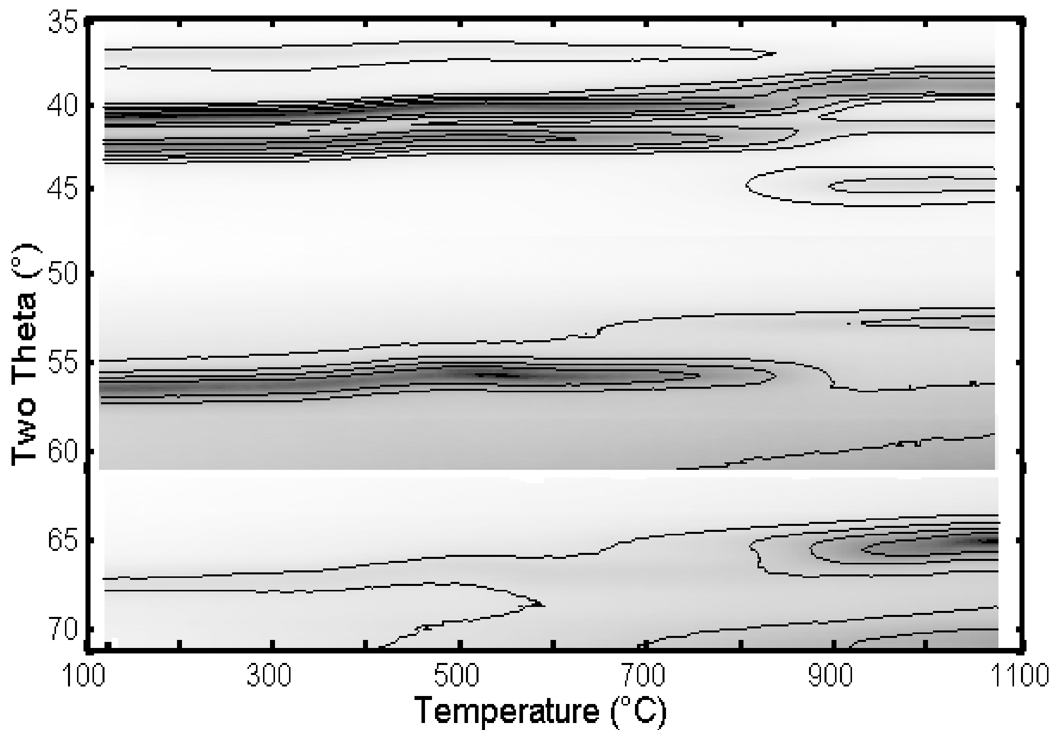

Figure 7.37: *in situ XRD measurements performed on a Hf-C sample, without a capping layer. Three 2θ windows have been combined.*

The *in situ* XRD measurements for the uncapped Hf-C system are shown in figure 7.37, where three 2θ windows have been combined into one figure. At the start of the experiment the Hf peaks can be clearly observed. Around $850°C$ a new phase is formed. It was not possible to identify the phase from the XRD data, but RBS measurements on a sample annealed to $1100°C$ show a high oxygen concentration. The RBS spectrum of the Hf peak, shown in figure 7.38 has an asymmetry, which indicates that the film is incompletely oxidized. This might explain why the diffraction peaks don't have a good correspondence to the XRD spectra of the different HfO_2 phases, as listed in table 7.15.

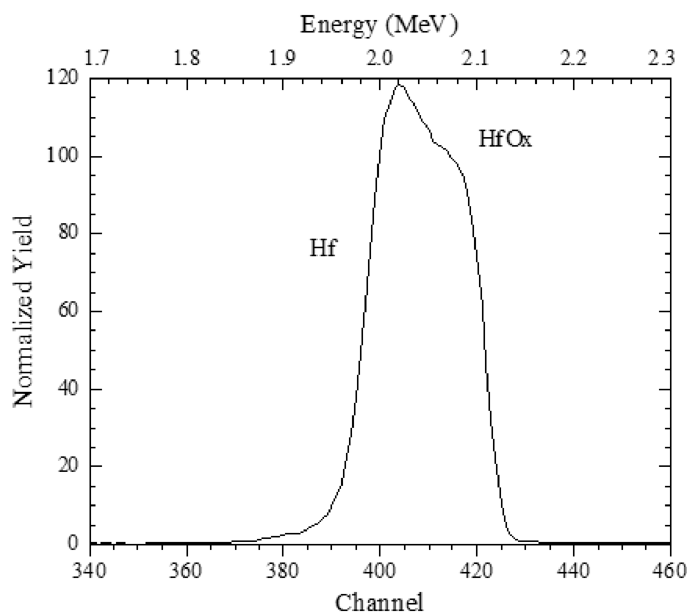

Figure 7.38: *RBS spectrum of the Hf peak, measured on a Hf-C sample without a capping layer, annealed to* $1100°C$.

With a 30nm C capping layer, the *in situ* XRD experiments on the Hf-C system looks different, as shown in figure 7.39. Between $710°C$ and $810°C$ a new phase is formed with diffraction peaks at $2\theta \approx 39°$, $\approx 45°$ and $\approx 66.5°$. These correspond to the (111), (200) and (220) peaks of the cubic HfC carbide phase, respectively. Table 7.15 lists these peaks, next to the peaks of the oxides.

Zhang *et al.* [20] deposited Hf films of 5nm thickness onto CNTs and performed an annealing in high vacuum for 4h. After annealing at $800°C$ they did not observe any carbide formation. However, after annealing at $1200°C$ they found that HfC had formed trough a solid-solid reaction. Because they don't use a capping layer on top of their Hf metal, it is understandable they needed higher annealing temperatures to achieve carbide formation. Toth [2] stated that to achieve bulk HfC materials from a direct reaction, very high temperatures of $1900 - 2300°C$ and a good vacuum is needed.

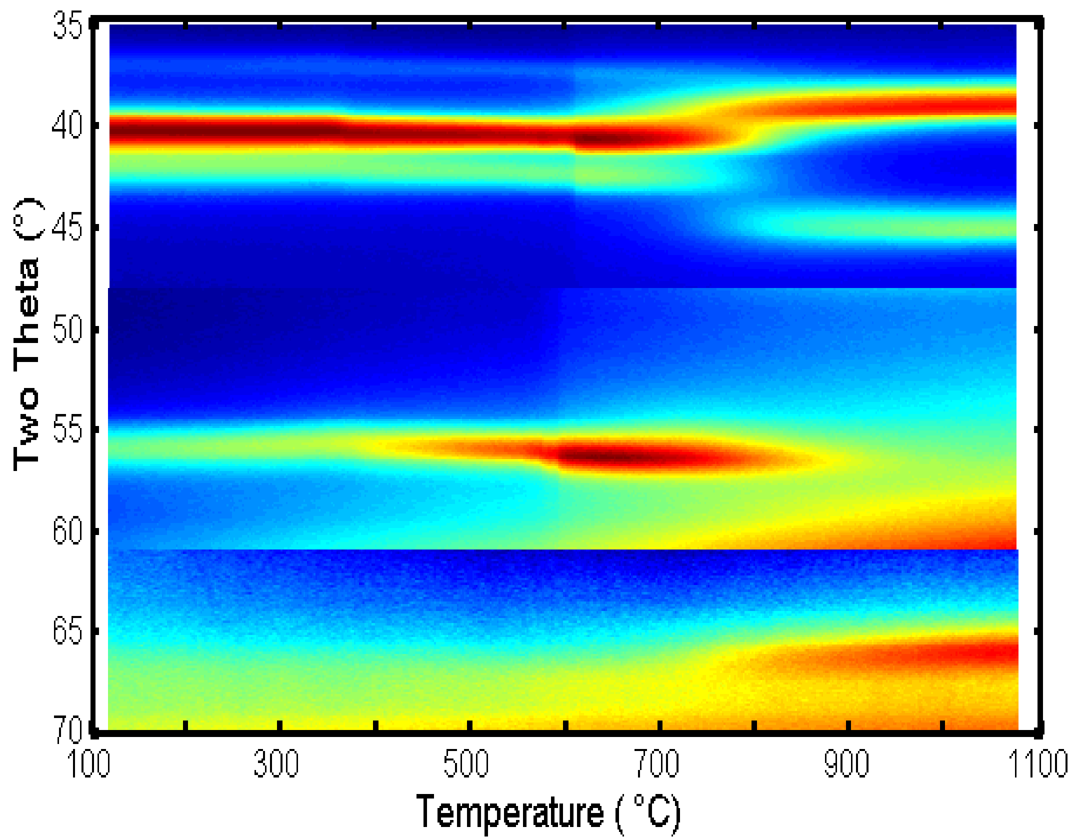

Figure 7.39: *in situ XRD measurements performed on a Hf-C sample, with a 30nm C capping layer. Three 2θ windows have been combined.*

Table 7.15: *Overview of the observed XRD peaks in the in situ experiment of the Hf-C system, and the XRD peaks of the suggested phases for the temperature ranges. A: low temperature peaks, B&C: high temperature peaks of the uncapped and capped sample, respectively.*

2θ	A	B	C	Hf °	Hf *hkl*	HfO_2(T) °	HfO_2(T) *hkl*	HfO_2(M) °	HfO_2(M) *hkl*	HfC °	HfC *hkl*
35						35.2	()*				
37	■			37.8	(100)			37.1	(111)		
		■									
39			■							39.2	(111)*
						40.1	(002)	40.2	(002)		
41	■	■		41.6	(002)	41.2	(200)	41.7	(200)		
43	■			43.4	(101)*						
		■				44.8	(102)				
45			■							45.6	(200)
47											
								48.2	($\bar{2}$11)		
49											
51											
		■									
53											
55											
57	■			57.5	(102)						
						58.6	(202)	58.5	(022)		
59						59.5	(220)	59.6	(220)		
								60.1	($\bar{1}$22)		
61											
63											
								64.4	(202)		
65		■									
			■					66.0	(221)	66.4	(220)
67											
	■			68.4	(110)						
69						69.4	()				
						70.9	(311)				

7.10 The Tantalum - Carbon system

TANTALUS was already mentioned in this work, as in Greek mythology he is the father of Niobe after whom niobium was named. He is also known from the '*Torment of Tantalus*', now commonly known as something highly desirable, but unreachable. The 73rd element's non-reactivity with other reagents was probably seen as something highly desirable, and so the element's name was linked to Tantalus. Tantalum was discovered in 1802 by A.G. Ekeberg, but was for a longtime confused with niobium. As a pure metal, it has a very high melting point (see table 7.16), and only the melting points of tungsten and rhenium exceed it.

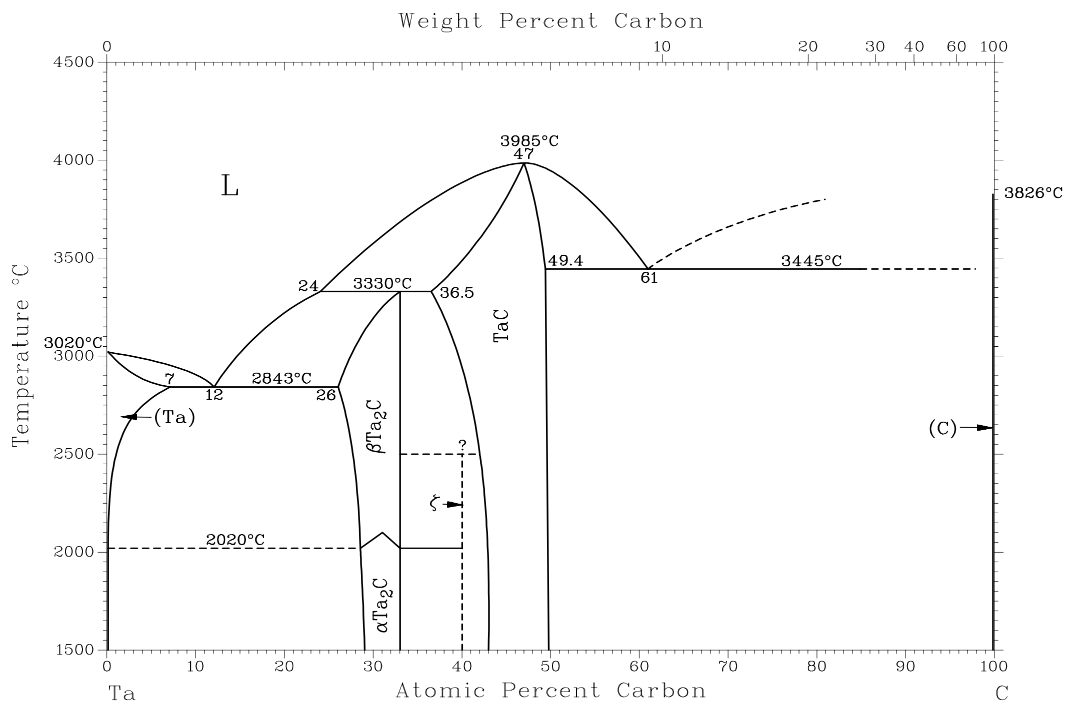

Figure 7.40: *Binary phase diagram for the Ta-C system [1].*

Tantalum forms two stable carbide phases, as can be seen from figure 7.40. They both have a certain range of composition, $0.41 \leq x \leq 0.50$ for the metal-rich carbide Ta_2C and $0.75 \leq x \leq 1$ for the monocarbide TaC, with x the carbon-to-metal ratio. Los Alamos National Laboratory developed a 'tantalum carbide-graphite composite material', one of the hardest materials ever synthesized. As can be seen in table 7.16, the monocarbide is very hard and has a very high melting point.

Table 7.16: *Some basic properties of the pure metal Ta and the carbide phases Ta_2C and TaC.*

	Ta	Ta_2C	TaC
Crystal Structure	bcc	hcp	fcc
Melting Point $(°C)$	3017	3400	3880
Density (g/cm^3)	16.7	15.2	14.5
Moh's hardness	6.5		9-10
Electrical resistivity $(\mu\Omega cm)$	13		25
Thermal conductivity $(W/K\ m)$	57		22

Figure 7.41 shows *in situ* XRD measurements on a Ta-C system without a capping layer. The phase which forms around $720°C$ could not be identified as one of the carbide phases for this system, so oxidation is very likely. Also, the metal peak makes a shift towards lower 2θ values, which hints towards oxidation. RBS measurements on a sample annealed to $1100°C$ confirmed a high oxygen concentration in the metal layer. The Ta RBS peak is asymmetric, which indicates partial oxidation, as was the case for the Hf-C system. The diffraction peaks observed correspond relatively well with those of the orthorhombic Ta_2O_5.

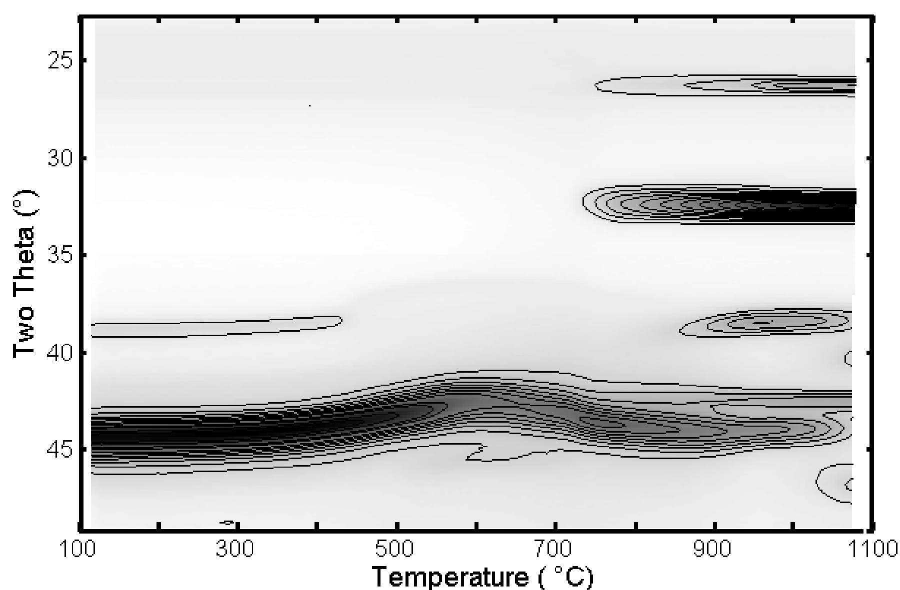

Figure 7.41: *in situ XRD measurements performed on a Ta-C sample, without a capping layer. Two 2θ windows have been combined.*

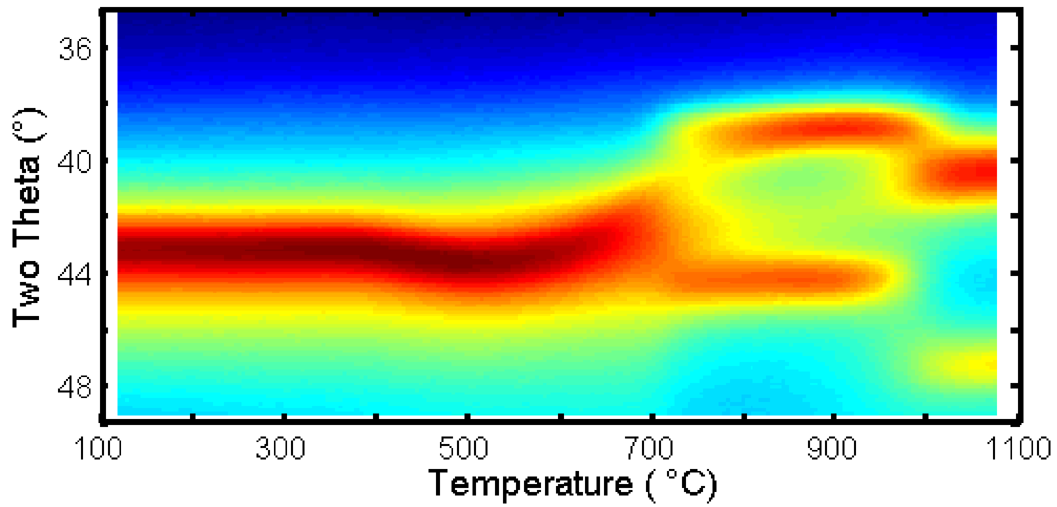

Figure 7.42: *in situ XRD measurements performed on a Ta-C sample, with 30nm C capping layer.*

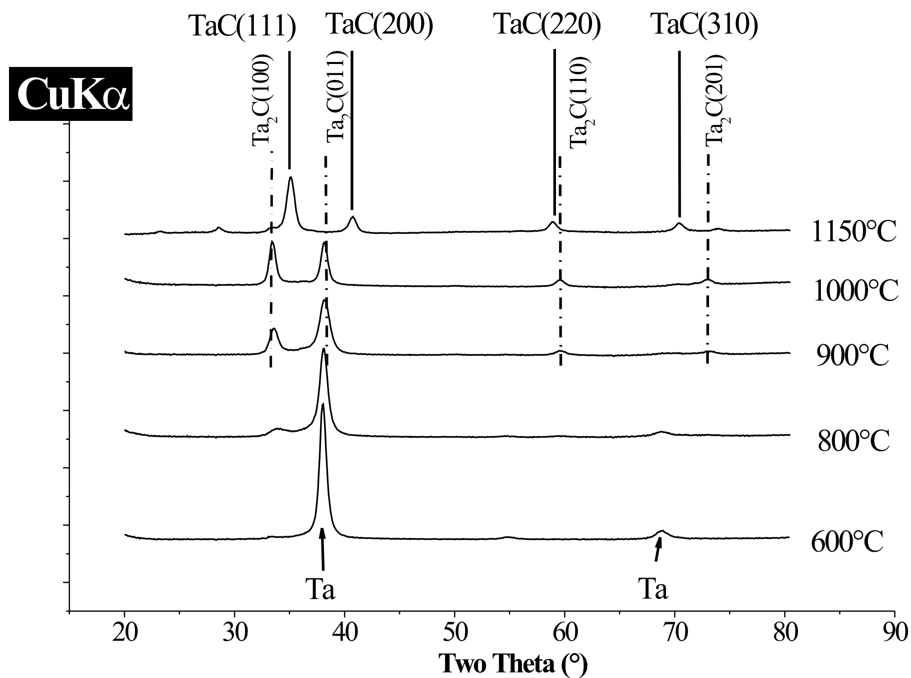

Figure 7.43: *Ex situ XRD measurements performed on Ta-C samples with 30nm C capping layer, that were annealed to different temperatures. The sequential formation of* Ta_2C *and* TaC *has been evidenced.*

The *in situ* XRD measurement of the Ta-C system with a 30nm C capping layer is shown in figure 7.42. Between $690°C$ and $750°C$ the $Ta(110)$ peak disappears, and the $Ta_2C(100)$ and $Ta_2C(110)$ peaks appear at $2\theta \approx 39°$ and $\approx 44.8°$, respectively. From $950°C$ to $1000°C$ the metal-rich carbide phase forms the monocarbide TaC with (111) and (200) peaks at $2\theta \approx 40.9°$ and $\approx 47.6°$, respectively. Although the phase sequence is correct, the formation temperatures given here are less than expected for a Ta-C system with 30nm of metal. Measurements following the *in situ* experiment showed that the thickness calibration was off for this system, and a thinner layer of Ta was deposited (and examined). *Ex situ* measurements on samples with a correct sample setup (30nm Ta on 200nm C, with 30nm C capping layer) show the same phases forming, although the transition temperatures are higher. A compilation of these *ex situ* measurements is shown in figure 7.43, and the diffraction peaks have been marked for the different phases. Unfortunately, *in situ* experiments were not available for this correct setup.

For the monocarbide phase, another problem occurs, namely the almost identical XRD peak positions for the fcc oxide TaO. Therefore, additional XPS measurements were performed on a sample annealed to $1100°C$. There was clear evidence found of carbide formation throughout the metal layer, when the $C1s$ spectra were examined. Figure 7.44(b) shows that the $C1s$ spectra, which were measured within the metal region of the depth profile, are at the carbide position. The normal $C1s$ spectrum is also shown (dashed line) as reference. From figure 7.44(a) one can observe that there is a considerable oxygen concentration present in the metal layer, so some oxide formation might also have occurred.

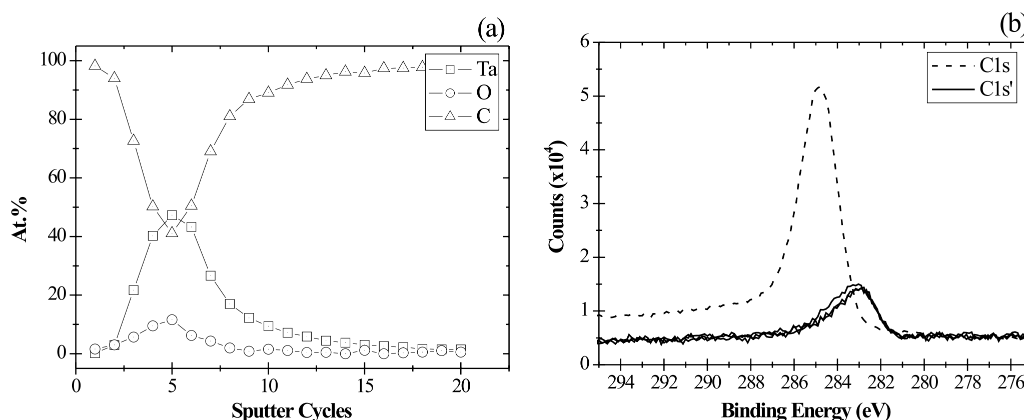

Figure 7.44: *(a) XPS depth profile of a Ta-C sample with 30nm C capping layer, annealed to* $1100°C$. *(b) XPS* $C1s$ *spectra.*

Chen *et al.* [21] reported on the thermal reaction of Ta thin films (60 - 135nm) with polycrystalline diamond. For the thinnest metal layer, they observed the phase formation of Ta_2C and TaC after annealing for 1h at $800°C$ and $900°C$, respectively. Pitter *et al.* [22] studied Ta layers of 1.5nm on single crystalline (100) diamond by Auger Electron Spectroscopy (AES) and Electron Energy Loss Spectroscopy (EELS). They observed characteristic carbide peaks in the AES spectra, and after annealing at $1000°C$ for 3 minutes they suggest the formation of TaC. Even on SiC, the carbide formation of Ta plays an important role. Chen *et al.* [23] deposited 320nm thick Ta layers on (001) β-SiC and found the formation of Ta_2C at the metal/SiC interface after annealing at $900°C$ for 1h. Annealing the structure for 1h at $1000°C$, produces TaC at the interface. Of course, various Ta-silicides are also formed during the process, but the carbide layers always formed at the interface with the SiC. This is very important in the SiC-technology, for the electrical properties of the contacts and the interface.

7.11 The Tungsten - Carbon system

WOLFRAM and tungsten both are names for the 74th element of the table. In Swedish, Danish and Norwegian *tung sten* means 'heavy stone', but ironically the current name for the element in these languages is wolfram. The word wolfram

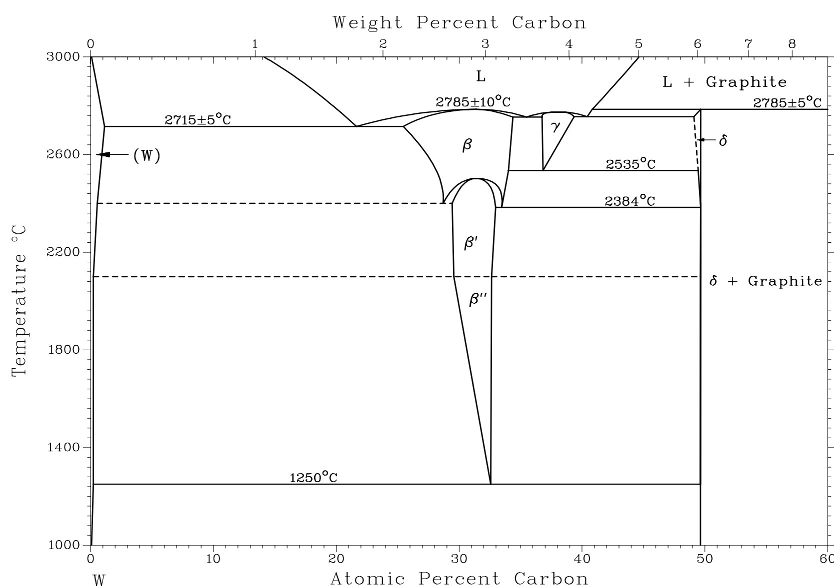

Figure 7.45: *Binary phase diagram for the W-C system [1].*

derives from the German *wolf's rahm*, literally meaning 'wolf's foam' or 'spuma lupi', which is how wolframite was traditionally known by the Saxon miners. The pure element was isolated from wolframite and this was done for the first time in 1783 by the de Elhuyar brothers. The metal is one of the most dense and has a higher melting point than any other metal.

Table 7.17: *Some basic properties of the pure metal W and the carbide phases W_2C and WC.*

	W	W_2C	WC
Crystal Structure	bcc	hcp	simple hex.
Melting Point $(°C)$	3422	2800	2750
Density (g/cm^3)	19.3	17.2	15.8
Moh's hardness	7.5	9-10	9
Electrical resistivity $(\mu\Omega cm)$	5	80	25
Thermal conductivity $(W/K\ m)$	170		84

Table 7.17 gives some properties of the metal, along with some for its carbide phases. From the binary phase diagram (figure 7.45) one can see that there are two stable tungsten carbides, namely W_2C and WC. The metal-rich carbide phase has a composition range of $0.41 \leq x \leq 0.50$, while the monocarbide is a line phase. Due to its extreme hardness, tungsten carbide is often used as a cheaper alternative to diamond in the manufacturing of cutting tools.

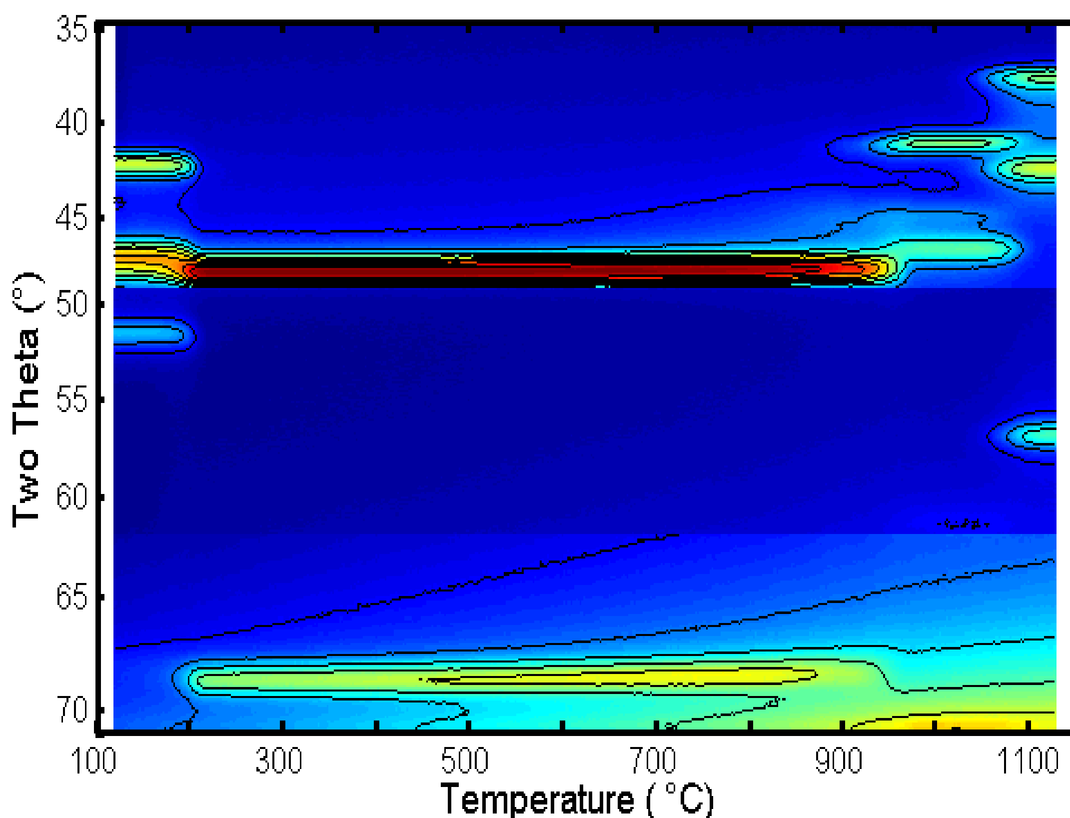

Figure 7.46: *in situ XRD measurements performed on a W-C sample, with 30nm C capping layer. For this system, the samples were annealed to* $1150°C$ *at the standard rate of* $3°C/s$*. Three* 2θ *windows have been combined into one figure.*

Figure 7.46 shows the *in situ* XRD measurement for the W-C system with a 30nm C capping layer. The measurement without a capping layer is not shown, because it is identical to figure 7.46, except for the transition temperatures, which are higher, as was explained in section 7.8. The experiment shown starts from the $\beta - W$ phase, which transforms into $\alpha - W$ around $200°C$. This doesn't affect the carbide formation, as was confirmed by *in situ* measurements of the solid-state reaction, starting from α-W. There is a clear phase-transition from W to W_2C in the temperature range of

Table 7.18: *Overview of the XRD peaks for the different phases discussed for the W-C system. The theoretical most intense peaks are marked with a star. The peak not visible on the experimental in situ XRD graph, is marked in grey.*

T	$100°C$		$200°C$		$950°C$		$1075°C$	
	$\beta - W$		$\alpha - W$		W_2C		WC	
	°	*hkl*	°	*hkl*	°	*hkl*	°	*hkl*
							36.9	(001)
					40.5	(100)		
	41.7	(200)					41.8	(100)*
					44.7	(002)		
					46.5	(101)*		
	46.9	(210)*						
			47.3	(110)*				
	51.7	(211)						
							57.0	(101)
					61.9	(102)		
			69.2	(200)				
T	$100°C$		$200°C$		$950°C$		$1075°C$	

$920°C$ to $970°C$. From $1050°C$ to $1100°C$ the metal-rich carbide phase transforms into the simple hexagonal monocarbide WC. Table 7.18 gives an overview of the peaks of the different phases that can be observed in the *in situ* experiment. RBS measurements performed on uncapped samples confirmed the carbide formation and there was no oxygen detected in the layers (detection limit is around $3\ at\%$).

Bachli *et al.* [24] and also Yeh *et al.* [25] reported on tungsten carbide formation by annealing a thick W film (135nm or 200nm, respectively) on polycrystalline diamond, and found the same phase sequence (first W_2C, then WC) after annealing for 1h. The temperatures they found differ for the different researchers; $900°C$ and $1100°C$ in the work of Bachli *et al.*, $800°C$ and $900°C$ in the work of Yeh *et al.*, for W_2C and WC formation respectively. The difference in formation temperatures is probably due to the long annealing times combined with the *ex situ* measuring techniques, which give an incomplete picture of the phase formation.

Baud *et al.* [26] studied the reaction of thin W films (500nm) on β-SiC. They observed the start of both W_2C and W_5Si_3 formation after annealing for 60s at $950°C$. The whole metal layer was transformed into these reaction products, after annealing the sample for 60s at $1100°C$. From their thermodynamic calculations they suggest that these reaction products are not the stable phases on SiC, but for longer annealing times, WSi_2 and WC are expected as stable phases.

7.12 Summary

SUMMARIZING the results, tables 7.19 and 7.20 give a comprehensive overview of the carbide phase formation for the various transition metals. The various metals are listed in table 7.19, with the carbide phases in order of appearance, as observed by our *in situ* experiments. In the last two columns, we list the necessity of a capping layer for each system.

Table 7.19: *The transition metals studied in this work, sorted by electronegativity (EN). The phase sequence for the solid-state reaction are listed in order of appearance. The last two columns indicate for which materials a capping layer is absolutely necessary to obtain carbide formation.*

Metal	EN	Phases	TF-Exp without Cap	TF-Exp with Cap
W	2.36	W_2C,WC	Carbide	Carbide
Mo	2.16	Mo_2C	Carbide	Carbide
Fe	1.83	Fe_3C,γ-Fe/α-Fe	Carbide	Carbide
Cr	1.66	Cr_2C/CrO_2,Cr_3C_{2-x},Cr_3C_2	Oxide -Carbide	Oxide -Carbide
V	1.63	V_2C/V_xO_y,VC	Oxide -Carbide	Oxide -Carbide
Nb	1.60	Nb_2C,NbC	Oxide	Carbide
Mn	1.55	MnO	Oxide	Oxide
Ti	1.54	TiC	Oxide	Carbide
Ta	1.50	Ta_2C,TaC	Oxide	Carbide
Zr	1.33	Zr_3O,ZrO	Oxide	Oxide
Hf	1.30	HfC	Oxide	Carbide

Oxidation is one of the main problems when using solid-state reactions to form carbides. We found that W, Mo, Fe, Cr and V form a carbide, even when no capping layer is applied. The others (Nb, Ti, Ta, and Hf) however, need the C capping layer or an oxide will form instead of a carbide. In table 7.19 the elements are arranged with decreasing electronegativity. The metals last mentioned here (Nb, Ti, Ta, and Hf) have a lower electronegativity compared to *e.g.* W and Mo, so they have a greater 'natural attraction' towards oxygen (which has an electronegativity of 3.44). So, one expects that these metals have a bigger chance of forming an oxide rather than a carbide. Cr and V are actually in between the two groups (W, Mo and Fe versus Nb, Ti, Ta, and Hf), which may explain why they tend to first form an oxide, but eventually the carbide phase governs the solid-state transformation. Mn and Zr are exceptions, as we weren't able to form a carbide phase for these metals. For Mn, the ionic bond with oxygen to form MnO is very stabilizing, which might explain its oxide-forming behaviour.

Table 7.20 lists the formation temperatures that were derived from the *in situ* XRD measurements, by annealing at $3°C/s$. The results are those for 30nm metal - C systems, with 30nm C capping layer. For the Ta-C system, the values are marked with an asterisk, because of the bad sample setup (<30nm metal).

Table 7.20: *Formation temperatures for the carbide phases that formed by a solid-state reaction of 30nm metal and 200nm C, capped with 30nm C. The in situ experiments were performed at a heating rate of $3°C/s$. MC_x shows the range of composition over which the carbide is stable (estimated from the binary phase diagram).*

Carbide Phase	T$_{form}$ ($°C$)	MC_x
W_2C	920 - 970	0.41 - 0.50
WC	1050 - 1100	=1
Mo_2C	700 - 770	0.47 - 0.50
Fe_3C	510 - 550	=0.25
Cr_2C	580 - 620	-
Cr_3C_{2-x}	740 - 770	-
Cr_3C_2	900 - 950	0.65 - 0.66
VC	680 - 730	0.74 - 0.92
Nb_2C	690 -	0.48 - 0.49
NbC	880 - 940	0.72 - 0.98
TiC	550 - 650	0.70 - 0.98
Ta_2C	690 - 750*	0.41 - 0.50
TaC	950 - 1000*	0.75 - 1
HfC	710 - 810	0.59 - 0.96

Electrical resistivity is an important property for electrical contacts. Therefore, table 7.21 lists resistivity values for the carbide phases. The first column are measured on the carbide phases formed through a thin film solid-state reaction as discussed in this chapter. The lowest measured values are listed, and a variation of approximately $10\mu\Omega cm$ between similar samples, was found. The experimentally measured resistivity values are higher than those found in literature, which can partially be explained by the difference in thin films to bulk samples. Furthermore, the range of composition of the carbide phase will reflect itself in a change of certain physical properties of the carbide, like the resistivity. This because C-vacancies act as powerful scattering centers for electrons and phonons. The resistivity increases with carbon vacancy concentration, and this probably explains the higher values we measured compared to literature. It is clear that one has to take this into account, when searching for appropriate contacts for semiconductors.

Considering the thin film samples, one can see that all values lie between 59 and 300 $\mu\Omega cm$. This is higher than the resistivities of the contact materials which are currently used (*e.g.* $\rho^{NiSi} = 10 - 15\mu\Omega cm$), but it is comparable to that of some other metals (*e.g.* $\rho^{Er} = 103\mu\Omega cm$).

Table 7.21: *Electrical resistivities for the different carbide phases. The first list (ρ) are experimentally obtained values, measured on the carbide phases, formed through the thin film solid-state reaction as discussed in this chapter. The last column summarizes the resistivities (ρ^{lit}) that were listed at the beginning of each section in this chapter, and are obtained from literature [2, 18].*

Carbide Phase	ρ ($\mu\Omega cm$)	ρ^{lit} ($\mu\Omega cm$)
W_2C	114	80
WC	300	25
Mo_2C	59	71
Fe_3C	180	
Cr_2C		
Cr_3C_{2-x}	72	
Cr_3C_2	167	75
VC	214	60
Nb_2C	160	60
NbC	107	35
TiC	136	68
Ta_2C	163	
TaC	132	25
HfC	178	37

Several criteria should be used to select the best candidate for contacting carbon-containing semiconductors. The last formed carbide phases of the systems: WC, Mo_2C, Fe_3C, Cr_3C_2, VC, NbC, TaC, and HfC, are most stable at the highest temperatures. For the Fe-C and the Cr-C system, carbide-mediated graphitization was observed, which suggests that the carbide phase will eventually disintegrate, as was observed for the Fe-C system, which formed $\gamma - Fe$ at high temperatures. Secondly, one has to take the formation temperature into account. From table 7.20, the remaining carbide phases in order of increasing formation temperature, are: TiC, VC, Mo_2C, HfC, NbC, TaC and WC. From our research it was also evidenced that W, Mo, Fe, Cr and V don't have the absolute necessity of a capping layer, which facilitates the fabrication of the contact. Cr and V first form oxides, which may cause problems when more oxygen is available during the processing. From the remaining candidates, Mo_2C has a relatively low formation temperature, and evenmore, has a narrow range of composition which limits the possible variation of the resistivity. Therefore, one may conclude that Mo_2C seems a promising candidate for contacting carbon-containing semiconductors.

Bibliography

[1] T. B. Massalski. *Metall. Trans. A*, 20(8):1295, 1989.

[2] L.E. Toth. *Transition Metal Carbides and Nitrides*, volume 7 of *Refractory Materials, A Series of Monographs*. Academic Press, New York, 1971.

[3] S. Miller, R. Fischer, H. Plank, J. Roth, and V. Dose. *J. Appl. Phys.*, 82(7):3314, 1997.

[4] L. Ramqvist, K. Hamrin, G. Johansson, A. Fahlman, and C. Nordling. *J. Phys. Chem. Solids (UK)*, 30(7):1835, 1969.

[5] C. D. Wagner, W. M. Riggs, L. E. Davis, J. F. Moulder, and G. E. Muilenberg. *Handbook of x-ray photoelectron spectroscopy*. Perkin-Elmer Corporation, Minnesota, 1979.

[6] R. Sinclair, T. Itoh, and R. Chin. *Microsc. microanal.*, 8(4):288, 2002.

[7] J. Roth, H. Graupner, S. P. Withrow, D. Zehner, and R. A. Zuhr. *J. Appl. Phys.*, 79(10):7695, 1996.

[8] V. N. Lipatnikov, A. I. Gusev, P. Ettmayer, and W. Lengauer. *J. Phys.-Condes. Matter*, 11(1):163, 1999.

[9] V. N. Lipatnikov, A. I. Gusev, P. Ettmeier, and W. Lengauer. *Phys. Solid State*, 41(3):474, 1999.

[10] J. G. Chen, B. D. Devries, B. Fruhberger, C. M. Kim, and Z. M. Liu. *J. Vac. Sci. Technol. A-Vac. Surf. Films*, 13(3):1600, 1995.

[11] Q. R. Hou, H. Y. Zhang, and Y. B. Chen. *Mod. Phys. Lett. B*, 19(21):1039, 2005.

[12] E. Bouzy, G. Lecaer, and E. Bauergrosse. *Philos. Mag. Lett.*, 64(1):1, 1991.

[13] E. Bouzy, E. Bauergrosse, and G. Lecaer. *Philos. Mag. B-Phys. Condens. Matter Stat. Mech. Electron. Opt. Magn. Prop.*, 68(5):619, 1993.

[14] A. Santaniello, J. Roth, and F. E. Wagner. *Nucl. Instrum. Methods Phys. Res. Sect. B-Beam Interact. Mater. Atoms*, 48(1-4):499, 1990.

[15] S. Barzilai, A. Raveh, and N. Frage. *Vacuum*, 79(3-4):171, 2005.

[16] C. R. Guarnieri, F. M. Dheurle, J. J. Cuomo, and S. J. Whitehair. *Appl. Surf. Sci.*, 53:115, 1991.

[17] Y. Zhang and S. Iijima. *Appl. Phys. Lett.*, 77(7):966, 2000.

[18] H. J. Goldschmidt. *Interstitial Alloys.* Butterworths, London, 1967.

[19] S. N. Mikhailov, D. Ariosa, J. Weber, Y. Baer, W. Hanni, X. M. Tang, and P. Alers. *Diam. Relat. Mat.*, 4(9):1137, 1995.

[20] J. H. Zhang, C. R. Yang, Y. J. Wang, T. Feng, W. D. Yu, J. Jiang, X. Wang, and X. H. Liu. *Nanotechnology*, 17(1):257, 2006.

[21] J. S. Chen, E. Kolawa, M. A. Nicolet, and F. S. Pool. *Thin Solid Films*, 236(1-2):72, 1993.

[22] M. Pitter, M. B. Hugenschmidt, and R. J. Behm. *Appl. Phys. Lett.*, 68(18):2508, 1996.

[23] J. S. Chen, E. Kolawa, M. A. Nicolet, R. P. Ruiz, L. Baud, C. Jaussaud, and R. Madar. *J. Appl. Phys.*, 76(4):2169, 1994.

[24] A. Bachli, J.S. Chen, R.P. Ruiz, and M-A. Nicolet. Solid-phase reaction of tungsten thin films with polycrystalline diamond. In *MRS Symposium Proceedings*, volume 339, page 247, 1994.

[25] J. J. Yeh, R. L. Pfeffer, M. W. Cole, M. Ohring, and J. E. Yehoda. *Diam. Relat. Mat.*, 5(10):1195, 1996.

[26] L. Baud, C. Jaussaud, R. Madar, C. Bernard, J. S. Chen, and M. A. Nicolet. *Mater. Sci. Eng. B-Solid State Mater. Adv. Technol.*, 29(1-3):126, 1995.

Chapter 8

Kinetics for the solid-state formation of carbides

IN THIS chapter we shall discuss the growth kinetics and mechanisms for the carbide formation, during a solid-state reaction. Therefore, a very brief overview of the growth models will be given (for a more thorough description see [1]), accompanied by an overview of literature regarding the growth process of carbide systems. Finally, an experimental procedure is discussed to extract kinetic parameters for the different metal-carbon systems.

8.1 The growth models

TWO different reaction types can be distinguished. DIFFUSION controlled reactions comprise three steps: (1) the creation of a reaction interface, (2) diffusion of atoms (metal and/or carbon) through the growing phase towards the reaction interface, and (3) the reaction of the diffusing atom at the interface to form the growing phase. At the beginning of the phase formation, the last step is always the rate limiting step. This 'reaction controlled' growth results in a linearly increasing thickness of the growing phase with time. As the phase grows thicker, the diffusion of the atoms through the growing phase is the rate limiting step, and the thickness will increase with the square root of time. It is the fastest diffusing atom that determines the formation rate, and it is therefore called the dominant moving species.

The previous explanation is for the growth of a single phase at a time. When multiple phases grow simultaneously, the process gets more complex with coupled growth of all (or some) phases, and possibly different mechanisms for each growth. We shall not discuss this problem. In general, diffusion controlled reactions are characterized by a planar growth of the new phase, resulting in a smooth interface.

In NUCLEATION controlled reactions, the laterally inhomogeneous creation of small nuclei is rate determining. These grow rapidly both vertically and laterally, and the resulting interface is rough. In this process, the competition between the gain in Gibbs free energy of the newly formed phase and the increase in surface energy, associated with the extra interface, implies a critical size for the nuclei. This critical size must be reached by the nuclei, to be energetically stable and grow. The rate of nucleation is very strongly temperature dependent. This will reflect itself in the fact that up to a certain temperature nothing happens, and above it, the reaction (and the diffusion) is usually very fast.

Considering the kinetics of the metal-carbon reaction, one can learn from literature that the reaction for carbide formation is controlled by the diffusion of carbon. A few examples are given. Peng *et al.* [2] reported this for TiC. Van Loo *et al.* [3] found from marker experiments in different types of diffusion couples, that carbon is virtually the only diffusing component in TiC_{1-y} and ZrC_{1-y}. Mikahilov *et al.* [4] showed that the Mo_2C growth in a Mo-CVD diamond system, is controlled by a diffusing process, and that C is the most probable diffusing element. Isobe *et al.* [5] also found a Mo_2C layer growth following the diffusion model, by studying Mo coatings on graphite. Yeh *et al.* [6] found that Mo_2C, W_2C and WC formed from the reaction of metal thin films with polycrystalline diamond, grow by a diffusion controlled process. Barzilai *et al.* [7] evidenced the diffusion controlled process for Nb_2C and NbC formation from Nb coatings on graphite. Woodford and Chang [8] evidenced that carbon is the only species undergoing significant diffusion in the Nb-C system. Pitter *et al* [9] showed that the reaction to TaC from thin metal layers on single crystalline diamond is controlled by the diffusion of carbon. Chen *et al.* [10] concluded the same for Ta-reaction with polycrystalline diamond. Zhu *et al.* [11] studied the reaction between a Cr layer and diamond particles, and concluded that the formation of a Cr_2C interlayer was governed by the diffusion of carbon. Fries *et al.* [12] reported that the rate-determining step of the diffusion process for carbide formation, is the diffusion of the carbon through the carbide phases.

8.2 Kissinger analysis

IN ORDER to obtain an apparent activation energy for the solid-state reactions, we applied a so-called Kissinger analysis. This is a modified Arrhenius plot (as it involves temperature dependencies), which can be applied to any thermally activated process involving a transition that can be monitored *in situ*. Colgan and d'Heurle [13] explained that the activation energy E_a can be determined from ramped *in situ* measurements, using this Kissinger method. The temperature corresponding to a fixed stage of transformation is measured as a function of the heating rate.

For diffusion limited growth, the thickness evolution can be written as

$$x^2 = \int_0^t K dt = \int_{T_0}^T K(dT/dt)^{-1} dT, \tag{8.1}$$

where K is an effective diffusion constant, dT/dt is a constant heating rate, T_0 is the starting temperature, and T is the temperature. For thermally activated growth, the diffusion constant can be written as

$$K = K_0\, e^{(-E_a/k_b T)}, \tag{8.2}$$

where K_0 is the pre-exponential factor called the reaction coefficient, k_b is the Boltzmann constant, and E_a is the activation energy.

Defining T_f as the temperature of the maximum rate of change of the measured variable, with x_f the corresponding thickness at temperature T_f, Mittemeijer [14, 15] simplified the integral obtained from combining equations 8.1 and 8.2. Furthermore, as the starting temperature T_0 is usually significantly less than T_f, the final form of the equation is

$$ln\left[\frac{dT/dt}{T_f^2}\right] = -\frac{E_a}{k_b T_f} - ln\left[\frac{x_f^2 E_a}{k_b K_0}\right], \tag{8.3}$$

with dT/dt the ramp rate (RR), T_f the formation temperature with x_f the corresponding thickness, k_b the Boltzmann constant, K_0 the reaction coefficient and E_a the activation energy.

The practical application of this Kissinger analysis, will be discussed in detail for the W-C system in the next section. The analysis for the other systems was analogous and we will not elaborate on the details there. Worth mentioning is that for the determination of E_a, it is not necessary to know the thickness of the layer. The latter, however, would enable one to determine the reaction coefficient K_0 from the y intercept of the Kissinger plot, once E_a has been determined.

8.3 Determining the activation energies for the W-C system

To obtain the activation energy, *in situ* XRD measurements were done at different heating rates (1, 3, 5, 9 and $27°C/s$). Figure 8.2(a) shows an *in situ* XRD measurement for the W-C system with 30nm C capping layer, that was annealed at $3°C/s$ from $100°C$ to $1150°C$. A transition temperature needs to be determined. For this, the summed intensity of the different peaks is plotted, see figure 8.2(b). In our calculations, the maximum of the first derivative of the intensity of the XRD-peak was used as the transition temperature. This is the temperature where the maximum rate of intensity change occurs. As an example, figure 8.2(c) shows the first derivative of '$WC(001)$' and '$W_2C(100)$', and the maxima (and hence the transition temperatures) are marked and labelled. For the W_2C peak, we get a transition temperature of $950.7°C$, for the WC peak $1061.7°C$. The same was done for the other peaks, and the final transition temperature (for each phase) is the average of these values.

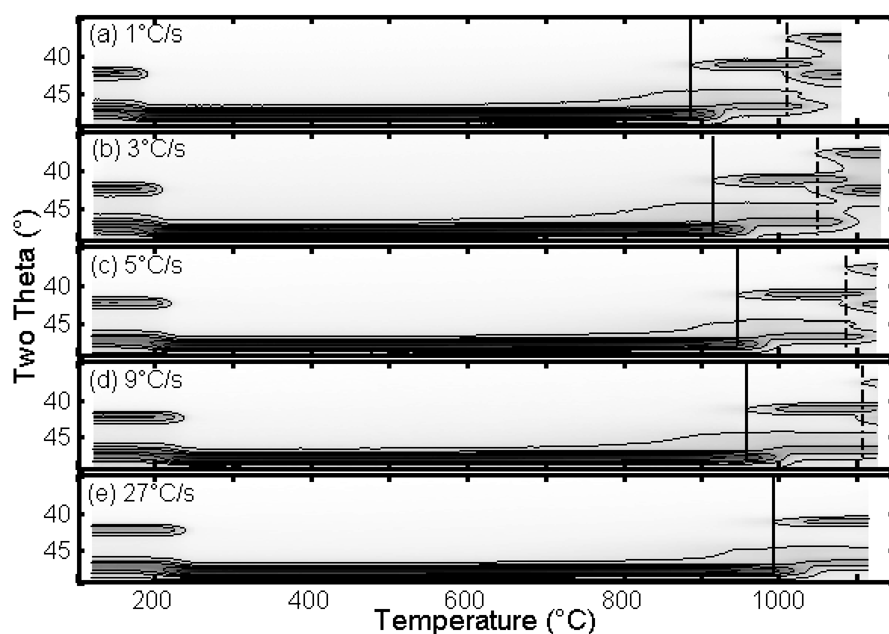

Figure 8.1: *In situ XRD measurements on W-C samples with 30nm C capping layer, annealed from $100°C$ to $1150°C$ at various ramp rates: (a) $1°C/s$, (b) $3°C/s$, (c) $5°C/s$, (d) $9°C/s$, and (e) $27°C/s$. The transition to the W_2C phase is marked with a full line, the transition to WC with a dashed line. At higher ramp rates, the transition temperatures shift towards higher values.*

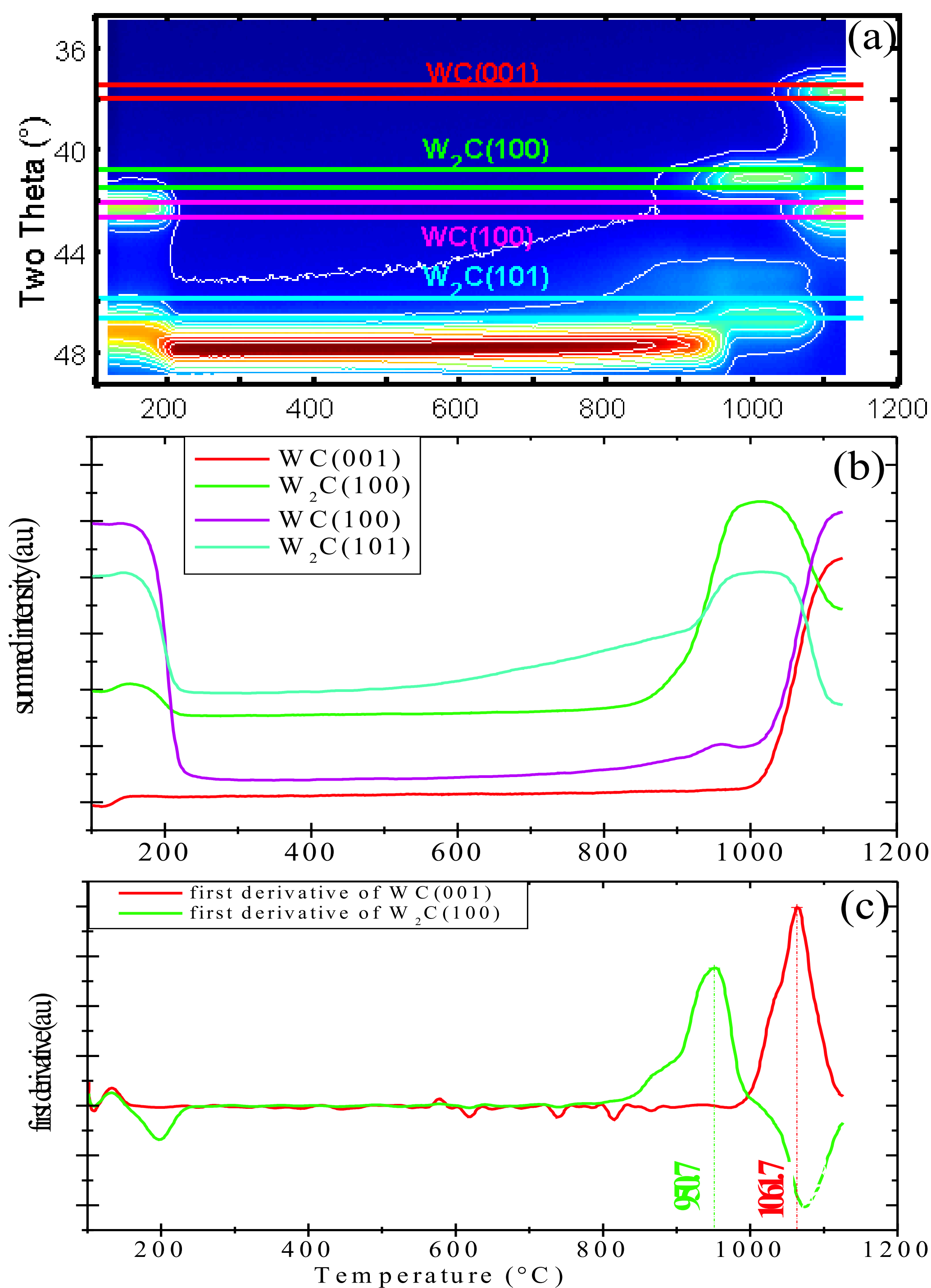

Figure 8.2: *(a): In situ XRD measurement of a W-C system with 30nm C capping layer, annealed at* $3°C/s$ *from* $100°C$ *to* $1150°C$*. (b): The summed intensities of the areas marked on the XRD measurement. (c): The first derivatives of the summed intensity of the* $WC(001)$ *and* $W_2C(100)$ *peaks. The maxima have been marked and labelled.*

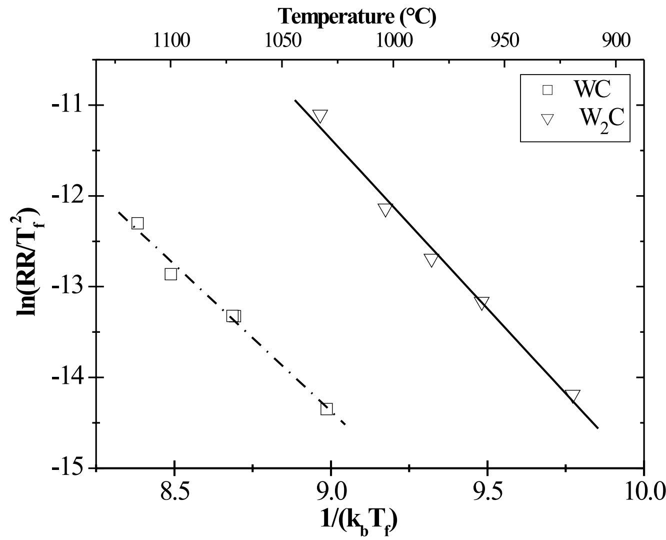

Figure 8.3: *Kissinger plots for the solid-state formation of W_2C and WC, from a W-C sample with 30nm C capping layer.*

As shown in figure 8.1 for the W-C system, the transition temperature shifts towards higher values, when the ramp rate is increased. This is clearly demonstrated in figure 8.1(e), where the transition from W_2C to WC doesn't take place in the measured temperature range ($100°C$ to $1150°C$), at a heating rate of $27°C/s$. The reason for this is that the 'total thermal budget' gets smaller, when the heating rate is higher.

Plotting $ln[(dT/dt)/T_f^2]$ vs $1/k_bT_f$ with T_f the transition temperatures determined (as discussed above) for the different ramp rates (dT/dt), one can fit a straight line to the data points (see figure 8.3). The slope of this straight line gives the activation energy, as can be derived from equation 8.3. The correlation coefficient (R) will be supplied for each plot, as an indication for the scatter of the data points from the fitted line. More details on the error determination is given in appendix C (page 163). The final calculated error on the activation energy will be supplied with their respective values.

Figure 8.3 shows the Kissinger plots for both phase formations of the W-C system with 30nm C capping layer. Straight lines have been fitted for the W-C Kissinger plots, and we have obtained activation energies of $E_a^{W_2C} = 3.74 \pm 0.29\ eV$ ($R = 0.9951$) for W_2C-formation, and $E_a^{WC} = 3.23 \pm 0.29\ eV$ ($R = 0.9932$) for WC-formation.

Buhsmer *et al.* [16] studied the self-diffusion of ^{14}C into WC, and obtained an activation energy $E_a^{b.d.} = 3.82\ eV$ for bulk diffusion, and $E_a^{g.b.d.} = 3.08\ eV$ for grain-boundary diffusion.

8.4 The activation energies for the other M-C systems

ACTIVATION ENERGIES were determined for most of the other carbide forming systems which were discussed in the previous chapter. The exceptions are the Ta-C system and the Cr-C systems, for which no good *in situ* XRD measurements were available at multiple ramp rates. The next subsections will give the results of the determination of the activation energy by using the Kissinger analysis, as was explained in the previous section, along with results from other researchers (when available in literature).

8.4.1 Ti-C:

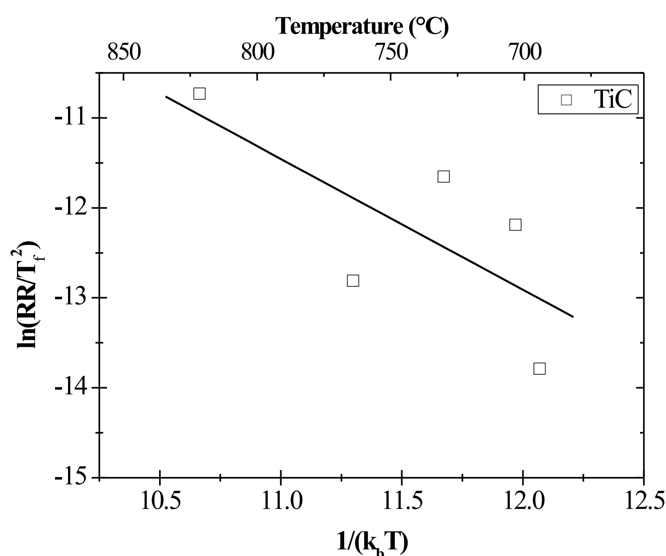

Figure 8.4: *Kissinger plot for the solid-state formation of TiC, from a Ti-C sample with 30nm C capping layer.*

For the Ti-C system, *in situ* XRD measurements were performed at 1, 3, 5, 9 and $27°C/s$ and the intensities of the TiC peaks at $2\theta \approx 42.1°$ and $\approx 49°$ were used to obtain the transformation temperatures for the Kissinger analysis. Figure 8.4 shows the Kissinger plot with the fitted line, which yields an activation energy for TiC formation of $E_a = 1.45 \pm 0.81\ eV$ ($R = 0.7184$). There is relatively large scatter on the data in the plot, which is also observable in the large error on the activation energy, and the low correlation coefficient. This might be due to high or sample-dependent impurity levels, which can play an important role, as will be discussed later in this chapter.

Van Loo *et al.* [3] reported on the carbon diffusion in TiC_{1-y}, and found the same activation energy for different carbon concentrations, namely $E_a = 3.42 \pm 0.21\ eV$.

Sarian *et al.* [17, 18] found different activation energies, ranging between $4.14\ eV$ and $4.77\ eV$, for different carbon concentrations. It should be mentioned that the latter researcher used ^{14}C tracer diffusion, and the experiments were done at relatively high temperatures ($1475°C - 2720°C$).

8.4.2 V-C:

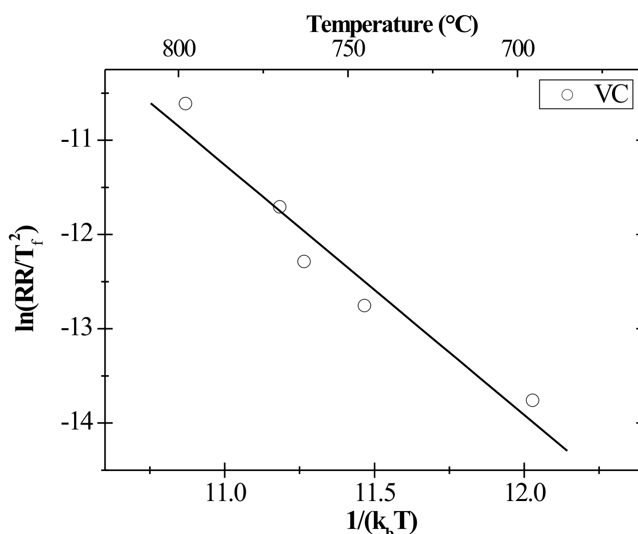

Figure 8.5: *Kissinger plot for the solid-state formation of VC, from a V-C sample with 30nm C capping layer.*

Figure 8.5 shows the Kissinger plot for the solid-state formation of VC from a V-C sample with 30nm C capping layer. The same heating rates were used as for the W-C system, and the 2θ peaks at $\approx 43°$ and $\approx 50.1°$ were used to calculate the data points. From this, an activation energy $E_a = 2.65 \pm 0.38\ eV$ ($R = 0.9709$) was determined.

Matzke [19] mentions an activation energy for the VC_{1-x} phase of $3.1 \pm 0.2\ eV$.

8.4.3 Fe-C:

For the Fe-C system, four diffraction peaks were used to calculate the transformation temperatures at the different heating rates, namely the (211), (102), (031) and (221) peaks of the Fe_3C phase. The transition temperatures were averaged for each heating rate, and they all were comprised within the usual error of $\pm 3°C$ that was imposed on the average. Figure 8.6 shows the Kissinger plot, and the calculated activation energy for the Fe_3C formation is $E_a = 4.05 \pm 0.83\ eV$ ($R = 0.9941$).

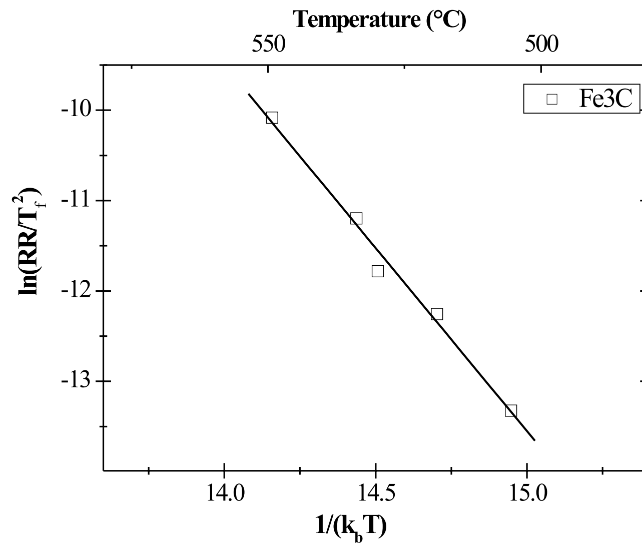

Figure 8.6: *Kissinger plot for the solid-state formation of Fe_3C, from a Fe-C sample with 30nm C capping layer.*

8.4.4 Nb-C:

The Nb-C system forms two carbide phases in its solid-state reaction, and for both the activation energy was obtained. For the metal rich phase, the (100) and (002)

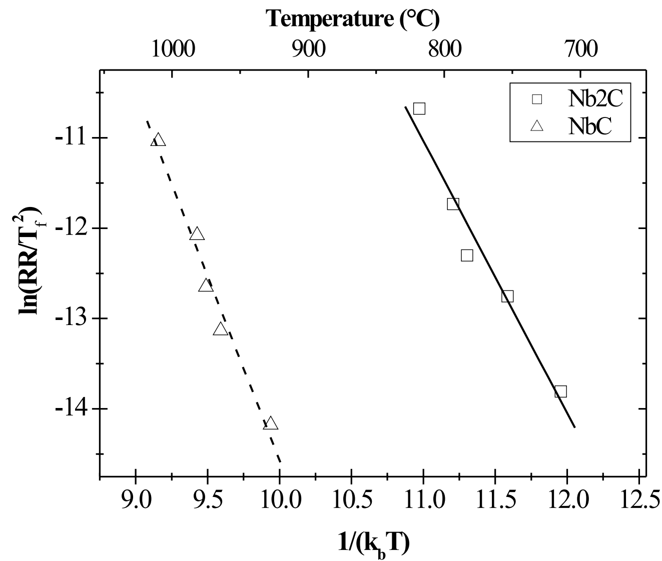

Figure 8.7: *Kissinger plots for the solid-state formation of Nb_2C and NbC, from a Nb-C sample with 30nm C capping layer.*

peaks at $2\theta \approx 38.8°$ and $\approx 42.4°$ were used for the calculation. The (101) peak was not useful for this, as the $Nb(110)$ metal peak is around the same 2θ value (it disturbs the summed intensity plot). For the determination of the activation energy of the monocarbide phase, the (111) and (200) peaks of NbC were used. Figure 8.7 shows the Kissinger plot for both phases, and the activation energies obtained are: $E_a^{Nb_2C} = 3.01 \pm 0.36\ eV$ ($R = 0.9797$) and $E_a^{NbC} = 4.08 \pm 0.37\ eV$ ($R = 0.9879$).

Barzilai *et al.* [20] found activation energies of $E_a^{Nb_2C} = 1.97\ eV$ and $E_a^{NbC} = 1.70\ eV$, which is lower than the values obtained in our research. Many others found activation energies, which are in the same region as our results, i.e. $3.25\ eV$ for Nb_2C [21], and $3.30 - 4.55\ eV$ for NbC [21–23].

8.4.5 Mo-C:

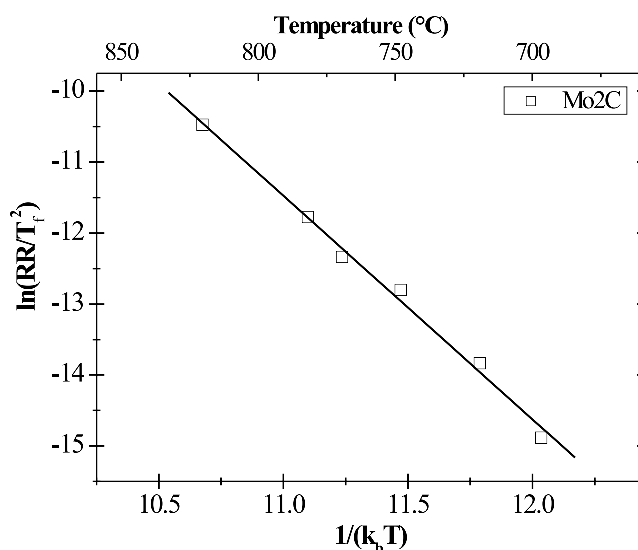

Figure 8.8: *Kissinger plot for the solid-state formation of Mo_2C, from a Mo-C sample with 30nm C capping layer.*

For the determination of the activation energy for Mo_2C formation, *in situ* XRD measurements were performed at 0.3, 1, 3, 5, 9 and $35°C/s$. For this the (100) and (101) peaks of the Mo_2C phase were used, and the Kissinger plot (figure 8.8) gave an activation energy of $E_a = 3.15 \pm 0.23\ eV$ ($R = 0.9968$).

Values reported for C diffusion in Mo_2C range from $3.06eV$ [24] to $3.60eV$ [25] in different temperature ranges. Warnes and Simkovich [26] reported a much higher activation energy of $4.79eV$, while Mikhailov *et al.* [4] found a lower value of $1.9 \pm 0.4\ eV$. Our value is in the same range as reported by the first group of researchers.

8.4.6 Hf-C:

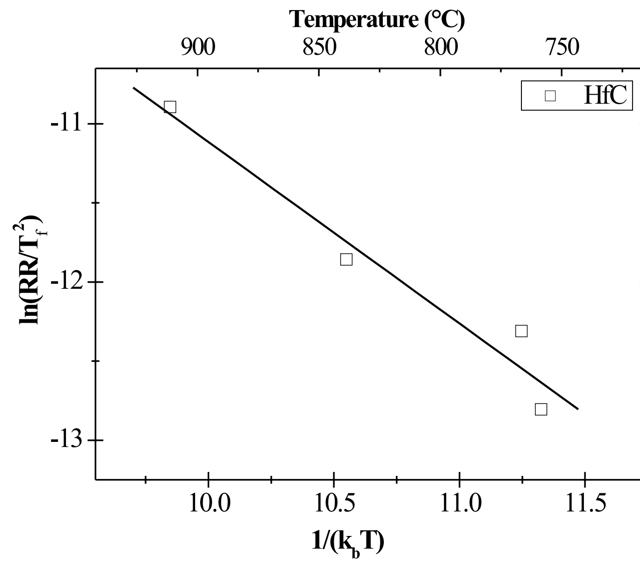

Figure 8.9: *Kissinger plot for the solid-state formation of HfC, from a Hf-C sample with 30nm C capping layer.*

Figure 8.9 shows the Kissinger plot for the Hf-C system. The HfC (111) and (200) peaks at $2\theta \approx 39^{\circ}$ and $\approx 45^{\circ}$, respectively, were monitored during the *in situ* XRD experiments at heating rate of 3, 5, 9 and $27^{\circ}C/s$. The activation energy for this system is $E_a = 2.05 \pm 0.19\ eV$ ($R = 0.9749$).

8.5 Summary

TABLE 8.1 summarizes the results for the activation energies of the different carbide phases. In the last column the range of composition is listed, more exactly the difference in x, which was already listed in table 7.20 (see Chapter 7, section 7.12, page 109).

Table 8.1: *Results for the activation energies of the various carbide phases, formed through a solid-state reaction of 30nm metal with carbon. All samples had a 30nm C capping layer. The activation energy was calculated from in situ XRD measurements at different heating rates by a Kissinger method. The range of composition (range of comp'n) was estimated from the binary phase diagram.*

Carbide Phase	E_a (eV)	Range of Comp'n
NbC	4.08 ± 0.37	0.26
Fe_3C	4.05 ± 0.83	0
W_2C	3.74 ± 0.29	0.09
WC	3.23 ± 0.29	0
Mo_2C	3.15 ± 0.23	0.03
Nb_2C	3.01 ± 0.36	0.01
VC	2.65 ± 0.38	0.22
HfC	2.05 ± 0.19	0.37
TiC	1.45 ± 0.81	0.28

Looking at the range of composition and the activation energies for the different carbide phases, one would intuitively try to correlate both. One would expect that C-atoms will move more easily through a layer with more vacancies, which would explain the lower activation energy. Figure 8.10 shows the activation energies of the different carbide phases versus the compositional range. The linear fit (dashed line) is not very convincing.

Many authors (e.g. [3, 8, 22]) pose that the activation energy for diffusion is independent of the composition. Figure 8.11 illustrates this for the NbC_x phase at two different compositions. The slope of the two lines in the plot stays the same, independent of the concentration. The intrinsic diffusivity (the diffusion coefficient) of carbon in the carbide phase, however, is highly sensitive to composition, decreasing exponentially with mole fraction carbon.

Other researchers [19, 21, 23] have shown that at different carbon concentrations, different carbon diffusion mechanisms are active. The dominance of a particular mechanism is dependent on the composition, but also on the temperature range. Due to these different diffusion mechanisms, a variation in the activation energy may occur.

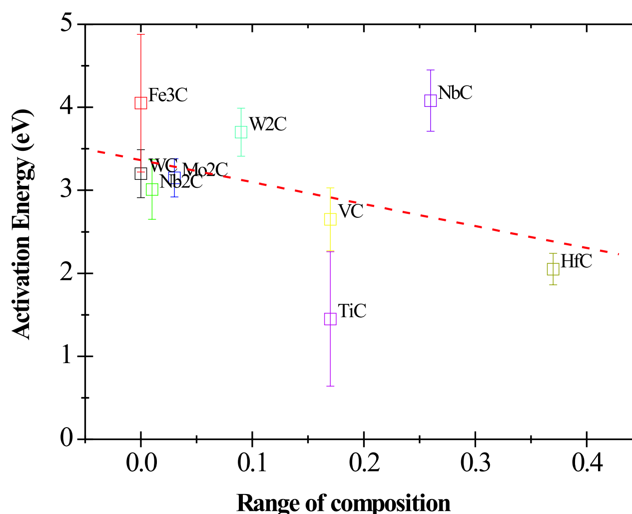

Figure 8.10: *The activation energies versus the range of composition for the different carbide phases. The dashed line is a linear fit to this data.*

According to Yu and Davis [23], three paths for C diffusion are most probable:

- the *O-O mechanism*, where the C atom jumps along the <110> direction, directly into a neighbouring vacant octahedral site.
- the *O-T-O mechanism*, where the carbon atom jumps to a vacant octahedral site in the <111> direction by a two-step process. First, a shorter <111> jump to an unoccupied tetrahedral site on the Nb sublattice takes place, followed by an immediate <111> jump to a vacant octahedral site (i.e. a vacant site on the C sublattice).
- the *transient divacancy mechanism*, where the C atom jumps to the vacant octahedral site by way of a normally occupied metal vacancy, which has momentarily become associated with the carbon vacancy.

In their research they found a different activation energy for single crystals of $NbC_{0.868}$ ($E_a = 4.35\ eV$) and $NbC_{0.834}$ ($E_a = 4.55\ eV$), compared to the activation energy for $NbC_{0.766}$ ($E_a = 3.30\ eV$). They attributed this difference to the presence of a different diffusion mechanism at different carbon concentrations. For the mechanisms above, they argue that a large lattice strain or accommodating movement of two metal atoms is required for the O-O mechanism. From consideration of the relative volumes of the C and metal atoms, it is obvious that the energy of the motion component in the activation energy in the transient divacancy mechanism will be much less than in the other two mechanisms, because in the latter two, the C atom has to forcefully migrate between Nb atoms. Therefore, it is concluded from the arguments

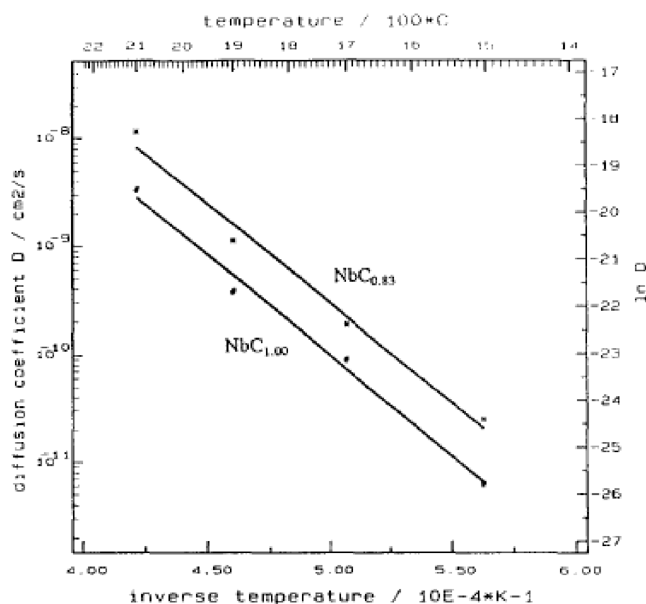

Figure 8.11: *Arrhenius dependencies of the carbon diffusion coefficients at the highest and lowest concentrations in NbC_x obtained from carbon profiles. The activation energy is independent of the concentration. Reproduction from [22].*

above that the energies of C migration in the various mechanisms decrease in the order (O-O) > (O-T-O) > divacancy. As they found the lowest activation energy for $NbC_{0.766}$, the logical assignments are the divacancy diffusion path for $NbC_{0.766}$, and the (O-T-O) path for the higher carbon concentrations.

For an explanation on the change of diffusion path, they consider the changes in electronic charge densities in the vicinity of the proposed avenues of transport. Yu and Davis cite work of Chadi and Cohen [27] which theoretically showed that the charge densities in NbC change, when going from NbC_1 to $NbC_{0.75}$. Namely, the number of valence electrons is reduced from 9 to 8, and secondly, the magnitude of the charge in the peak of the d_{xy} component of the d states becomes nearly zero in the latter material. Because of the extension of the d_{xy} electron orbitals from the neighbouring Nb atoms into the metal vacancy, the C atoms diffusing through the metal vacancy would have a barrier unless the electron density in the d_{xy} peak were close to zero. Thus the feasibility of the transient divacancy mechanism is enhanced as the C/Nb ratio decreases to a value close to 0.75. Also, from charge density calculations for the electron distribution, the minimum disturbance in the charge distribution of the NbC_1 crystal is along the <111> direction, i.e. the (O-T-O) path.

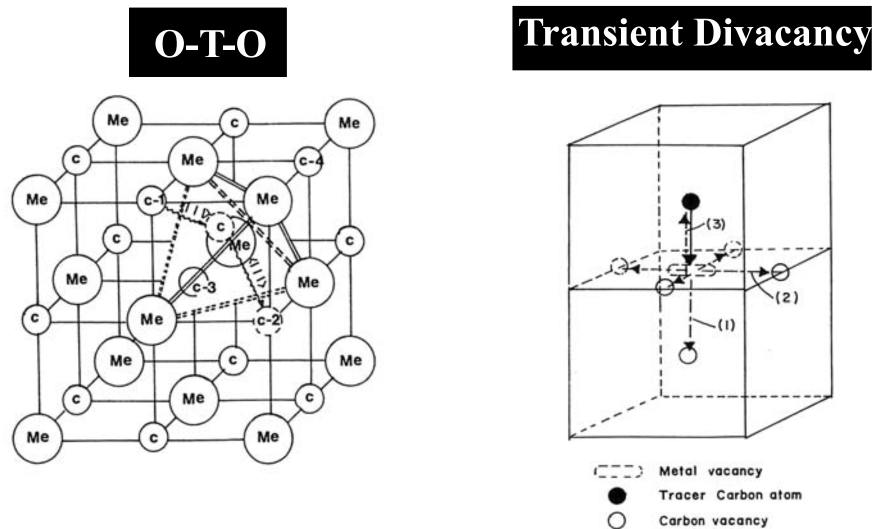

Figure 8.12: *Schematic illustrations of the O-T-O diffusion path (left) and the transient divancany mechanism (right) (reproduction from [23]). In the O-T-O mechanism, the carbon atom moves along the <111> direction, via an unoccupied tetrahedral site to the vacant octahedral site. In the transient divacancy mechanism, the carbon atom moves directly to an adjacent C vacancy whenever the latter becomes a nearest neighbour of a metal vacancy.*

As a support to their choice of mechanism they point out that the Nb vacancy formation energy determined by Storms ($2.62\ eV$) is similar to their activation energy for diffusion in $NbC_{0.766}$: $3.3\ eV$. They attribute the difference to a small migration energy term.

Summarizing, as the carbon concentration increases, the character of bonding in the material changes in such a manner as to cause the Nb d-orbitals to interfere with motion of carbon atoms through Nb vacancies. Therefore, the diffusion path changes from the divacancy mechanism to the (O-T-O) path.

Overviewing our results for the activation energies, we see that the results for TiC, HfC, VC, Nb_2C, Mo_2C and WC, are in the same range of the results of Yu and Davis [23], that were correlated to the *O-T-O mechanism*, while the other results (W_2C, Fe_3C, and NbC) tend to the *transient divacancy mechanism*. For a good correlation to their results, one would have to look at the charge densities of the different compounds, in order to get an idea of the most favoured diffusion path. The classification we give here, is only a possible part of the explanation, because other effects might play an important role.

Influences like grain boundary diffusion, probably play a very important role here in the diffusion. Barzilai *et al.* [7] wrote that the activation energy values for carbon diffusion in thin layers differ greatly from those obtained for bulk materials, and they address this difference in values to the micro-porosity of the film. Isobe *et al.* [5] also found a difference in the diffusion coefficient and also a lower activation energy for carbon diffusion in a coating, compared to bulk material. They state that grain boundary diffusion of carbon plays an important role in the carbide layer growth behaviour. And Guarnieri *et al.* [21] even conclude that at $1500°C$ for the Nb-C system, a shift occurs from a process dominated by lattice diffusion to one dominated by grain boundary diffusion or interface diffusion.

From the work of Yeh *et al.* [6] and Hatano *et al.* [28], one can conclude that grain boundaries and dislocations play an important role in the growth of carbides. Mikhailov *et al.* [4] also state that defects in a thin carbide film could play the role of traps, trapping the species diffusing (i.e. carbon) through the carbide layer.

The work of Buhsmer *et al.* [16] revealed another surprising result. In their study of the self-diffusion of carbon in tungsten carbide, they found two layers with a different diffusion path. A top layer (about $1\mu m$ into the bulk WC sample) had a bulk diffusion mechanism, with an anomalous slow rate. They attributed this layer to the surface oxidation. Beneath the surface layer, grain boundary diffusion was predominant. Relating the influence of impurities (like the oxygen in the surface layer, but also nitrogen or other metals), Matzke [19] writes that the defect concentrations are often impurity-controlled and that diffusion is governed by impurity-defect interactions.

Therefore, more experimental research should be done to determine the activation energies for the carbide phases, using different techniques, different parameters and different sample setups. This should be complemented by theoretical calculations for the different models of diffusion.

Bibliography

[1] C. Detavernier. *Fundamental study of nucleation and epitaxial growth of CoSi2*. Ph.d. thesis, Ghent University, 2001.

[2] X. L. Peng and T. W. Clyne. *Thin Solid Films*, 293(1-2):261, 1997.

[3] F. J. J. Vanloo, W. Wakelkamp, G. F. Bastin, and R. Metselaar. *Solid State Ion.*, 32-3:824, 1989.

[4] S. N. Mikhailov, D. Ariosa, J. Weber, Y. Baer, W. Hanni, X. M. Tang, and P. Alers. *Diam. Relat. Mat.*, 4(9):1137, 1995.

[5] Y. Isobe, P. Son, and M. Miyake. *J. Less-Common Met.*, 147(2):261, 1989.

[6] J. J. Yeh, R. L. Pfeffer, M. W. Cole, M. Ohring, and J. E. Yehoda. *Diam. Relat. Mat.*, 5(10):1195, 1996.

[7] S. Barzilai, A. Raveh, and N. Frage. *Vacuum*, 79(3-4):171, 2005.

[8] J. Woodford and Y. A. Chang. *Metall. Mater. Trans. A-Phys. Metall. Mater. Sci.*, 29(11):2717, 1998.

[9] M. Pitter, M. B. Hugenschmidt, and R. J. Behm. *Appl. Phys. Lett.*, 68(18):2508, 1996.

[10] J. S. Chen, E. Kolawa, M. A. Nicolet, and F. S. Pool. *Thin Solid Films*, 236(1-2):72, 1993.

[11] Y. F. Zhu, L. Wang, W. Q. Yao, and L. L. Cao. *Appl. Surf. Sci.*, 171(1-2):143, 2001.

[12] R.J. Fries, J.E. Cummings, C.G. Hoffman, and S.A. Daily. *Nucl. Sc. Abstr.*, 22(18):38622, 1967.

[13] E. G. Colgan and F. M. dHeurle. *J. Appl. Phys.*, 79(8):4087, 1996.

[14] E. J. Mittemeijer, A. Vangent, and P. J. Vanderschaaf. *Metall. Trans. A*, 17(8):1441, 1986.

[15] E. J. Mittemeijer, L. Cheng, P. J. Vanderschaaf, C. M. Brakman, and B. M. Korevaar. *Metall. Trans. A*, 19(4):925, 1988.

[16] C. P. Buhsmer and P. H. Crayton. *J. Mat. Sc.*, 6(7):981, 1971.

[17] S. Sarian. *J. Appl. Phys.*, 39(7):3305, 1968.

[18] S. Sarian. *J. Appl. Phys.*, 40(9):3515, 1969.

[19] H. Matzke. *Solid State Ion.*, 12(MAR):25, 1984.

[20] S. Barzilai, N. Frage, and A. Raveh. *Surf. Coat. Tech.*, 200(14-15):4646, 2006.

[21] C. R. Guarnieri, F. M. Dheurle, J. J. Cuomo, and S. J. Whitehair. *Appl. Surf. Sci.*, 53:115, 1991.

[22] W. Lengauer. *J. Alloy. Compd.*, 229(1):80, 1995.

[23] B. B. Yu and R. F. Davis. *J. Phys. Chem. Solids*, 40(12):997, 1979.

[24] C. J. Rosa. *Metall. Trans. A*, 14(2):199, 1983.

[25] G.V. Samsonov and A.P. Epik. *ZB. PR. Inst. Teploenerg. Akad. Nauk Ukr. R.S.R.*, 26:67, 1964.

[26] B. M. Warnes and G. Simkovich. *J. Less-Common Met.*, 106(2):241, 1985.

[27] D. J. Chadi and M. L. Cohen. *Phys. Rev. B*, 10(2):496, 1974.

[28] Y. Hatano, M. Takamori, K. Nogita, K. Matsuda, S. Ikeno, and K. Watanabe. *J. Nucl. Mater.*, 337-39(1-3):902, 2005.

Part III

Carbides as contacts to carbon-containing advanced semiconductors

Chapter 9

Carbides as contacts to C-containing advanced semiconductors

FOR certain applications, carbon-containing semiconductors may potentially replace the current silicon technology. SiC is already used in high-power and high-frequency applications [1, 2]. Contact formation on SiC, however, involves both carbide and silicide formation [3, 4]. $Si_{1-x}C_x$ as well as $Si_{1-x-y}Ge_xC_y$ are mentioned [5] for future devices, and of particular concern is how C behaves during annealing (*e.g.* carbide formation) and how it affects the contact integrity in terms of interface morphology and contact resistivity.

Carbon nanotubes (CNTs) and diamond are more advanced carbon-containing semiconductors. These materials have very promising properties, but are still in a highly experimental phase. We will briefly give some properties of these materials and summarize some of the relevant published work. Furthermore, some experimental results are presented as an illustration of the possibility of using carbides as contacts for these carbon-containing semiconductors.

9.1 Carbon Nanotubes (CNTs)

IN the early 1960s, a whole range of graphite-based materials were developed, which found broad industrial application. A good (present-day) example for this, is the nanostructured carbon anode which is used in lithium ion rechargeable batteries. After Russian scientists in 1973 calculated that a C_{60} molecule would be stable, the ***Buckminsterfullerene*** was synthesized in 1985 by Harold Kroto, Richard Smalley and Robert Curl [6], winners of the 1996-Nobel prize of Chemistry. In 1991, another form of carbon comes into play: the carbon nanotube (CNT) [7]. Ever since this discovery of the multi-walled CNTs (MWCNTs) and later the single-walled CNTs (SWCNTs) [8, 9], research on this interesting material has been booming.

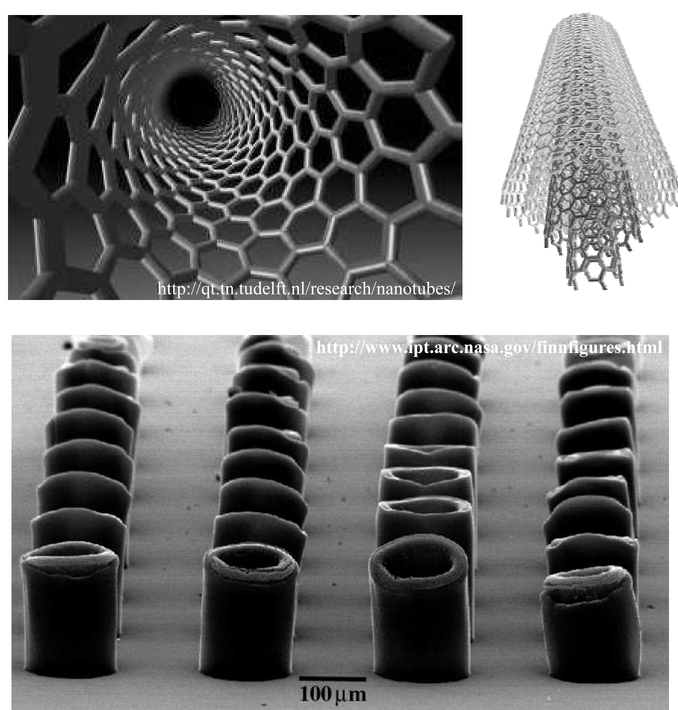

Figure 9.1: *Illustrations of carbon nanotubes (top) and a SEM image of an array of aligned carbon nanotubes (bottom).*

There are three most commonly used methods to produce carbon nanotubes [10, 11]: arc discharge, laser ablation, and chemical vapour deposition. In arc discharge, a carbon vapour is created by an arc discharge between two carbon electrodes with or without catalyst. Nanotubes self-assemble from this carbon vapour. The multiwall nanotubes reported by Iijima [7] in 1991 were produced by an arc-discharge method. In the laser ablation technique, a high-power laser beam impinges on a volume of carbon -containing feedstock gas (methane or carbon monoxide). At the moment, laser ablation produces a small amount of clean nanotubes, whereas arc

discharge methods generally produce large quantities of impure material. The evaporation temperature involved in both processes is close to the melting temperature of graphite, $3000°C$ to $4000°C$. The CVD method is based on the decomposition of carbon-containing gases on metal catalysts at reaction temperatures below $1000°C$. This method is relatively easy to scale up, which favours commercial production.

Some of the special properties of CNTs are [12]:

- *Mechanical Strength.* CNTs have a very large Young's modulus in their axial direction, typically of the order of 1.0 to $1.3TPa$ (the metal with the biggest Young's modulus is Ir with $0.538TPa$). This is easily understood if one knows that graphite has a high Young's modulus, and one can visualize CNTs as 'rolled-up graphite sheets'. They combine this strength with a high flexibility (i.e. easy twisting, bending,.. of the CNT), without plastic deformation. This cannot be found in any other graphitic structure. These mechanical properties imply many possible applications and recently, a super-hard bulk material consisting solely of nanotubes has been created, suggesting that macroscopic structures consisting exclusively of nanotubes might be possible [10].

- *Chemical Reactivity.* The CNTs have various peculiar chemical properties, and chemical modification of either sidewalls or end caps was shown to be possible [13]. Researchers find it clear that the nascent field of nanotube chemistry will rival that of the fullerenes [14]. One of the most special features is the possibility to fill the CNT with a gas (*e.g.* H_2 [15, 16]) and even with liquids and solids [17].

- *Electrical Conductivity.* Depending on their atomic structure (chirality and diameter), carbon nanotubes with a small diameter are either semi-conducting or metallic [18]. In theory, metallic nanotubes can have an electrical current density more than 1,000 times greater than metals such as silver and copper.

The unique combination of properties of CNTs make them very attractive for numerous applications, and we will focus on a few electronic ones. In order to be suitable as a ***field emitter***, a material should have a low threshold emission field and a large stability at high current density. Furthermore, an ideal emitter is required to have a nanometre size diameter, a good structural integrity, a high electrical conductivity and a large chemical stability. CNTs possess all these properties. A few applications of field emitting devices are flat panel displays (see figure 9.2), lamps, electron guns for electron microscopes, and microwave amplifiers. A flat panel display *e.g.* works by applying a potential between a CNT$-$coated surface and an anode. Due to the small radius of the nanofiber tip and the length of the nanofiber, this produces high local fields that cause electrons to tunnel from the nanotube tip into the vacuum. Electric fields direct the field-emitted electrons toward the anode, where a phosphor produces light for the flat panel display application.

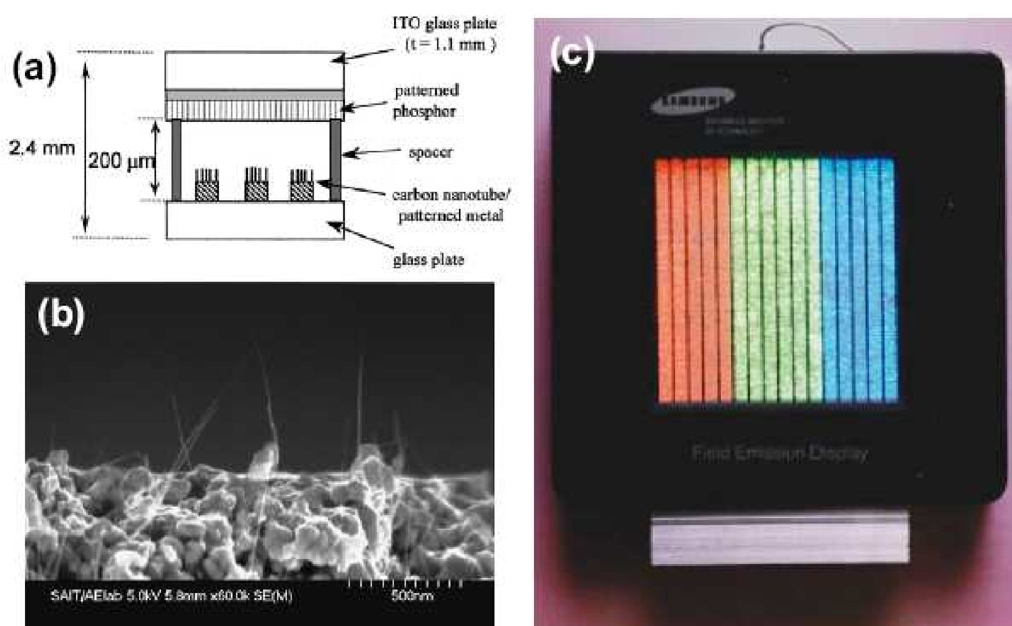

Figure 9.2: *(a) Picture representing the set-up of a field emission display. CNTs are deposited on a patterned metal substrate. Field emitted electrons hit the phosphor screen and cause light emission in that colour that depends on the chemical compound of the phosphor screen. (b) SEM image of nanotube bundles projecting from the metal electrode. (c) A sealed CNT field emission display emitting light in three different colours. The dimension of the display is* $11.43cm.$ *(from Choi et al. [19])*

The transistor is probably the most-used electronic component, and ever since Tans *et al.* [20] demonstrated the possibility for modulating the conductance through a carbon nanotube by a gate electrode, several groups have fabricated field effect transistors (FETs) device structures [21, 22]. In a 'standard' CNT-FET, the carbon nanotube acts as a channel, connecting two metal electrodes. The channel conductance is modulated by a third gate electrode. Several different types of CNT-FETs have been proposed and figure 9.3 shows two possibilities.

There are, however, several issues which need to be resolved before CNT-FETs will be found in everyday life. One of the problems, is the positioning of the CNTs. Currently, either randomly distributed CNTs are individually contacted by metal pads (using *e.g.* e-beam lithography or focussed ion beam (FIB) deposition), or the CNTs are individually positioned on the metal pads, using an AFM. Both techniques are unsuitable for scaling-up. IBM researchers [23] have demonstrated a position-selected growth of CNTs, and although the technique is far from perfect, it is a big step towards large-scale integration of the CNTs in electronics.

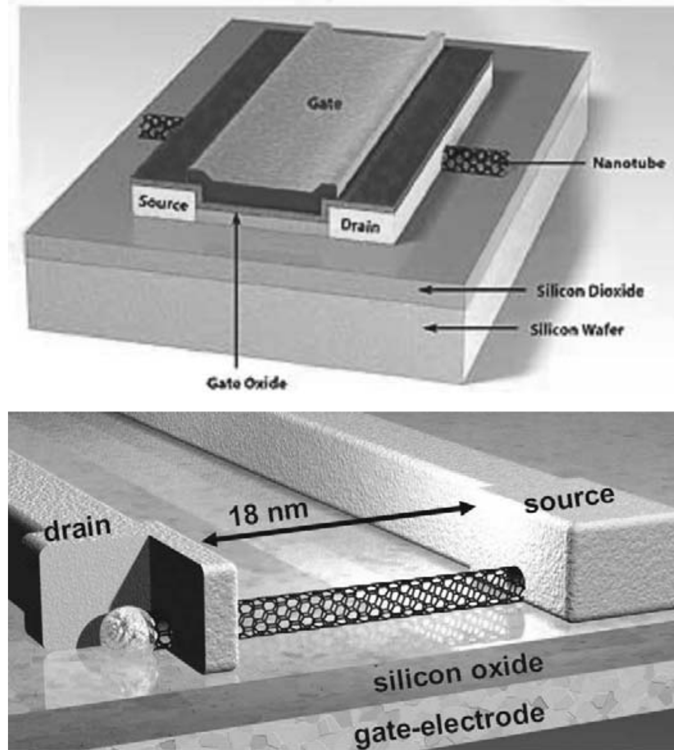

Figure 9.3: *Two illustrations of a possible CNT-FET. The top is a so-called top-gate FET (image from IBM), the bottom one is a bottom-gate FET (image from Infineon).*

Another problem is caused by the dual electric nature of the CNTs (they can be either metallic or semiconducting, depending on their structure). Obviously, a transistor will not work when it is built using a metallic CNT as base material. Collins *et al.* [24] demonstrated that it is possible to selectively peel the outer layers from a multi-walled CNT until a nanotube cylinder with the desired electronic properties is obtained. The same can be done for a bundle of single-walled CNTs, *e.g.* destroying the metallic CNTs and leaving the semiconducting CNTs alone. Recently, researchers in Texas [25] succeeded in sorting carbon nanotubes by their size AND by their electrical properties. This will probably make them easier to use in everything from nano-electronics to tear-proof textiles.

Research towards CNT-FETs aims to replace the source-drain channel structure with a nanotube. A more radical approach is to construct entire electronic circuits from interconnected nanotubes. Because the electronic properties depend on the structure of the CNT, it should be possible to produce a diode, for example, by grafting a metallic nanotube to a semiconducting nanotube. Yao *et al.* [26] have shown the possibility of an intrinsic metal-semiconductor CNT, but the CNT was not rationally produced. Rather, it was recognized in a normal nanotube sample by its kinked structure, which

was caused by the helicity change. The development of rational synthesis routes to multiply branched and interconnected low-defect nanotubes with targeted helicity would be another revolutionary advance for nanoelectronics.

Carbides and Carbon Nanotubes:

WHERE do carbides come into play with CNTs? As said before, integrating CNTs in the current IC production methods is probably the most promising way for their acceptance in microelectronics. Carbides are good candidates to contact CNTs, because they can be applied using the current method of contact fabrication (SALICIDE). As shown in chapter 7, Ti, V, Cr, Fe, Nb, Mo, Hf, Ta, and W form carbides through a solid-state reaction with carbon. Their carbide phases can be expected to form stable contacts to CNTs.

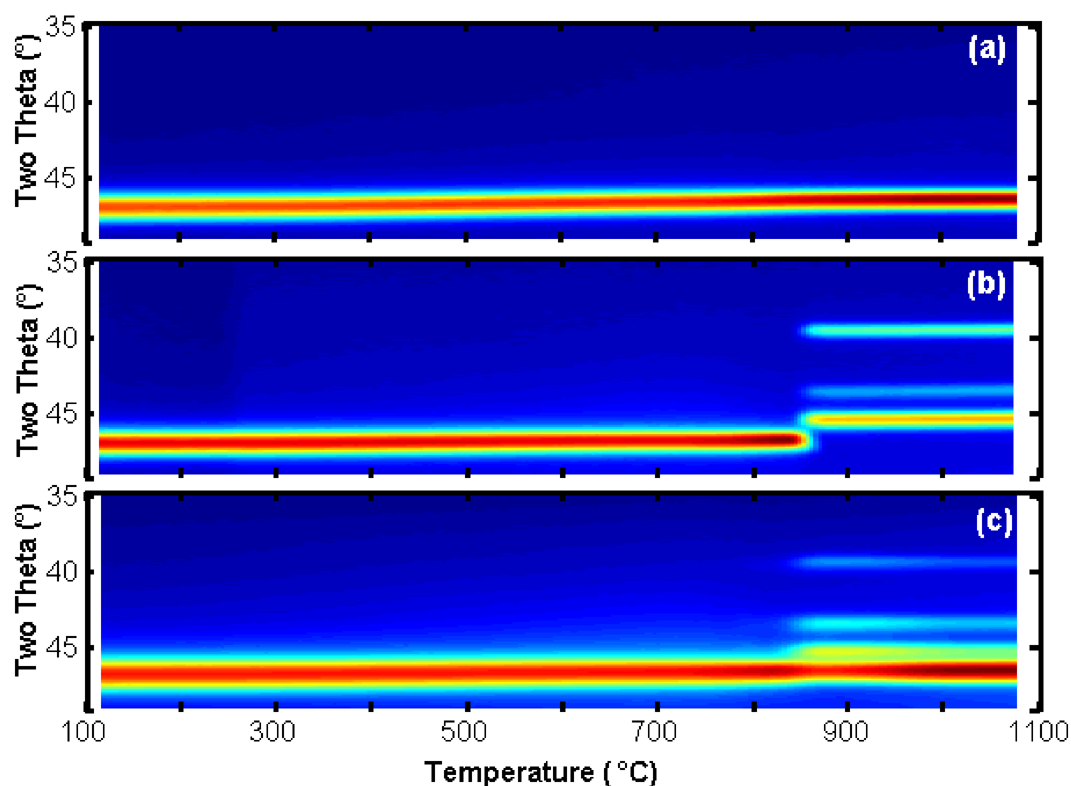

Figure 9.4: *Three in situ XRD measurements, ramped at $3°C/s$. (a) 30nm Mo on SiO_2, (b) 30nm Mo on 200nm C on SiO_2, 30nm Mo on dispersed carbon nanotubes on SiO_2.*

Dai *et al.* [27] were (to our knowledge) the first to combine carbide formation and CNTs. In their work, CNTs are reacted with volatile oxide and/or halide species to prepare solid carbide nanoscale rods of TiC, NbC, Fe_3C, SiC and BC_x with diameters between 2 and $30nm$. However, this method has not been used for fabricating nanojunctions because of the difficulty of controlling the reaction region along the carbon nanotube. Zhang *et al.* [28] describe a method for fabricating SWCNT/carbide heterostructures with well-defined nanometer-scale interfaces. Through a solid-state reaction of SWCNTs and Si, Ti or Nb, they formed carbide end-bonded contacts to CNTs. Lee *et al.* [29] formed low-resistance TiC contacts to MWCNTs and Martel *et al.* [30] did the same for SWCNTs and created an ambipolar CNTFET (n- or p-type action, depending on the gate voltage). They point out that carbide contact formation improves the contact resistance and stability. But as Kreupl [31] mentions: one of the problems that needs to be solved, is to contact the CNTs with metals to yield reproducible low Ohmic contact resistances.

To illustrate **the possibility of forming carbide contacts to CNTs**, using a solid-state reaction, we present an *in situ* XRD result. Figure 9.4 shows three *in situ* XRD measurements, where the samples were heated at $3°C/s$ from $100°C$ to $1100°C$. The different sample setups are (a) $30nm\ Mo$ on SiO_2, (b) $30nm\ Mo$ on $200nm$ C on SiO_2, and (c) $30nm\ Mo$ on dispersed CNTs on SiO_2. Figure 9.4(a) and (b) show that Mo does not interact with SiO_2 and that it forms Mo_2C when reacted with C, respectively. Figure 9.4(c) can be regarded as a combination of the two previous reactions. The Mo layer interacts with the CNT to form Mo_2C, while the excess Mo remains unreacted (the $Mo(110)$ peak is still present after Mo_2C formation). If one would use patterning to cover the CNTs only partially with Mo, carbide contacts could be formed which are end-bonded to the CNTs.

9.2 Chemical Vapour Deposited (CVD) Diamond

DIAMOND has always been a desire of people, because of its hardness and high dispersion of light (and of course, its rareness). But it took until 1796 to recognize that diamond is an allotrope form of carbon. This founded the belief that diamond could be man-made, and in the 1950s Swedish and American scientists* synthesized diamond. Pressures above $5.5GPa$ and temperatures above $1400°C$ are needed, plus molten iron to facilitate the change from graphite to diamond. Worth mentioning in regard of our work, is that the discovery of tungsten carbide in the 1930s was a major step in the right direction, because this material could achieve the pressure containment needed for growing diamond.

Figure 9.5: *A synthetic diamond created by Apollo Diamond using a patented chemical vapour deposition process. It is 8mm wide by 2mm deep*†*.*

The original method of making synthetic diamond is still being used, because of its relatively low cost. The *high pressure and high temperature (HPHT)* reproduce the conditions that create natural diamond inside the Earth. There are however a few downsides to the possibility of usage for these HPHT-diamonds (the same as for natural diamonds). The shapes and sizes which can be obtained are limited. Secondly, since a solvent metal is used (usually Fe, Ni or Co) to lower the temperature needed for formation, metallic inclusions in the synthetic diamond are inevitable. Therefore,

*The Swedish team was led by Balthazar von Platen and they succeeded in making diamond in 1953 in Stockholm, but their success wasn't published. The American General Electric team claimed credit for the first reproducible transformation from graphite to diamond, on February 15, 1955.

†http://www.flickr.com/photos/jurvetson/156830367/

these diamonds are mainly used for mechanical and thermal applications, and not for more sophisticated applications and devices.

In 1962, the first successes using another method of creating diamond, *Chemical Vapour Deposition*, were reported [32]. In this technique, an alternating flow of thermally decomposed hydrocarbon gas and hydrogen, leads to a successful deposit of diamond under reduced pressure on a heated ($900°C$) natural diamond crystal. Nowadays, the production of CVD-diamond has become more common, and there are different ways of production available [33] (*e.g.* hot filament CVD, microwave plasma-enhanced CVD,...). CVD-diamond has very similar properties as natural diamond, but has the advantage that it can be deposited on various substrates, that it can be grown over large areas and that the properties of the diamond can be controlled. These are all necessary properties to be considered for application in microelectronics.

Diamond has quite some advantageous properties compared to silicon, for being used in microelectronics (see table 9.1). However, it's only since the last decade that CVD-diamond has become readily available. Before, all diamonds that could be used, were either very expensive or of poor quality.

Table 9.1: *Overview of some properties of a single crystal of diamond, compared with silicon. [34]*

Property		Diamond	Silicon
Thermal expansion	$(\times 10^{-6} K^{-1})$	1.1	2.6
Band Gap	(eV)	5.45 (indirect)	1.1 (indirect)
Carrier Mobility	$(cm^2 V^{-1} s^{-1})$		
Electron		2200	1500
Hole		1600	600
Breakdown Voltage	$(\times 10^5 V cm^{-1})$	100	3
Dielectric Constant		5.5	11.8
Resistivity	(Ωcm)	10^{13}	10^3
Thermal Conductivity	$(W cm^{-1} K^{-1})$	20	1.5
Hardness	(GPa)	98	9.8

CVD diamond has very attractive physical and electrical properties for electronic applications. The wide band gap, high breakdown voltage, high carrier mobility, radiation hardness, and high thermal conductivity make diamond a promising material for the fabrication of high-power, high-frequency and high-temperature devices. There has been considerable research on understanding CVD diamond material properties, fabrication processes and the physics of diamond-based devices. There are, however, still quite some obstacles to widespread the commercial use of CVD diamond in electronics. To our knowledge, the first experimental planar diamond transistor in a MESFET configuration was fabricated in 1989 by Shiomi *et al.* [35]. The first high-

temperature ($200°C$) and high-voltage ($100V$) operation of a polycrystalline diamond FET, was demonstrated by Tessmer *et al.* in 1993 [36]. It exhibited saturation of the drain-to-source current and modulation of the active channel conductance (as is expected for a good FET).

Most of the microelectronic realisations use p-type diamond, because there have been more problems in doping diamond to n-type. However in 1991, Okano *et al.* [37] already reported the formation of a $p-n$ junction diode made of semiconducting diamond films. Koizumi *et al.* succeeded in the realisation of a UV-LED based on a diamond $p-n$ junction [38].

Carbides and CVD diamond:

METALLIZATION of CVD diamond is essential for bonding integrated circuits (ICs) to the diamond and providing electrical interconnects between the ICs. A metal contact on diamond is required to take advantage of the excellent thermal and electrical properties of diamond. Therefore, the contact needs to be strongly adherent to diamond, stable at high temperatures, corrosion resistant, have a good electrical conductivity, have a strong adherence to dielectrics and be compatible with the assembly process. Carbides posses many of these properties and are therefore very good candidates to contact diamond. In general, carbides are strongly adherent to diamond, are stable at high temperatures, have a good corrosion resistance and a good electrical conductivity. As shown in chapter 7, most carbides can be formed using a solid-state reaction, which includes their compatibility with the assembly processes already used in IC manufacturing.

Formation of the contacts:

There are two schemes that have mostly been used for the metallization of diamond substrates. An adhesion layer of Cr or Ti, with an overlayer of either Au or $Au-Sn$ alloy. This system will fail at high temperatures, because of the intermixing of the two layers. The second method uses a diffusion barrier to separate the contacting layer and the overlayer. The latter, off course, requires some more complex deposition techniques.

Other researchers have already used carbide-forming metals to contact diamond and most of them noticed that a heat treatment of the metal-diamond contact reduces the contact resistivity [39–42]. Some of them evidenced the formation of a carbide at the interface and most of them were already mentioned in chapter 7 [43–48]. However, a systematic approach to the carbide formation was not done, and hopefully our work can be a big help for future research on the contact formation on diamond.

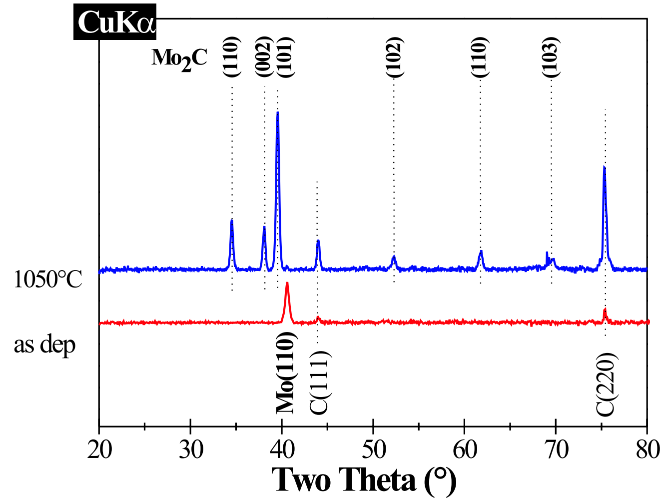

Figure 9.6: *Ex situ XRD measurements ($CuK\alpha$) of 30nm Mo layers with 30nm C capping layer on CVD diamond. The measurement in red is done on an as-deposited sample, the one in blue on a sample that was annealed to $1050°C$ at $3°C/s$ in a He-atmosphere.*

As an example, we deposited $30nm\ Mo$, with $30nm\ C$ capping layer, on CVD diamond and annealed the sample at $3°C/s$ to $1050°C$ in He-atmosphere. Figure 9.6 shows *ex situ* XRD measurements (using $CuK\alpha$ radiation) of an as-deposited sample (in red), and of a sample annealed to $1050°C$ (in blue). The different peaks of each phase have been marked on the figure. There are also two peaks of the diamond visible on the measurement ($C(111)$ and $C(220)$). From figure 9.6, one can easily see that the carbide phase, Mo_2C, has formed after annealing the sample. We did not find any differences from our previously obtained results on amorphous-C substrates. Unfortunately, *in situ* XRD measurements for this sample, were not available.

The results of another *ex situ* XRD experiment, using $30nm\ W$ with $30nm\ C$ capping layer on CVD diamond, is shown in figure 9.7(b). As a reference, we show the *in situ* XRD measurement on an amorphous-C susbtrate, in figure 9.7(a). The first two phases, $\beta - W$ and $\alpha - W$, have distinct peaks and are the phases that were expected from the *in situ* experiment. At $1020°C$, the *in situ* XRD measurement shows only peaks of the W_2C phase, while in the *ex situ* XRD measurement, the $\alpha - W(110)$ peak is still visible. At the highest annealing temperature ($1150°C$), the $\alpha - W(110)$ peak has disappeared and peaks of the WC phase are present alongside the peaks of W_2C.

Although the phase sequence remains the same for an amorphous C and a CVD diamond substrate layer, the formation temperatures of the different phases seems to have shifted to slightly higher temperatures. This might be due to the extra amount of energy needed to create mobile C-atoms out of the diamond layer. As we have

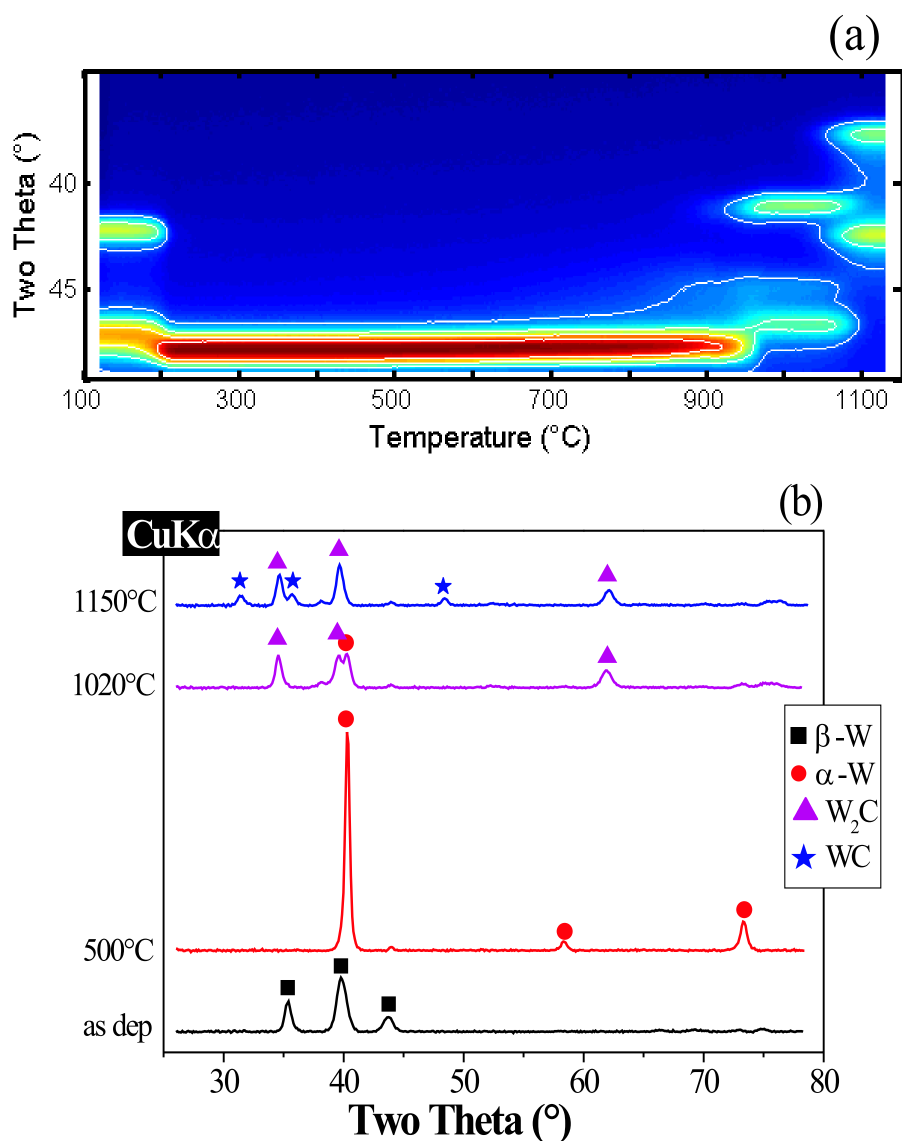

Figure 9.7: *(a) In situ XRD measurement of 30nm W layers with 30nm C capping layer on 200nm C on SiO_2; and (b) ex situ XRD measurements ($CuK\alpha$) of 30nm W layers with 30nm C capping layer on CVD diamond. The samples were annealed to the indicated temperatures at $3°C/s$ in a He-atmosphere. The peaks of the different phases in figure (b) have been marked.*

no *in situ* XRD measurements on CVD diamond substrates, we were not able to determine the formation temperature for the different phases on CVD diamond, but both experiments show that **the same phase formation occurs for the carbide solid-state formation on CVD diamond.**

Electrical behaviour of the contacts:

There are already a variety of studies on the electrical behaviour of metal contacts to CVD diamond [39, 41, 42, 44, 49–53], dealing with carbide-forming metals as well as non-interacting metals. From our previous obtained results, we selected Mo_2C as a good candidate for contacting C-containing semiconductors. Therefore, we deposited circular dots of $30nm$ Mo with $30nm$ C capping layer on B-doped CVD diamond (i.e. p-type). I/V characteristics were obtained between two contacts, and figure 9.8(a) shows two of them, one before annealing and one after (ramp)annealing the sample at $3°C/s$ to $1000°C$ in a He atmosphere. One clearly observes an Ohmic behaviour,

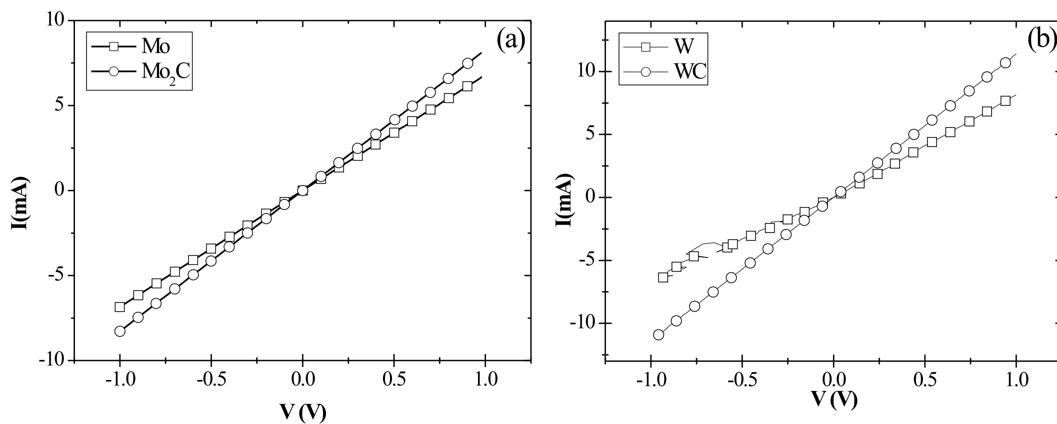

Figure 9.8: *(a) I/V characteristics of Mo and Mo_2C dots on a layer of CVD diamond. (b) I/V characteristics of W and WC dots on a layer of CVD diamond.*

with a (slightly) lower resistance for the annealed sample, were the Mo dots have been reacted to Mo_2C dots. This was expected, as Nakanishi *et al.* [52] observed similar behaviour, i.e. Ohmic behaviour for as-deposited Mo and for formed Mo_2C contacts and a lower (contact) resistance for the latter contacts. Figure 9.8(b) shows the same for W and WC contacts on CVD diamond. Contact resistances were not calculated from our results, due to the uncertainty on the thickness of the CVD-layer. Our results are shown for illustrating trends. Nakanishi *et al.* concluded from their research that Mo_2C contacts are extremely stable at high temperatures. Specific contact resistances of $\rho_C \approx 10^{-6}\Omega cm^2$ were measured for Mo_2C contacts on heavily doped ($N_A \geq 10^20 cm^{-3}$) diamond films.

Ohmic behaviour was also shown for other carbide-forming metals, like Ta, Ti and Cr [40, 54–56].

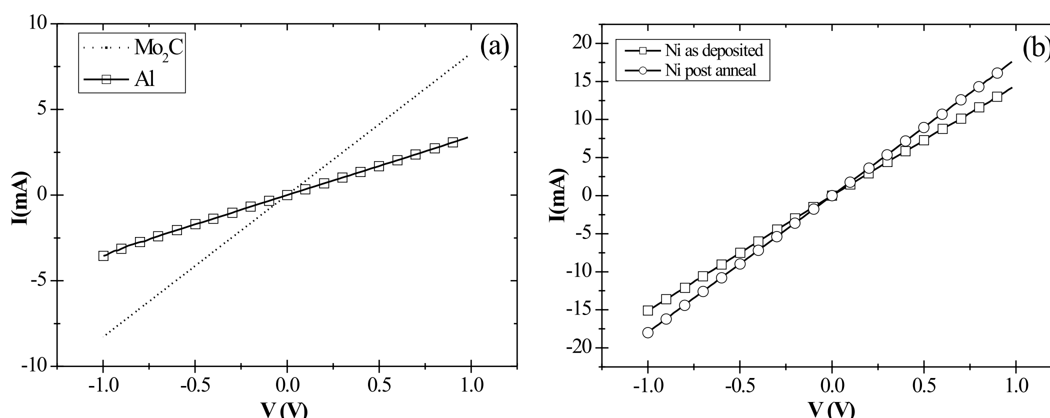

Figure 9.9: *(a) I/V characteristics of an Al dot on CVD diamond, with a Mo_2C dot as 'back-contact'. The dashed line is the I/V characteristic for two $Mo2C$ contacts, and is given as reference only. (b) I/V characteristics of Ni dots on CVD diamond, measured as deposited and after annealing to $1100°C$.*

Schottky contacts on p-type CVD diamond have also been reported: by depositing Au or Al on the diamond [49], by (thermally or reactively) growing the rare-earth carbide ErC_2 on diamond [53, 57], and even by depositing WC contacts [58]. As shown in figure 9.8(b), we obtained Ohmic behaviour for the WC contacts, in contradiction to the results of Liao *et al.*. Furthermore, figure 9.9(a) shows an I/V characteristic measured on an Al dot on CVD diamond, where Mo_2C contacts were made as second (or back-) contact, prior to the Al deposition. The characteristic is by no means rectifying, in contradiction to the results of Gildenblat *et al.* [49]. Humphreys *et al.* [59] showed rectifying characteristics for Ni contacts on p-type diamond, and therefore we deposited Ni dots onto the p-type CVD diamond layer. The I/V characteristics are shown in figure 9.9(b) and demonstrate (again) an Ohmic behaviour.

Tachibana *et al.* performed a study on the correlation of the electrical properties and the chemical nature of metal-diamond contacts [44, 50]. For this, they examined the behaviour of a non-carbide forming metal (Au) and of a carbide-forming metal (Ti) on polycrystalline diamond. The as-deposited Au contact exhibits rectifying characteristics, but when the diamond surface was sputter-cleaned prior to the Au deposition, the as-deposited Au formed Ohmic contacts. Due to the sputtering, a damaged surface layer, consisting of graphite and amorphous carbon, is present. Once the Au contacts are annealed, they again become rectifying, because the damaged layer is absorbed into the gold overlayer. For Ti they observed the same behaviour as for Au, namely rectifying for as-deposited samples on diamond,

and Ohmic on sputter-cleaned diamond. However, annealing the Ti contacts results for both diamond surfaces in carbide formation, with an Ohmic behaviour (even after post-deposition annealing of the sputter-cleaned sample). It is believed that the Ohmic behaviour results from the defect formation at and near the diamond surface due to either the presence of the graphitic layer or due to the carbide forming reaction. Moreover, the carbide layer acts as a diffusion barrier for the (electrically active) defects at the diamond surface. Zhu *et al.* [60] found a similar behaviour for $Au/n-Si$ and $PtSi/n-Si$ Schottky contacts. Ar ion bombardment of the Si substrate, prior to the contact fabrication, induced donor-like defects with relatively high densities near the Si surface, which led to a lowering of the Schottky barrier height. For the p-type diamond-substrates (used by Tachibana *et al.*), similar **acceptor-like defects** will be present, and are annealed out at higher temperatures.

According to Koide *et al.* [41, 61], the defect layer is due to the phase formation from metastable diamond to a stable conductive graphite layer, in the vicinity of the metal/diamond interface. In this view, Kiyota *et al.* [62] also concludes that the mechanism of barrier formation on as-grown diamond surfaces are drastically changed by oxidation. Moreover, they suggest that additional (i.e. not related to boron) acceptor centres are present in the as-grown film, which disappear after oxidation.

Regarding the rectifying contacts on CVD diamond films, they can be obtained (and/or improved) by growing an insulating and undoped diamond film on a previously boron-doped semiconducting film, or by thin interfacial insulating films (*e.g.* SiO_2) [51]. Furthermore, the previously mentioned Schottky characteristics for WC on diamond were obtained on an oxidized p-diamond layer [58].

From all the above, it is concluded that **the crystal structure at the metal/diamond interface significantly influences the electrical properties**. We refer to the **bond-polarization theory** (see chapter 4), where a similar conclusion is made. To get a good comprehension of the electrical behaviour of the contacts formed on CVD diamond, one should have a good understanding of the metal-diamond interface, and thus first of the diamond surface.

Bibliography

[1] J. A. Cooper and A. Agarwal. *Proc. IEEE*, 90(6):956, 2002.

[2] K. C. Chang, L. M. Porter, J. Bentley, C. Y. Lu, and J. Cooper. *J. Appl. Phys.*, 95(12):8252, 2004.

[3] T. C. Chou, A. Joshi, and J. Wadsworth. *J. Vac. Sci. Technol. A-Vac. Surf. Films*, 9(3):1525, 1991.

[4] J. S. Chen, E. Kolawa, M. A. Nicolet, R. P. Ruiz, L. Baud, C. Jaussaud, and R. Madar. *J. Appl. Phys.*, 76(4):2169, 1994.

[5] S. L. Zhang and M. Ostling. *Crit. Rev. Solid State Mat. Sci.*, 28(1):1, 2003.

[6] H. W. Kroto, J. R. Heath, S. C. Obrien, R. F. Curl, and R. E. Smalley. *Nature*, 318(6042):162, 1985.

[7] S. Iijima. *Nature*, 354(6348):56, 1991.

[8] S. Iijima and T. Ichihashi. *Nature*, 363(6430):603, 1993.

[9] D. S. Bethune, C. H. Kiang, M. S. Devries, G. Gorman, R. Savoy, J. Vazquez, and R. Beyers. *Nature*, 363(6430):605, 1993.

[10] R. R. Schlittler, J. W. Seo, J. K. Gimzewski, C. Durkan, M. S. M. Saifullah, and M. E. Welland. *Science*, 292(5519):1136, 2001.

[11] O. A. Shenderova, V. V. Zhirnov, and D. W. Brenner. *Crit. Rev. Solid State Mat. Sci.*, 27(3-4):227, 2002.

[12] S. B. Sinnott and R. Andrews. *Crit. Rev. Solid State Mat. Sci.*, 26(3):145, 2001.

[13] S. S. Wong, E. Joselevich, A. T. Woolley, C. L. Cheung, and C. M. Lieber. *Nature*, 394(6688):52, 1998.

[14] S. Niyogi, M. A. Hamon, H. Hu, B. Zhao, P. Bhowmik, R. Sen, M. E. Itkis, and R. C. Haddon. *Acc. Chem. Res.*, 35(12):1105, 2002.

[15] A. C. Dillon, K. M. Jones, T. A. Bekkedahl, C. H. Kiang, D. S. Bethune, and M. J. Heben. *Nature*, 386(6623):377, 1997.

[16] C. Liu, Y. Y. Fan, M. Liu, H. T. Cong, H. M. Cheng, and M. S. Dresselhaus. *Science*, 286(5442):1127, 1999.

[17] T. W. Ebbesen. *J. Phys. Chem. Solids*, 57(6-8):951, 1996.

[18] T. W. Ebbesen, H. J. Lezec, H. Hiura, J. W. Bennett, H. F. Ghaemi, and T. Thio. *Nature*, 382(6586):54, 1996.

[19] W. B. Choi, D. S. Chung, J. H. Kang, H. Y. Kim, Y. W. Jin, I. T. Han, Y. H. Lee, J. E. Jung, N. S. Lee, G. S. Park, and J. M. Kim. *Appl. Phys. Lett.*, 75(20):3129, 1999.

[20] S. J. Tans, A. R. M. Verschueren, and C. Dekker. *Nature*, 393(6680):49, 1998.

[21] A. Bachtold, P. Hadley, T. Nakanishi, and C. Dekker. *Science*, 294(5545):1317, 2001.

[22] P. Avouris. *Accounts Chem. Res.*, 35(12):1026, 2002.

[23] C. Klinke, J. B. Hannon, A. Afzali, and P. Avouris. *Nano Lett.*, 6(5):906, 2006.

[24] P. C. Collins, M. S. Arnold, and P. Avouris. 292(5517):706, 2001.

[25] NewScientist.com. "gadget sorts nanotubes by size", 27 June 2006.

[26] Z. Yao, H. W. C. Postma, L. Balents, and C. Dekker. *Nature*, 402(6759):273, 1999.

[27] H. J. Dai, E. W. Wong, Y. Z. Lu, S. S. Fan, and C. M. Lieber. *Nature*, 375(6534):769, 1995.

[28] Y. Zhang, T. Ichihashi, E. Landree, F. Nihey, and S. Iijima. *Science*, 285(5434):1719, 1999.

[29] J. O. Lee, C. Park, J. J. Kim, J. Kim, J. W. Park, and K. H. Yoo. *J. Phys. D-Appl. Phys.*, 33(16):1953, 2000.

[30] R. Martel, V. Derycke, C. Lavoie, J. Appenzeller, K. K. Chan, J. Tersoff, and P. Avouris. *Phys. Rev. Lett.*, 87(25), 2001.

[31] F. Kreupl, A. Graham, and W. Honlein. *Solid State Technol.*, 45(4):S9, 2002.

[32] W.G. Eversole. Synthesis of diamond, April 17 1962 1962.

[33] T. A. Railkar, W. P. Kang, H. Windischmann, A. P. Malshe, H. A. Naseem, J. L. Davidson, and W. D. Brown. *Crit. Rev. Solid State Mat. Sci.*, 25(3):163, 2000.

[34] K. Haenen. *Opto-electronic study of P-doped n-type and H-doped p-type CVD diamond films*. Ph.d. thesis, Limburgs Universitair Centrum (LUC), 2002.

[35] H. Shiomi, H. Nakahata, T. Imai, Y. Nishibayashi, and N. Fujimori. *Jpn. J. Appl. Phys. Part 1 - Regul. Pap. Short Notes Rev. Pap.*, 28(5):758, 1989.

[36] A. J. Tessmer, L. S. Plano, and D. L. Dreifus. *IEEE Electron Device Lett.*, 14(2):66, 1993.

[37] K. Okano, H. Kiyota, T. Iwasaki, T. Kurosu, M. Iida, and T. Nakamura. *Appl. Phys. Lett.*, 58(8):840, 1991.

[38] S. Koizumi, K. Watanabe, F. Hasegawa, and H. Kanda. *Science*, 292(5523):1899, 2001.

[39] G. S. Gildenblat, S. A. Grot, C. W. Hatfield, A. R. Badzian, and T. Badzian. *IEEE Electron Device Lett.*, 11(9):371, 1990.

[40] M. Yokoba, Y. Koide, A. Otsuki, F. Ako, T. Oku, and M. Murakami. *J. Appl. Phys.*, 81(10):6815, 1997.

[41] Y. Koide, M. Yokoba, A. Otsuki, F. Ako, T. Oku, and M. Murakami. *Diam. Relat. Mat.*, 6(5-7):847, 1997.

[42] M. S. Alexander, M. N. Latto, P. W. May, D. J. Riley, and G. Pastor-Moreno. *Diam. Relat. Mat.*, 12(9):1460, 2003.

[43] K. L. Moazed, J. R. Zeidler, and M. J. Taylor. *J. Appl. Phys.*, 68(5):2246, 1990.

[44] T. Tachibana, B. E. Williams, and J. T. Glass. *Phys. Rev. B*, 45(20):11975, 1992.

[45] C. R. Guarnieri, F. M. Dheurle, J. J. Cuomo, and S. J. Whitehair. *Appl. Surf. Sci.*, 53:115, 1991.

[46] S. N. Mikhailov, D. Ariosa, J. Weber, Y. Baer, W. Hanni, X. M. Tang, and P. Alers. *Diam. Relat. Mat.*, 4(9):1137, 1995.

[47] M. Pitter, M. B. Hugenschmidt, and R. J. Behm. *Appl. Phys. Lett.*, 68(18):2508, 1996.

[48] Y. F. Zhu, L. Wang, W. Q. Yao, and L. L. Cao. *Appl. Surf. Sci.*, 171(1-2):143, 2001.

[49] S. A. Grot, G. S. Gildenblat, C. W. Hatfield, C. R. Wronski, A. R. Badzian, T. Badzian, and R. Messier. *IEEE Electron Device Lett.*, 11(2):100, 1990.

[50] T. Tachibana, B. E. Williams, and J. T. Glass. *Phys. Rev. B*, 45(20):11968, 1992.

[51] K. Das, V. Venkatesan, K. Miyata, D. L. Dreifus, and J. T. Glass. *Thin Solid Films*, 212(1-2):19, 1992.

[52] J. Nakanishi, A. Otsuki, T. Oku, and O. Ishiwata. *J. Appl. Phys.*, 76(4):2293, 1994.

[53] P. Muret, F. Pruvost, C. Saby, E. Lucazeau, T. A. N. Tan, E. Gheeraert, and A. Deneuville. *Diam. Relat. Mat.*, 8(2-5):961, 1999.

[54] K. L. Moazed, R. Nguyen, and J. R. Zeidler. *IEEE Electron Device Lett.*, 9(7):350, 1988.

[55] C. A. Hewett, M. J. Taylor, J. R. Zeidler, and M. W. Geis. *J. Appl. Phys.*, 77(2):755, 1995.

[56] C. M. Zhen, Y. Y. Wang, S. H. He, Q. F. Guo, Z. J. Yan, and Y. J. Pu. *Opt. Mater.*, 23(1-2):117, 2003.

[57] C. Saby, P. Muret, F. Pruvost, and G. Patrat. *Diam. Relat. Mat.*, 11(7):1332, 2002.

[58] M. Y. Liao and Y. Koide. *J. Vac. Sci. Technol. B*, 24(1):185, 2006.

[59] T. P. Humphreys, J. V. Labrasca, R. J. Nemanich, K. Das, and J. B. Posthill. *Jpn. J. Appl. Phys. Part 2 - Lett.*, 30(8A):L1409, 1991.

[60] S. Y. Zhu, C. Detavernier, R. L. Van Meirhaeghe, F. Cardon, A. Blondeel, P. Clauws, G. P. Ru, and B. Z. Li. *Semicond. Sci. Technol.*, 16(2):83, 2001.

[61] Y. Koide, M. Yokoba, A. Otsuki, F. Ako, T. Oku, and M. Murakami. *Diam. Films Technol.*, 6(2):61, 1996.

[62] H. Kiyota, H. Okushi, T. Ando, M. Kamo, and Y. Sato. *Diam. Relat. Mat.*, 5(6-8):718, 1996.

CONCLUSIONS

Conclusions

IN the first part of this work, we focussed on the inhomogeneity of the Schottky barrier height. Au/n-GaAs was used as a model metal/semiconductor contact, because it has a wide background in SB-research and because the advanced semiconductor GaAs is gaining importance in the semiconductor (mobile) industry. Small contacts were fabricated using Electron Beam Lithography. Moreover, by modifying a standard AFM to a Conducting probe AFM, we were able to measure 50 to 100 small-sized Schottky contacts on the same n-GaAs sample. This reduces possible differences in the fabrication process of the Schottky contacts.

From the measured I/V-characteristics, the homogeneous barrier height was calculated, using two different techniques, namely by fitting Tung's Pinch Off model to each individual I/V-characteristic, or by using Mönch's linear relationship between the barrier height and ideality factor, both of which are calculated from the standard Thermionic Emission model. We found that **both methods are reliable for obtaining the value of the homogeneous Schottky barrier height** (which is a unique property of the investigated MS-contact).

From the comparison of the obtained homogeneous barrier heights from diodes with a different fabrication process, we confirm the influence of the interfacial $Au^{\delta+} - O^{\delta-}$ dipole on the barrier height. The homogeneous barrier height for the Au/n-GaAs Schottky contacts without the dipole is $0.848\,eV$, while for the contacts with the dipole, we found a value of $1.021\ eV$. With this **confirmation of the dipole-model**, we strengthen the Bond Polarization Theory which states that the SBH is locally determined by the bonding of the atoms forming the interface.

The second part evidenced the solid-state formation of carbides from thin metal-carbon films. The different phases of the metal-carbon systems were identified using *in situ* **XRD**, completed with *ex situ* XRD, RBS and XPS. W, Mo, Fe, Cr and V form carbides, while Nb, Ti, Ta and Hf need an extra capping layer to prevent oxidation ($30nm\ C$ was selected as a good capping layer). Mn and Zr, however, formed oxide phases rather than carbide phases, despite the precautions we took (capping layer, no vacuum break during deposition of the different layers). **The phase sequences for the different carbide-forming transition metal-carbon systems**, are listed in table 7.19 on page 108, and their **formation temperatures** (at a heating rate of $3°C/s$) are summarized on page 109 in table 7.20.

Furthermore, **activation energies** were determined for the different carbide formations. For this, *in situ* XRD measurements at different heating rates were analyzed using a modified **Kissinger method**. The **activation energies** are listed in table 8.1 on page 124, and they can be used in the search for the mechanisms which govern the (carbide) phase formation.

The last part illustrates the possible application of carbides as contacts for C-containing semiconductors. Carbon nanotubes (CNTs) and diamond are some of the most advanced C-containing semiconductors, and they both possess very peculiar, but interesting and useful properties. We give an example of a **solid-state reaction between a metal layer (Mo) and CNTs**, forming a carbide (in this case Mo_2C). Furthermore, we give examples of **carbide formation on CVD-diamond**, with the same phase sequence as obtained in the previous part. Also, a preliminary research on the electrical characteristics on CVD-diamond was done. We conclude that **the crystal structure (and hence the dipoles) at the metal/diamond interface significantly influences the electrical properties**. To get a good comprehension of the electrical behaviour of the contacts formed on CVD diamond, one should have a good understanding of the metal-diamond interface, and thus first of the diamond surface. Furthemore, the **bond-polarization theory** is a good starting point for the comprehension of the metal-diamond interface.

APPENDICES

Appendix A

Determination of the error induced by the C-AFM technique

Influence of tip-cantilever type

THERE were two kinds of C-AFM tips available for our research, namely silicon cantilevers (and tips) with either a $25nm$ Pt-coating, or a $20nmCr/20nmAu$ -coating on both sides. For each coating, cantilevers with different force constants

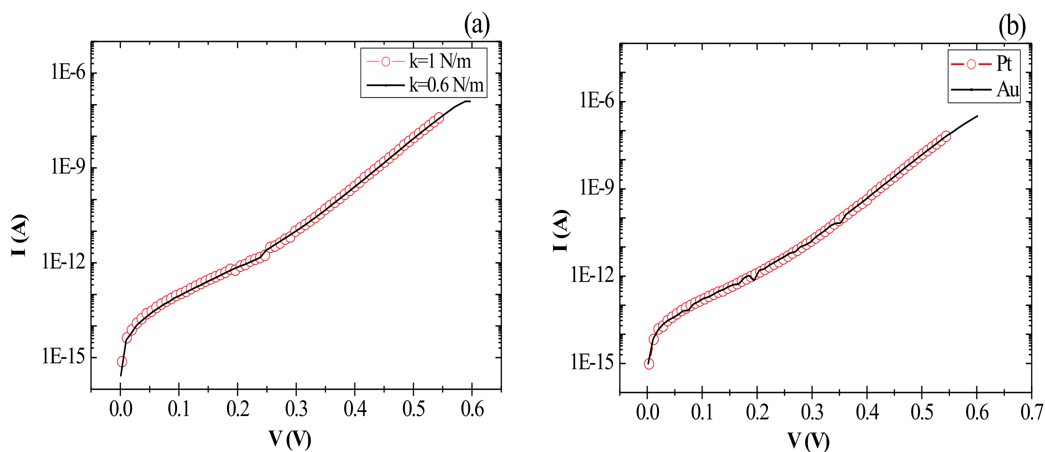

Figure A.1: *I/V characteristics measured on the same Au/n-GaAs Schottky contact. (a) Comparison between different force constants of the cantilever. (b) Comparison between different tip coatings.*

were available. To know if there is an influence of either the force constant or the coating, we did the following experiments.

We have performed I/V measurements on a same Au/n-GaAs Schottky contact using Pt-coated tips, with a force constant of $1N/m$ and $0.6N/m$. The measurements are shown in figure A.1(a). There is no observable difference between the two measurements. The same can be said for measurements done using tips with a different coating (Pt or Cr/Au), shown in figure A.1(b). We prefer the usage of Pt-coated tips, due to the longer lifetime of the coating.

Error on Φ_B and n

To get an idea of the reproducibility of the measurements, we repeated the same measurement on the same Au/n-GaAs Schottky contact. Between the mea-

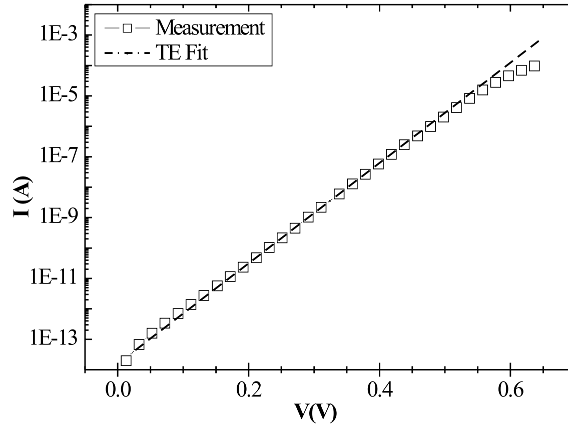

Figure A.2: *I/V characteristics measured on the same Au/n-GaAs Schottky contact*

surements, we broke the electric contact by lifting the tip from the sample and then re-established contact before doing the following measurement. For each measurement, we extracted the BH Φ_B and ideality factor n by fitting a straight line to the data, according to the Thermionic Emission (TE) model (see equation 1.8 on page 8). Figure A.2 shows one measurement, with its TE fit. One can see that the fit is good for the values between $100mV$ and $500mV$. Above $500mV$ the I/V-curve shows the influence of the series resistance, below $100mV$ low-barrier inhomogeneities are predominant. The latter will be discussed further in chapter 4.

The different values for Φ_B and n were then compared with each other, and the largest difference was taken as the measuring error on the parameter.

error(ϕ_B) $= 0.003$ eV and error(n) $= 0.009$.

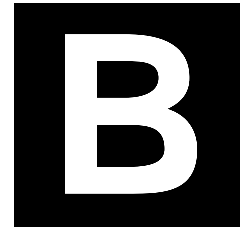

Visualization of the EBL process

FIGURE B.1 shows the different steps of the EBL patterning process. First, a double layer of photoresist is spincoated and baked on the GaAs-substrate (a). The sample is then mounted into the SEM and the homebuilt software writes the desired patterns (b). Due to the beam of electrons, the structure of the photoresist layers changes locally, i.e. only where the e-beam passes by (c). Because the lower layer of photoresist has a lower molecular weight, it is more sensitive then the layer above it. This makes the photoresist change in the typical form as seen in (c). The pattern is immersed in the MIBK:IPA solution for development. Only the changed photoresist gets washed out by the solution, leaving the sample as in (d). The sample is mounted in a PVD system vertically above the evaporation source and Au is deposited. Due to the shadowing property of PVD deposition, there will only be a Au layer on the top resist layer and on the part of the sample, which was exposed by the development (e). Acetone makes the photoresist dissolve, thus leaving the Au contact on the GaAs substrate in the desired pattern.

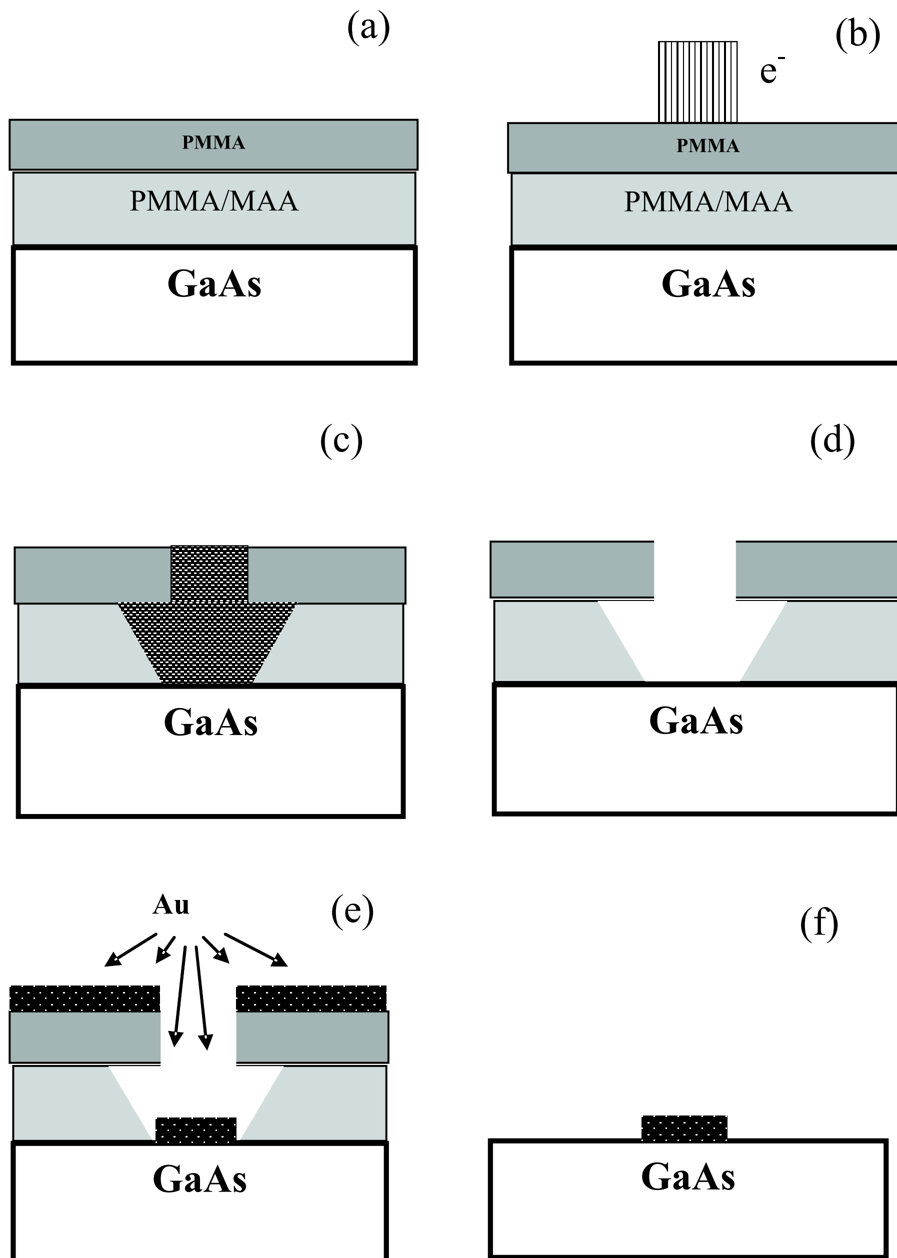

Figure B.1: *Different steps of the EBL patterning process.*

Appendix C

Error calculation for the activation energies determined by *in situ* XRD

As explained in Chapter 8, the activation energy is extracted from *in situ* XRD experiments using a Kissinger analysis. The experiments are performed at different heating rates and one plots $ln[(dT/dt)/T_f^2]$ vs $1/k_bT_f$ for the different ramp rates (dT/dt), with T_f the transition temperatures. One can fit a straight line through the data points and the slope of this straight line gives the activation energy.

Ramp Rate calibration:

An error originates from the determination of the transition temperature. The real ramp rate (dT/dt) can be different from the desired ramp rate. Therefore, the real ramp rate was determined in a region around the transition temperature and used for the calculations. Figure C.1 shows the temperature registration as a function of time, for an experiment done at $9°C/s$ on a W-C sample. For the W_2C formation, a straight line was fit to the data points within a temperature range of $850°C$ to $1050°C$, as this is the temperature region where the phase formation takes place (see figure 8.1(d)). The slope of the line yielded a real ramp rate of $8.57°C/s$. The same was done for the other transitions and the other ramp rates. These 'real' ramp rates were used in the calculation of the activation energy.

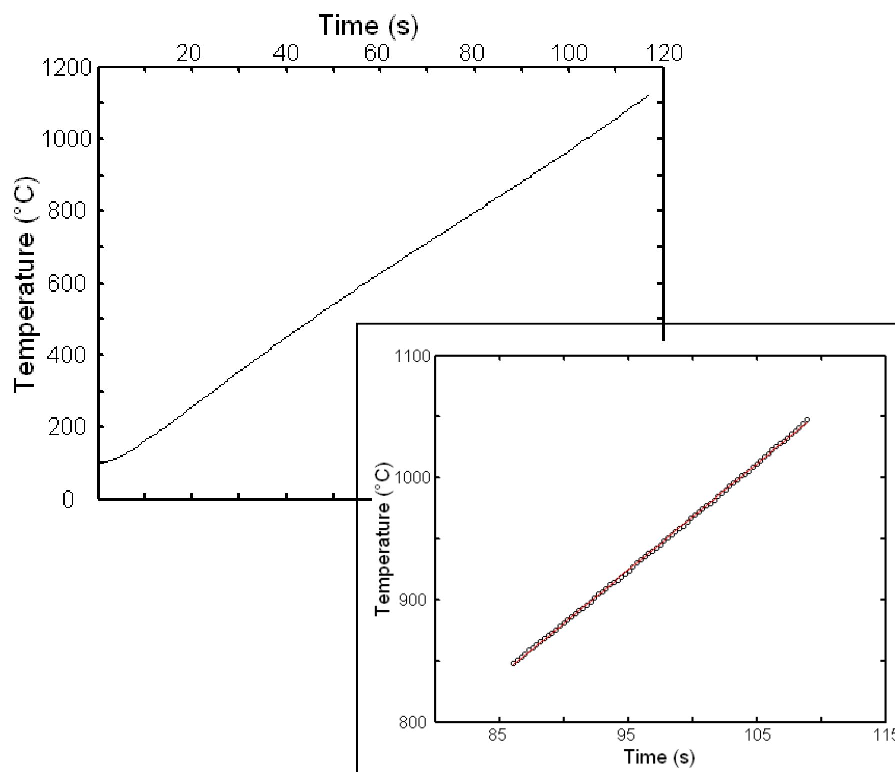

Figure C.1: *Temperature registration as a function of the time, for the in situ experiment on a W-C sample at $9°C/s$. The inset shows the temperature range $850°C$ to $1050°C$, where a straight line was fit to the data points, in order to obtain the real ramp rate (i.e. the slope of the line) for this experiment.*

A systematic error:

The thermocouple used for the temperature registration during the *in situ* experiment was calibrated using eutectics. From reproducing experiments, a certain error on the absolute temperature was estimated to be $\pm 3°C$. This 'systematic' error obviously has no influence on the ramp rate (as this is a temperature difference). However, imposing this error on the transition temperature will result in an error in x- and y-direction on the data points of the Kissinger plot. In figure C.2, the error flags were drawn for each data point. One can see that the error in the y-direction is minimal (order of 0.005), which is due to the logarithmic function. In the x-direction, an error of $\pm 3°C$ on the transition temperature results in an error of about $0.02\ (eV)^{-1}$.

As a first step, we applied the same temperature error on all transition temperatures. We did this for error-values ranging from $-20°C$ to $+20°C$, and calculated the activation energy for each set of new data points. In figure C.3(a) one can see

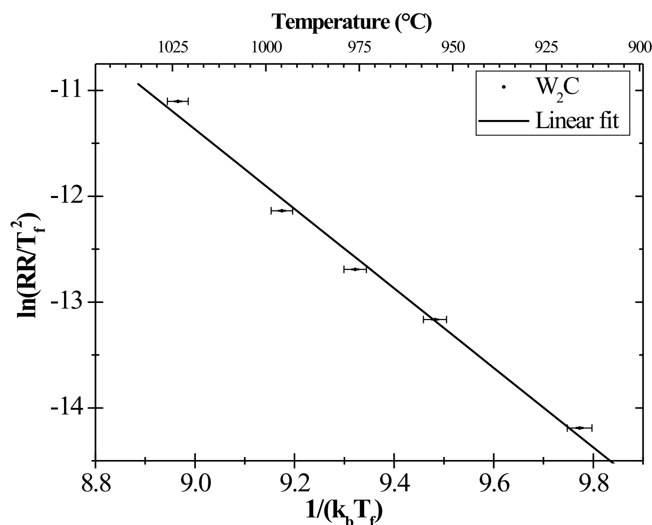

Figure C.2: *Kissinger plot for the solid-state formation of W_2C, from a W-C sample with 30nm C capping layer. Error flags have been marked on each point, which were calculated for a variation of $\pm 3°C$ on the transition temperature T_f. The errors in the y-direction are very small.*

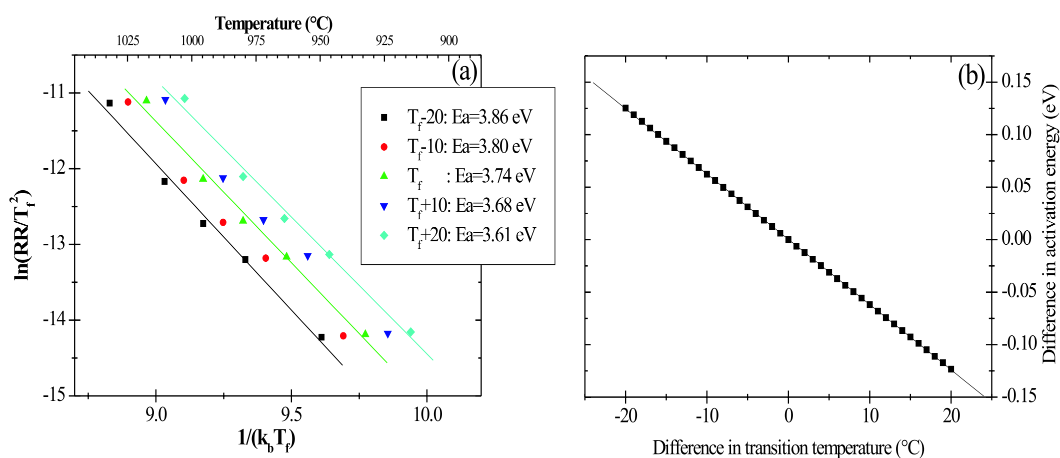

Figure C.3: *(a): Kissinger plot for the solid-state formation of W_2C, from a W-C sample with 30nm C capping layer. The transition temperatures were translated over a certain temperature (see legend), and the activation energy was calculated for each set of points. (b): Difference in activation energy compared to the originally obtained activation energy, plotted vs amount over which the transition temperatures were translated.*

that the fitted line shifts in the x-direction, linearly related to the temperature variation. As long as the shift is parallel, it has no influence on the activation energy (which is determined by the slope of the line). However, there is also a minor change of the data points in the y-direction, which causes the straight line to tilt, and thus causes changes in the activation energy. The activation energies for the data points are listed in the figure. In figure C.3(b), the difference of the 'translated activation energies' compared to the originally obtained activation energy, is plotted versus the difference in transition temperature. As can be seen, a linear relationship exists, which can also be calculated mathematically.

As an indication of the magnitude of the error on the activation energy, we calculated the difference between the original activation energy and the 'translated activation energy' (i.e. when all transition temperatures were registered at a higher/lower temperature) for a difference of $20°C$: $0.13\ eV$. For the realistic error on the temperature registration, namely $3°C$ (determined by sequential measurements of eutectics), we get a difference of $0.02\ eV$.

However, if temperature registration can be $3°C$ off, it is not to be said it will always be off in the same direction (higher or lower) for each measurement. Therefore, we calculated the activation energy for every possible combination of transition temperatures within a $3°C$ deviation of the originally determined value (E_a^0) ($1°C$ steps were used):

Deviation of T_f's at Ramp Rate X					Ea
1	3	5	9	27	
+3	+3	+3	+3	+3	3.76
+3	+3	+3	+3	+2	3.78
+3	+3	+3	+3	+1	3.81
			...		
0	0	0	0	+1	3.71
0	0	0	0	0	3.74
0	0	0	0	-1	3.76
			...		
-3	-3	-3	-3	-2	3.69
-3	-3	-3	-3	-3	3.72

From this list of activation energies, the maximum (E_a^{max}) and minimum (E_a^{min}) values are selected. By comparing these extreme values to E_a^0, we obtained a maximum error (ΔE_a^{max}) on the activation energy, calculated for the realistic error of $3°C$. These are listed in table C.1 for the carbide phases, for which an activation energy was obtained. For our example, the W_2C formation, we obtained $\Delta E_a^{max} = 0.29\ eV$. The set of transition temperatures that resulted in this maximum deviated activation energy was:

Deviation of T_f's at Ramp Rate X					Ea
1	3	5	9	27	
+3	+3	-3	-3	-3	3.76

Statistical error:

One needs to fit a straight line through the points using a least-squares method, in order to obtain the activation energy. This implies a statistical error on the value. The graphical fitting program used (in our case: Origin), supplies an error on the intercept and the slope of the fitted line. These errors are calculated from the scatter of the data about the fitted line. We have listed the error values for the slope in table C.1, along with the correlation coefficient (R). The correlation coefficient gives an indication of the scatter of the data points from the fitted line.

Table C.1: *Activation energies for the carbide phases (E_a^0) with its error, calculated via the method explained: (ΔE_a^{max}). ΔE_a^{Orig} is the statistical error supplied by the graphical fitting program, with R the correlation coefficient.*

Carbide Phase	E_a^0 (eV)	ΔE_a^{max} (eV)	ΔE_a^{Orig} (eV)	R
NbC	4.08	± 0.31	$\pm\mathbf{0.37}$	0.9879
Fe_3C	4.05	$\pm\mathbf{0.83}$	± 0.26	0.9941
W_2C	3.74	$\pm\mathbf{0.29}$	± 0.21	0.9951
WC	3.23	$\pm\mathbf{0.29}$	± 0.22	0.9932
Mo_2C	3.15	$\pm\mathbf{0.23}$	± 0.13	0.9968
Nb_2C	3.01	± 0.32	$\pm\mathbf{0.36}$	0.9797
VC	2.65	± 0.21	$\pm\mathbf{0.38}$	0.9709
HfC	2.05	± 0.16	$\pm\mathbf{0.19}$	0.9749
TiC	1.45	± 0.14	$\pm\mathbf{0.81}$	0.7184

Final error:

In table C.1, the largest error of the two (ΔE_a^{max} or ΔE_a^{Orig}) is marked in bold and is used for the E_a values. One can easily see that the statistical error is the largest whenever the correlation coefficient is below 0.99. In this work, we will supply the correlation coefficient along with the value for E_a and ΔE_a. This allows one to determine which error was the largest and thus was used.

List of Publications

THE results from this Ph.D. work can be found in the following publications:

- **Leroy WP**, Detavernier C, Van Meirhaeghe RL, and Lavoie C;
  Thin film solid-state reactions forming carbides as contact materials for carbon-containing semiconductors;
  submitted to Journal of Applied Physics, Sep 2006
  (minor revision, Dec 2006).

- **Leroy WP**, Detavernier C, Van Meirhaeghe RL, Kellock AJ, and Lavoie C;
  Solid-state formation of titanium carbide and molybdenum carbide as contacts for carbon-containing semiconductors;
  Journal of Applied Physics 99(6) Art.No. 063704, Mar 15 2006.

- **Leroy WP**, Opsomer K, Forment S, and Van Meirhaeghe RL;
  The barrier height inhomogeneity in identically prepared Au/n-GaAs Schottky barrier diodes;
  Solid-State Electronics 49(6) 878-883, Jun 2005.

- Forment S, Biber M, Van Meirhaeghe RL, **Leroy WP**, and Turut A;
  Influence of hydrogen treatment and annealing processes upon the Schottky barrier height of Au/n-GaAs and Ti/n-GaAs diodes;
  Semiconductor Science and Technology 19(12) 1391-1396, Dec 2004.

Life is far too important a thing
ever to talk seriously about.

OSCAR WILDE
(1854-1900)